

Université du Québec
Institut national de la recherche scientifique
Centre Énergie Matériaux et Télécommunications

Improvement of air breakdown limit in photoconductive antennas by surface passivation for intense terahertz generation

By

Xiaolei Peng

A thesis submitted to the Department of Energy, Materials and Communications in conformity
with the requirements for the degree of Master of Science.

Jury members:

Internal examiner: Dr. Luca Razzari
(President of the jury) INRS-EMT, Canada

External examiner: Dr. Jonathan Holzman
The University of British Columbia, Canada

Research supervisor: Dr. Tsuneyuki Ozaki
INRS-EMT, Canada

Abstract

Terahertz (THz) electromagnetic waves, located between microwaves and infrared waves, provide an attractive spectral region for imaging, communication, medical diagnostics and other applications. However, the THz portion of the electromagnetic spectrum has remained one of the last frontiers in optics, having only recently been exploited in the industry. This is because the technology for the efficient generation and detection of THz radiation has been difficult to develop, as it requires either extremely fast electronics or long-wavelength photonics.

A photoconductive antenna (PCA) is typically composed of a high resistivity semiconductor substrate with two electrodes fabricated on one face of the substrate. PCAs are widely used to generate THz radiation because they can demonstrate high optical-to-THz conversion efficiency when operating at room temperature. Since their demonstration as practical THz sources and detectors, PCAs have been the subject of a vast number of scientific and industrial reports investigating their application as THz transmitters and receivers.

This thesis aims to develop intense THz sources using PCAs. At the Advanced Laser Light Source (ALLS), large aperture photoconductive antennas (LAPCAs) based on ZnSe crystal have already been developed. This source uses 20 mJ laser energy to generate free space THz pulses with energy up to $8.3 \pm 0.2 \mu\text{J}$. The main limitation of the ZnSe-based intense THz source is that the maximum applied bias field (which determines the maximum radiated THz field) is still limited in practice by air breakdown.

We overcome the air breakdown limit by the surface passivation method, opening the road to generate intense THz radiation. More precisely, the antenna is covered with a dielectric layer of epoxy resin to avoid air breakdown, which allows higher bias fields to be applied, thus potentially generating THz radiation with higher peak electric fields.

We demonstrate that the maximum applied bias field increases more than 2.2 times by using the surface passivation method. Further, even with the same bias field, the peak electric field of the generated THz radiation increases more than 1.37 times after covering the PCAs with an epoxy layer. We demonstrate that after covering the GaAs PCA with the epoxy coating, the optical fluence irradiating the GaAs surface increases, leading to the increase in the generated THz electric field.

Résumé

Les ondes électromagnétiques térahertz (THz), situées entre les micro-ondes et les infrarouges, constituent une région spectrale intéressante pour l'imagerie, la communication, les diagnostics médicaux et d'autres applications. Cependant, la portion THz du spectre électromagnétique est restée l'une des dernières frontières de l'optique qui a été exploitée récemment dans l'industrie. En effet, la technologie permettant de générer et de détecter efficacement les ondes THz a été difficile à mettre au point, car elle nécessite soit une électronique de pointe et extrêmement rapide, soit une photonique avec de grande longueur d'onde.

Une antenne photoconductrice (APC) est généralement composée d'un substrat semi-conducteur de haute résistivité avec deux électrodes déposées sur une face du substrat. Les APCs sont largement utilisées pour générer des ondes THz car elles peuvent démontrer une efficacité de conversion optique-THz élevée lorsqu'elles fonctionnent à température ambiante.

Cette thèse vise à développer des sources THz intenses en utilisant les APCs. Au Laboratoire de Sources Femtosecondes (LSF), les antennes photoconductrices à grande ouverture (APCGOs) basées sur un cristal de ZnSe ont déjà été développées. Cette source utilise une énergie laser de 20 mJ pour générer des impulsions THz en espace libre avec une énergie allant jusqu'à 8.3 µJ. La principale limite de cette source THz intense est que le champ de polarisation maximum appliqué (qui détermine l'intensité maximale de l'onde THz maximum rayonnée) est toujours limité en pratique par la force diélectrique de l'air.

Nous avons surmonté la limite du claquage de l'air par la méthode de passivation de surface, ouvrant ainsi la voie à la génération d'un rayonnement THz intense. Plus précisément, l'antenne est recouverte d'une couche diélectrique faite à partir de résine époxy. Cette dernière ayant une force diélectrique plus élevée que celle de l'air, nous pouvons appliquer des champs de polarisation plus élevés, et donc générer un rayonnement THz plus intense.

Nous avons démontré que le champ de polarisation maximum appliqué augmente de plus de 2.2 fois en utilisant la méthode de passivation de surface. En outre, même avec un champ de polarisation identique, le champ électrique de crête du rayonnement THz généré augmente de plus de 1.37 fois après avoir revêtu l'APC par la couche d'époxy. Nous avons également démontré qu'après avoir recouvert la surface de l'APC de GaAs avec la couche d'époxy, la fluence optique irradiant la surface de GaAs augmente, ce qui entraîne l'augmentation du champ électrique THz généré.

Acknowledgement

I am first and foremost grateful to my research advisor, Professor Tsuneyuki Ozaki, for his patience, motivation, enthusiasm and immense knowledge. I was extremely lucky to have such an exceptional research director. The discussions with Prof. Ozaki were always encouraging, enjoyable and inspiring. He also considered my research interest while offering me projects. It is one of the most valuable experiences in my life being able to study under his supervision.

I would sincerely like to thank my colleague Dr. Xavier Ropagnol for his support during my Master's. It is his expertise in the large aperture photoconductive antenna THz source that makes this thesis even possible. He was always there to ask. His guidance helped me in all the time of research and writing. He also taught me to become an independent researcher, take initiative and solve problems.

I'm also very grateful to my colleagues Mangaljit Singh, Elchin Isgandarov, Ahmed Mohamed, Romain Marcelino and Carlos M. Garcia-Rosas for their help and collaboration. Massive thanks to the departmental and technical staff at INRS-EMT and all my friends who have made my research life so enjoyable.

Great thanks to the members of the jury: Prof. Luca Razzari and Prof. Jonathan Holzman for reviewing and evaluating my thesis.

Last but not least, I would like to give special thanks to my family: my parents and my brother, for their continuing love and heartily support. I thank my family and friends for supporting me spiritually throughout my life.

Table of Contents

Chapter 1. Introduction	1
Chapter 2. Intense THz generation and detection techniques	5
2.1 Optical rectification (OR)	5
2.2 THz generation from photoconductive antennas (PCAs)	8
2.3 THz detection by PCAs	16
2.4 Free-space electro-optic sampling	17
2.5 THz time-domain spectroscopy (THz-TDS)	18
Chapter 3. Increasing the THz intensity generated from LAPCA	34
3.1 Introduction	34
3.2 Paschen's law	34
3.3 Breakdown field of GaAs-based PCA	35
3.4 THz generated from GaAs-based PCA	40
Chapter 4. Conclusions and Perspectives	50
References	51
Sommaire Récapitulatif	59

List of Figures

Figure 1. THz band in the electromagnetic spectrum	1
Figure 2. Mechanism of intense THz pulse induced intervalley scattering. The electrons in the conduction band are accelerated by the THz electric field (green arrow); after acquiring enough kinetic energy, they can scatter into the L valley	2
Figure 3. Normalized time integral of the square modulus of the transmitted electric field as a function of the Z-scan position of the InGaAs sample for three different peak THz fields (174, 144 and 115 kV/cm) and for the bare InP substrate at a peak field of 174 kV/cm	3
Figure 4. Schematic view of THz generation via optical rectification in a nonlinear crystal. A femtosecond laser pulse, passing through a nonlinear medium, generates a broadband THz pulse using difference frequency generation processes	7
Figure 5. Schematic view of a typical photoconductive antenna (PCA). A DC bias voltage is applied to the semiconductor substrate to drive the photoexcited carriers	8
Figure 6. THz peak electric field versus fluence for a 6H-SiC (a) and 4H-SiC (b) PC antenna excited at 400 nm and biased with three different bias fields. (c) is an expanded scale of the bottom left part of (b), in order to show the quadratic dependence of the THz field on fluence for the 4H-SiC PCA at low excitation fluence	10
Figure 7. Calculated photocurrent, the amplitude of the radiated electric field and the laser pulse shape as a function of time	11
Figure 8. Bandgap of InGaN versus the indium concentration	13
Figure 9. Electron mobility of the InGaN as a function of indium concentration	14
Figure 10. A typical 6H-SiC interdigitated LAPCA. Here, the iLAPCA is composed of 38 electrodes with a gap distance of 800 μm and a width and length of 1 and 55 mm, respectively	14
Figure 11. Schematic view of the interdigitated ZnSe antenna covered with a binary phase mask and shadow mask	15
Figure 12. (a) THz pulses shapes generated from the ZnSe iLAPCA excited at 400 nm with a fluence of 0.2 mJ/cm^2 , at a bias field of 10 kV/cm with 0.65 and 1 mm binary mask and a shadow mask. (b) Power spectrum with a shadow mask (blue line) and the 1 mm binary mask (red line). (c) and (d) THz pulse shapes obtained with the 0.65 mm (c) and the 1 mm (d) binary mask on the ZnSe iLAPCA	16
Figure 13. Schematic view of THz detection using the electro-optic sampling technique	17
Figure 14. CCD image of the PCA emitter	20
Figure 15. Schematic of THz-TDS system using the PCA emitter and PCA detector	20

Figure 16. (a) THz waveforms and (b) amplitude spectrum, generated and detected by Teravil's GaBiAs PCA emitter and detector before (red) and after (blue) rough alignment of the HR Si lenses	21
Figure 17. (a) Typical waveform for a THz-TDS experiment. The blue curve is the measurement of reference through air, and the red curve is the measurement of the sample. (b) The frequency spectrum. The gray-shaded area represents the upper limit of the useful spectral region of the measurements	22
Figure 18. Unwrapped phase (a) from Origin (before correction), (b) from MATLAB (after correction)	22
Figure 19. (a) Representation of time-domain electric field waveforms measured by THz-TDS and TRTS. (b) Corresponding frequency-domain intensity spectra obtained from the Fast Fourier transform (FFT)	23
Figure 20. Electric field of THz signal in THz-TDS measurement of the 1 mm CdTe sample	24
Figure 21. Amplitude spectrum of THz signal in THz-TDS measurement of the 1 mm CdTe sample	24
Figure 22. Unwrapped phase of THz signal in THz-TDS measurement of the 1 mm CdTe sample	25
Figure 23. Index of refraction of the 1 mm CdTe sample	25
Figure 24. Absorption coefficient of the 1 mm CdTe sample	26
Figure 25. Index of refraction and absorption coefficient of (A) ZnTe and (B) CdTe from literature	27
Figure 26. (a) Amplitude when the end of THz pulse is included. (b) Amplitude when the end of THz pulse is set to zero. When the end of the THz pulse is set to zero, the oscillation in the amplitude is mitigated ...	27
Figure 27. (a) Absorption coefficient when the end of THz pulse is included. (b) Absorption coefficient when the end of THz pulse is set to zero. The oscillation is mitigated when the end of the THz pulse is set to zero	28
Figure 28. The upper limit of the detectable absorption of CdTe (dynamic range)	28
Figure 29. Schematic of the THz-TDS system using a nonlinear crystal as the THz emitter and the PCA as the THz detector	29
Figure 30. Electric field of THz signal in THz-TDS measurement of the 2 mm ZnTe sample	30
Figure 31. Amplitude of THz signal in THz-TDS measurement of the 2 mm ZnTe sample	30
Figure 32. Unwrapped phase of THz signal in THz-TDS measurement of the 2 mm ZnTe sample	31
Figure 33. Index of refraction of the 2 mm ZnTe sample	31
Figure 34. Absorption coefficient of the 2 mm ZnTe sample	32
Figure 35. The upper limit of the detectable absorption of the 2 mm ZnTe sample (dynamic range)	33
Figure 36. Paschen curves obtained for helium, neon, argon, hydrogen and nitrogen, using the expression for the breakdown voltage	35
Figure 37. The schematic view of GaAs band structure. Optical photons can excite electrons directly into the Γ valley	36

Figure 38. PCA with a large gap size of 0.9066 mm designed in AutoCAD	37
Figure 39. The GaAs substrate after cleaning	38
Figure 40. PCA with a large gap size of 0.9066 mm fabricated on GaAs substrate	38
Figure 41. GaAs PCA with a large gap size of 0.9066 mm fixed on the mount for measuring the air breakdown field	39
Figure 42. Air breakdown observed in the GaAs PCA when a bias field of 23.3 kV/cm is applied	39
Figure 43. Breakdown observed in the GaAs PCA when a bias field of 53.3 kV/cm is applied	40
Figure 44. Schematic of the setup using GaAs PCA as THz emitter	41
Figure 45. THz waveforms at different bias voltages. The THz peak electric field increases as the bias voltage increases	42
Figure 46. Relationship between the THz peak electric field and the applied bias field. From 2.2 kV/cm to 4.4 kV/cm, the THz peak electric field scales linearly with the bias field	42
Figure 47. Failure of GaAs PCA after applying a bias field of 5.5 kV/cm, due to the increase in temperature	43
Figure 48. THz waveform (a) at 200 V bias voltage, (b) at 400 V bias voltage, with (red curve) and without the epoxy coating (black curve). By covering the GaAs PCA with the epoxy resin, the THz peak electric field increases	44
Figure 49. THz amplitude spectrum (a) at 200 V bias voltage, (b) at 400 V bias voltage, with (red curve) and without the epoxy coating (black curve)	44
Figure 50. (a) Schematic of the 522 nm femtosecond laser transmitting into bare GaAs substrate. (b) Schematic of the 522 nm femtosecond laser transmitting into GaAs substrate with an 0.7 μ m thick epoxy coating	45
Figure 51. The intensity of the laser after travelling through z microns of GaAs without epoxy layer	46
Figure 52. The intensity of the laser after travelling through z microns of GaAs with epoxy layer	46
Figure 53. (a) Schematic of the laser beam transmitting into bare GaAs substrate. (b) Schematic of the laser beam transmitting into GaAs substrate with an 0.15 mm thick epoxy coating	47

List of symbols

Electro-optic coefficient of ZnTe crystal	r_{41}
Electro-optic coefficient of LiNbO ₃ crystal	r_{33}, r_{51}
Electro-optic coefficient of LiTiO ₃ crystal	r_{33}, r_{51}
Electro-optic coefficient of CdTe crystal	r_{41}
Electro-optic coefficient of DAST crystal	r_{11}
Electro-optic coefficient of GaAs crystal	r_{41}
Extraordinary index of refraction	n_e
Ordinary index of refraction	n_o
Polarization	P
Radiated THz electric field	E_{THz}
Far-field electric field	E_{far}
Bias field	E_{bias}
Free space permittivity	ϵ_0
Velocity of light	c
Current density	J
Energy of band gap	E_g
Electron charge	e
THz energy	W_{THz}
Wavelength	λ
Optical pump energy	W_{opt}
Fluence	F
Saturation fluence	F_{sat}
Optical fluence	F_{opt}
Electric field	E
Index of refraction	n
Thickness of the sample	d

Chapter 1

Introduction

Terahertz (THz) electromagnetic waves have provided an attractive spectral region for imaging, communication, medical diagnostics and other applications, due to their non-invasive properties and excellent spectroscopic and sensing abilities. As shown in Figure 1 [107], located between microwaves and infrared waves, THz roughly ranges from 0.1×10^{12} to 10×10^{12} Hz, and 1 THz is equivalent to 1 picosecond in time, 0.3 mm in wavelength and 4.14 meV in photon energy. THz radiation bridges the gap between photonics and electronics devices, and it provides a vast amount of useful bandwidth.

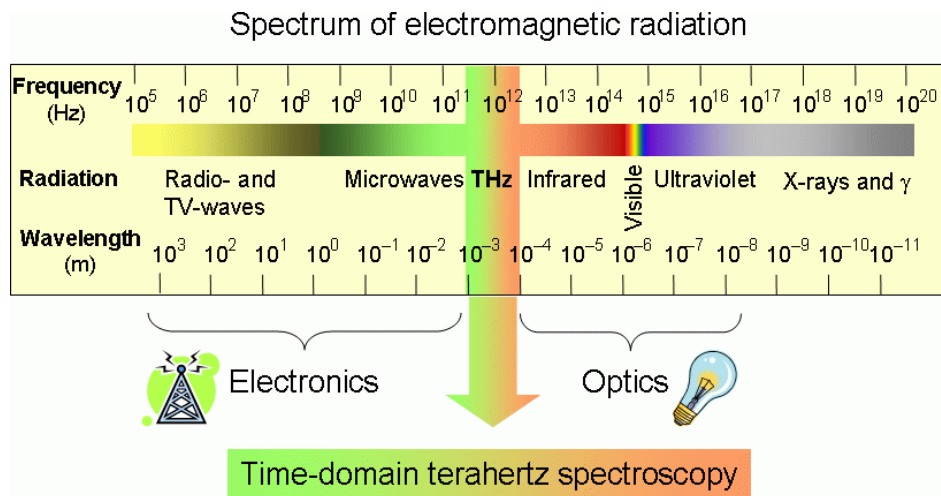


Figure 1. THz band in the electromagnetic spectrum [107].

Although THz radiation is invisible to the human eye, it has a lot of unique attributes and possesses great potential for applications in our daily life. For example, many materials that block visible and infrared light turn out to be transparent in the THz frequency range [7], and THz is selectively absorbed by water and organic substances [10]. Moreover, THz imaging can achieve sub-mm spatial resolutions, and near-field imaging allows resolutions in the nm regime [8].

Further, due to its small photon energy, the THz wave is non-invasive and nonionizing compared to X-ray waves, and it is considered to be harmless for humans, plants and animals [9].

Researchers faced enormous technical problems in the generation and detection of THz pulses, due to the lack of high-energy pulsed laser sources and sensitive detectors. It was not until 1992 that the first intense THz source was reported by You *et al.* [11]. After long inactivity, Blanchard *et al.* demonstrated the generation of intense THz pulses by optical rectification from a large aperture ZnTe crystal [12] in 2007. Furthermore, Ropagnol *et al.* developed a ZnSe-based interdigitated large aperture photoconductive antenna (iLAPCA) THz source in 2013 [13,14]. Due to their large bandgap and high dielectric strength, 6H-SiC and GaN substrates are also used for fabricating large aperture photoconductive antennas (LAPCAs) [15,16]. In the search for new materials, organic crystal BNA (N-benzyl-2-methyl-4-nitroaniline) and the DAST crystal are considered to be able to generate intense THz radiation [17,18]. With the laser facilities of the Advanced Laser Light Source (ALLS) at the INRS-EMT, the generated THz pulse energies are getting more and more intense and have increased from a few nJ up to several μJ [12-14,19-23].

With the efficient and compact table-top THz source with high intensity, we can study a lot of fascinating nonlinear phenomena and novel applications, such as the anisotropic effective mass of hot electrons in the non-parabolic band of InGaAs [106], intraband and interband carrier dynamics [5] and absorption bleaching of THz pulses in n-doped semiconductors [1,3]. In addition, the development of THz time-domain spectroscopy (THz-TDS) opened a new chapter in THz science, initiating great efforts to develop various applications to exploit the unique opportunities that THz waves offer [24-28].

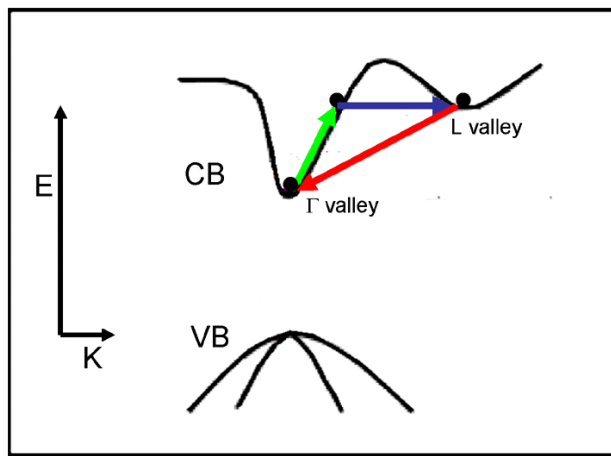


Figure 2. Mechanism of intense THz pulse induced intervalley scattering. The electrons in the conduction band are accelerated by the THz electric field (green arrow); after acquiring enough kinetic energy, they can scatter into the L valley [1].

THz pulse can serve as a transient voltage bias, driving a lot of nonlinear phenomena in semiconductors. As shown in Figure 2 [1], the carriers at the bottom of the conduction band are accelerated by the high THz fields, gaining kinetic energy through each oscillation. When the kinetic energy is higher than the nearest intervalley separation, they can scatter into the L valley, where the effective mass of electrons is higher and the carrier mobility is lower. This effect results in a reduction in the conductivity of the semiconductor layer, and thus the transmission of the THz pulse increases as the conductivity of the sample decreases. Therefore, nonlinear transmission enhancement (also known as absorption bleaching) is observed in n-doped semiconductors at high THz fields, as shown in Figure 3 [14].

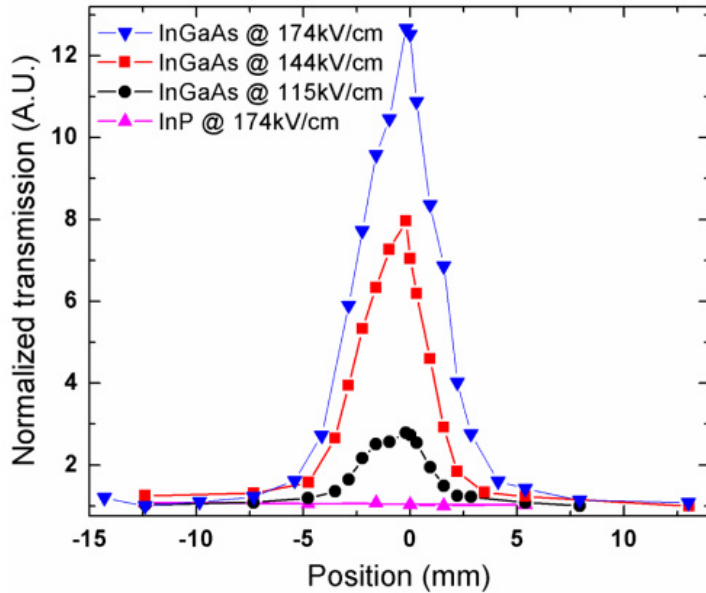


Figure 3. Normalized time integral of the square modulus of the transmitted electric field as a function of the Z-scan position of the InGaAs sample for three different peak THz fields (174, 144 and 115 kV/cm) and for the bare InP substrate at a peak field of 174 kV/cm [14].

The high THz field used in studying the absorption bleaching effect is provided by an interdigitated ZnSe LAPCA [14]. It is a very efficient and compact table-top THz source, which can generate free space THz pulses with energy up to $8.3 \pm 0.2 \mu\text{J}$. It is also very convenient since we can easily control the THz peak electric field by applying a specific bias field.

In chapter 2, we will discuss the generation and detection techniques of THz radiation, as well as the principle and experimental results of THz time-domain spectroscopy (THz-TDS). For the THz generation, we will mainly discuss THz emission from nonlinear crystals via optical rectification and THz radiation generated by photoconductive antennas (PCAs). In chapter 3, we

will investigate the THz generation from large aperture photoconductive antennas (LAPCAs) and new methods to increase the THz intensity.

Chapter 2

Intense THz generation and detection techniques

2.1 Optical rectification (OR)

Optical rectification (OR) is an extensively used approach for intense THz generation. It is a second-order nonlinear process that can take place in noncentrosymmetric media. This effect was first reported using Ruby lasers in a KDP crystal by M. Bass *et al.* in 1962 [29].

Optical rectification is usually much simpler for THz generation compared with PCAs, since we do not need high-voltage supplies to provide the bias field. Generally speaking, optical rectification refers to the generation of quasi-DC polarization when a strong laser beam passes through a nonlinear crystal. The change in the nonlinear polarization over time in the nonlinear medium resulting from femtosecond laser could contain many different frequency components, inducing the emission of THz.

In nonlinear optics, the electric polarization P induced in the medium can be expressed as the power series of the electric field of optical pump E :

$$\vec{P} = \varepsilon_0 (\chi^{(1)} \vec{E} + \chi^{(2)} \vec{E} \vec{E} + \chi^{(3)} \vec{E} \vec{E} \vec{E} + \dots) \quad (1)$$

Here, $\chi^{(n)}$ is the n th-order susceptibility tensor of the material. The second term in equation (1) explains the optical rectification process; this is due to the noncentrosymmetric nature of the nonlinear crystal, which causes optical rectification. Equation (2) shows the nonlinear polarization related with optical rectification:

$$\vec{P}_{OR}^{(2)}(\Omega) = \varepsilon_0 \chi^{(2)}(\Omega, \omega_1, \omega_2) \vec{E}(\omega_1) \vec{E}^*(\omega_2) \quad (2)$$

Here, Ω is the frequency difference between the two frequency components of the optical pump ω_1 and ω_2 . In the time domain, the THz far-field is proportional to the second-order derivative of the induced polarization with respect to time, given by [53]:

$$\vec{E}_{THz}(t) \propto \frac{\partial^2}{\partial t^2} \vec{P}_{OR}^{(2)}(t) \quad (3)$$

$$\vec{P}(t) = \varepsilon_0 (\chi^{(1)}(t) \vec{E}(t) + \chi^{(2)}(t) \vec{E}(t) \vec{E}(t) + \chi^{(3)}(t) \vec{E}(t) \vec{E}(t) \vec{E}(t) + \dots) \quad (4)$$

Apparently, by increasing the optical pump power, one can obtain a higher electric field of THz [30-37]. In theory, the spectral bandwidth of the generated THz pulses depends exclusively on

the frequency components of the pump beam. But in order to efficiently generate high-energy THz pulses, several prerequisites must be met [38]:

1. To begin with, apart from the noncentrosymmetric crystal structure, the medium should be highly transparent at all relevant frequencies. Otherwise, the length of the effective interaction will be limited by absorption.
2. Since difference frequency generation is a nonlinear process, high intensities need to be used. For material selection, this means that it must have a relatively high damage threshold to withstand the high intensity of the femtosecond pump beam.
3. Furthermore, many other material properties, such as absorption, diffraction, saturation and phase-matching conditions must be cautiously analyzed. Among these factors, the phase-matching between the optical group velocity and the THz phase velocity is one of the most significant requirements for an efficient optical rectification process, which determines the best parameters for the orientation and thickness of crystals. The phase-matching condition is given by:

$$\vec{k}(\omega_2) - \vec{k}(\omega_1) = \vec{k}(\Omega) \quad (5)$$

Here, \vec{k} is the wave vector depending on the electromagnetic frequency and the corresponding refractive indexes. The definition of coherence length is the interaction length at which the phase change reaches π , during which THz waves can have a positive accumulation to prevent the effects of phase mismatch [42]:

$$\Delta k L_c = \pi \quad (6)$$

Here $\Delta k = k_{\omega_2} - k_{\omega_1} - k_{THz}$ and L_c is the coherence length. To generate efficient THz radiation from a bulk crystal, the thickness of the crystal cannot be longer than the coherence length to avoid the conversion cancellation due to phase mismatch.

According to these factors, several nonlinear mediums can be chosen as an appropriate THz emitter via OR. As a highly relevant process of OR, the performance of electro-optic (EO) sampling techniques used for characterizing THz pulses also depends on these key rules. Table 1 summarizes some important parameters of nonlinear materials commonly used for OR [20,44-45].

Table 1. Important parameters of nonlinear materials commonly used for OR [20,44-45].

Crystal	EO coefficient (pm V ⁻¹)	Refraction index	THz refraction index	THz absorption coefficient (cm ⁻¹)
ZnTe	$r_{41} = 4.0$ (0.633μm)	2.85 (0.8μm)	3.17	1.3
<i>LiNbO₃</i>	$r_{33} = 30.9$ $r_{51} = 32.6$ (0.633μm)	$n_o = 2.29$, $n_e = 2.18$ (0.633μm)	$n_o = 6.8$, $n_e = 4.98$	16
<i>LiTiO₃</i>	$r_{33} = r_{51} = 30.5$ (0.82μm)	$n_o = 2.176$, $n_e = 2.18$ (0.633μm)	$n_o = 6.5$, $n_e = 6.4$	46
CdTe	$r_{41} = 4.5$ (1.00μm)	2.84 (0.8μm)	3.23	4.8
DAST	$r_{11} = 160$ (0.82μm)	$n_o = 2.46$, $n_e = 1.70$ (0.82μm)	2.4	150
GaSe	1.7 (0.8μm)	2.85 (0.8μm)	3.72	0.07
GaAs	$r_{41} = 1.43$ (1.15μm)	3.61 (0.886μm)	3.4	0.5

A simple configuration for THz radiation generated through the optical rectification process is shown in Figure 4. As mentioned above, as an intense femtosecond laser beam propagates through a second-order nonlinear medium, a transient polarization is induced, resulting in the emission of THz radiation. The electric field of the generated THz pulse is proportional to the second time derivative of this polarization [39-43].

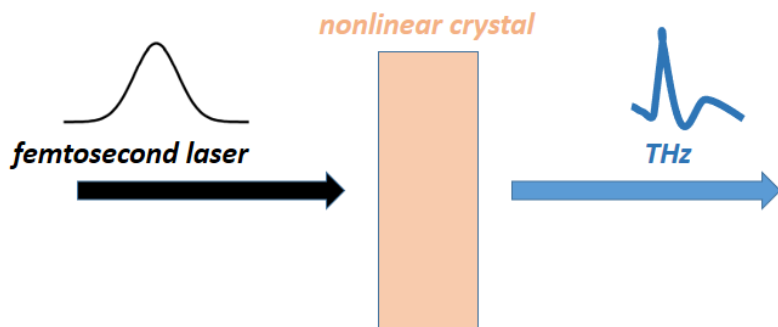


Figure 4. Schematic view of THz generation via optical rectification in a nonlinear crystal. A femtosecond laser pulse, passing through a nonlinear medium, generates a broadband THz pulse using difference frequency generation processes.

With the configuration shown above, researchers have demonstrated generating intense and broadband THz pulses using nonlinear crystals such as LiNbO₃, ZnTe, GaAs, CdTe, GaP, DAST and BNA [37,46-48]. It has been shown that organic molecular crystals like DAST are more efficient than ZnTe crystals of the same thickness, but they are more fragile and normally suffer from lower damage thresholds [49-51].

2.2 THz generation from photoconductive antennas (PCAs)

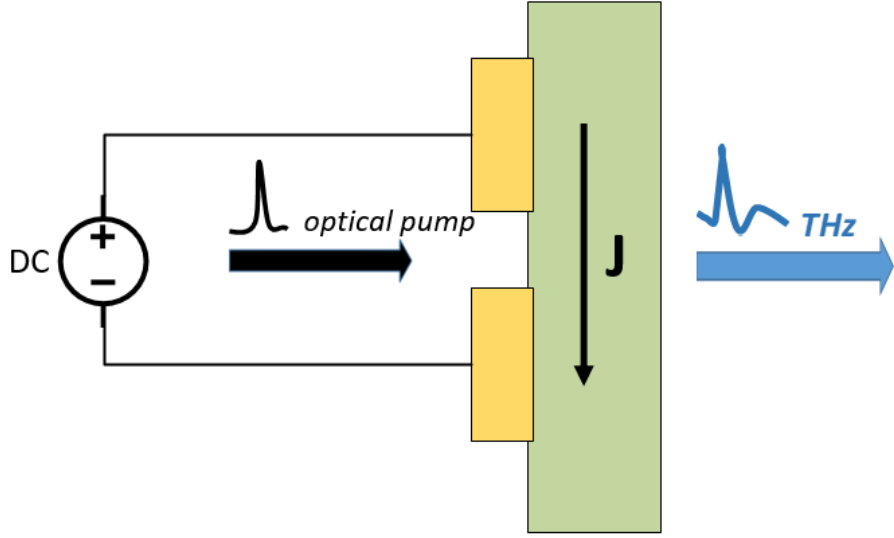


Figure 5. Schematic view of a typical photoconductive antenna (PCA). A DC bias voltage is applied to the semiconductor substrate to drive the photoexcited carriers.

As shown in Figure 5, a PCA is typically composed of a high-resistivity semiconductor substrate with two electrodes fabricated on one side [21]. The femtosecond laser pulse illuminates the semiconductor substrate where the metal electrodes have been deposited, exciting carriers from the valence band to the conduction band. These free carriers are accelerated by a bias field to generate a photocurrent. The variation of the photocurrent density in the picosecond time scale generates the THz pulse. Two of the most unique characteristics of THz pulses generated from PCAs are their quasi-half-cycle nature and their relatively low central frequency, lying between 0.05 and 1 THz. To generate high-energy THz pulses, large aperture photoconductive antennas (LAPCAs) have been studied and developed [52,53].

The relation between the surface current $J(t)$ and the radiated near field $E_{near}(t)$ can be expressed as [54,62]:

$$J(t) = -\frac{(1 + \sqrt{\epsilon_r})}{\eta_0} E_{near}(t) \quad (7)$$

Here, η_0 is the free impedance and ϵ_r is the material's relative permittivity. From Ohm's law, $J(t)$ can also be written as [63]:

$$J(t) = \sigma_s(t)(E_b + E_{near}(t)) \quad (8)$$

Here, $\sigma_s(t)$ is the surface conductivity of the PCA, and E_b is the bias electric field. The conductivity is proportional to the electron mobility and density. The electron mobility remains constant over the duration of the rising of the current density. In this case, the surface conductivity $\sigma_s(t)$ can be expressed as [55]:

$$\sigma_s(t) = e\mu n(t) \quad (9)$$

Here, e is the electron charge, μ is the electron mobility, and $n(t)$ is the time-dependent electron density. When using a femtosecond laser pulse, the electron density will increase at the timescale of the femtosecond laser and then decrease at a timescale proportional to the carrier recombination time. Equation (9) can be rewritten as [62,64]:

$$\sigma_s(t) = \frac{e(1-R)}{hv} \int_{-\infty}^t \mu(t-t') I_{opt}(t') \exp\left(-\frac{t-t'}{\tau_c}\right) dt' \quad (10)$$

Here, R is the reflectivity of the PCA substrate at the laser wavelength, hv is the photon energy, I_{opt} is the optical intensity, and τ_c is the carrier lifetime. By combining equations (7) and (8), we obtain a new expression for the radiated near field E_{near} [54]:

$$E_{near}(t) = -E_b \eta_0 \frac{\sigma_s(t)}{\sigma_s(t)\eta_0 + (1 + \sqrt{\varepsilon_r})} \quad (11)$$

Equation (11) indicates that the radiated near field E_{near} is linearly proportional to the bias electric field E_b . Further, the scaling of E_{near} is proportional to the surface conductivity but scales hyperbolically. The maximum radiated near field, E_{near}^{max} , is expressed as [62]:

$$E_{near}^{max} = -E_b \eta_0 \frac{\sigma_s^{max}}{\sigma_s^{max} \eta_0 + (1 + \sqrt{\varepsilon_r})} \quad (12)$$

where σ_s^{max} is the peak surface conductivity. In this case, the peak surface conductivity appears just at the end of the laser pulse before carrier recombination happens. From equation (10), the maximum surface conductivity can be expressed as follows [62]:

$$\sigma_s^{max} = \frac{e(1-R)\mu F_{opt}}{hv} \quad (13)$$

Here, F_{opt} is the optical fluence, and μ is the transient carrier mobility. From equations (12) and (13), we can obtain the new expression for the radiated near field [54]:

$$E_{near}^{max} = -E_b \frac{F_{opt}}{F_{opt} + \frac{hv(1 + \sqrt{\varepsilon_r})}{e(1-R)\mu\eta_0}} = -E_b \frac{F_{opt}}{F_{opt} + F_{sat}} \quad (14)$$

Here, F_{sat} is the saturation fluence and is inversely proportional to the electron mobility, given by:

$$F_{sat} = \frac{h\nu(1 + \sqrt{\epsilon_r})}{e(1 - R)\mu\eta_0} \quad (15)$$

From equation (14), we know that the near field of the radiation scales hyperbolically with the fluence. Therefore, by increasing the optical fluence, one can increase the generated THz electric field. But a saturation will occur as we increase the optical fluence, as demonstrated in Figure 6 (a) [15].

The bandgap of the 4H-SiC crystal is 3.26 eV, requiring the absorption of two photons at 400 nm to generate one electron-hole pair in the conduction band, known as the two-photon absorption (TPA) process. Since the current density is proportional to the square of the input intensity for the TPA process, the quadratic behavior is observed in Figure 6 (c) [15].

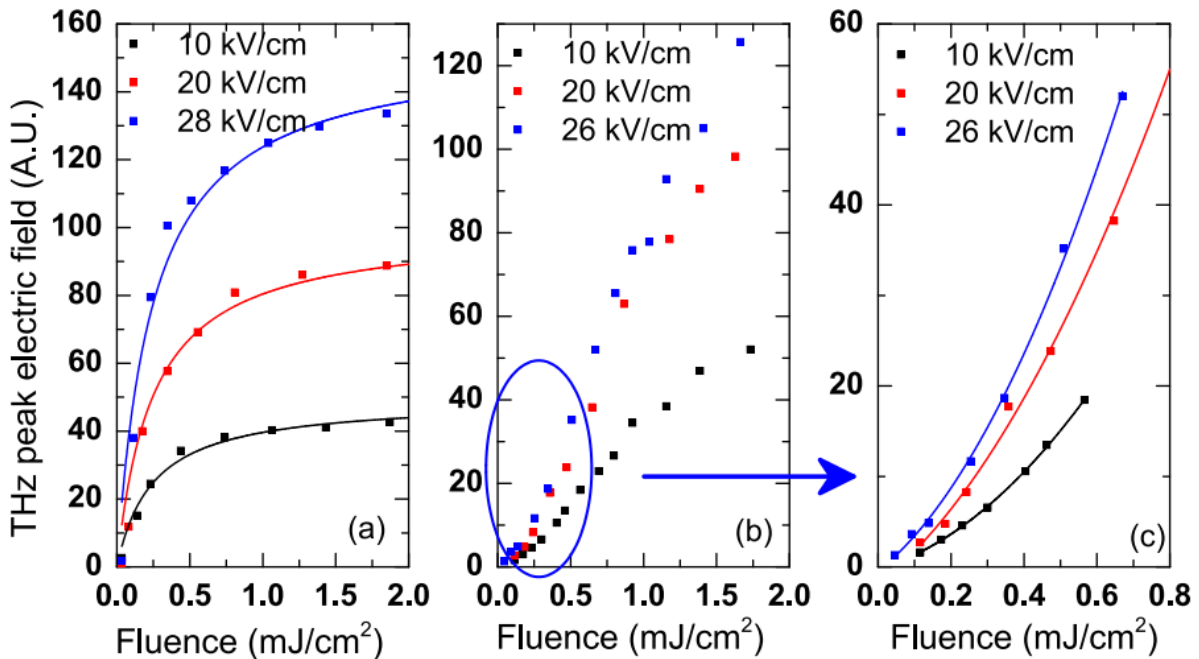


Figure 6. THz peak electric field versus fluence for a 6H-SiC (a) and 4H-SiC (b) PC antenna excited at 400 nm and biased with three different bias fields. (c) is an expanded scale of the bottom left part of (b), in order to show the quadratic dependence of the THz field on fluence for the 4H-SiC PCA at low excitation fluence [15].

Physically, when the optical fluence is small compared to the saturation fluence, the radiated near field scales almost linearly. On the contrary, when the optical fluence is high, the amplitude of the radiated near field saturates. As a result, the amplitude of the radiated near field is comparable to the amplitude of the bias electric field, thus screening the bias electric field itself. The THz pulse is emitted around the dipole with a polarization direction of the electric field

parallel to the dipole axis. It has the same direction as the surface current J , which is opposite to the direction of the bias electric field. When the PCA is operating in the screening regime, the only approach to increasing the amplitude of the radiated near field is to apply a higher bias field. The expression of far-field radiation is [65]:

$$E_{far}(t) \propto \frac{\partial J}{\partial t} \propto E_{bias} \frac{\partial \sigma}{\partial t} \quad (16)$$

As shown in equation (16), the THz electric field is proportional to the bias field E_{bias} and the time derivative of the surface conductivity σ . As can be seen from Figure 7 [56], carrier recombination is the dominating mechanism influencing the decay time of photocurrent. The temporal profile of the THz pulses depends on the rate at which the photocurrent increases and decreases.

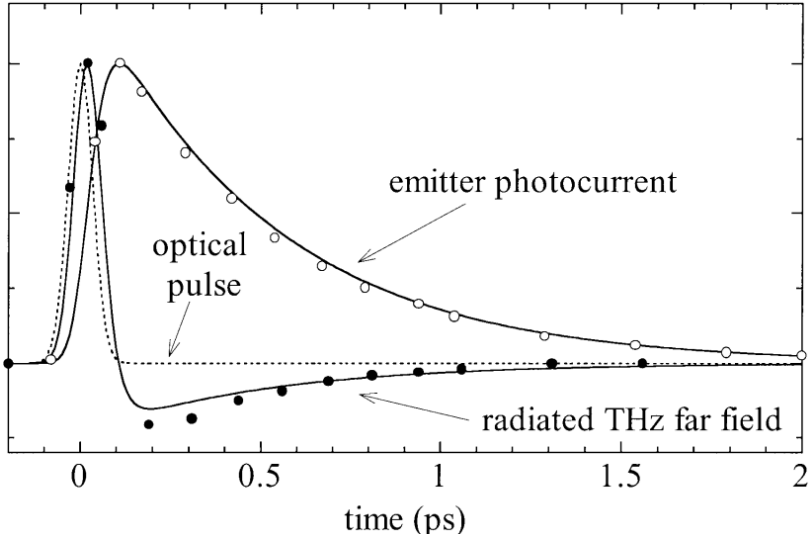


Figure 7. Calculated photocurrent, the amplitude of the radiated electric field and the laser pulse shape as a function of time [56].

The optical-to-THz conversion efficiency of PCAs is expressed by [66]:

$$\eta = \frac{\tau E_{bias}^2}{2F_{opt}\eta_0} \left(\frac{F_{opt}}{F_{opt} + F_{sat}} \right)^2 \quad (17)$$

Here, τ is the duration of the THz pulse. The efficiency of converting femtosecond laser to THz scales quadratically with the bias field. When the optical fluence is equal to the saturation fluence, the maximum optical-to-THz conversion efficiency is obtained:

$$\eta_{max} = \frac{\tau E_{bias}^2}{8F_{sat}\eta_0} \quad (18)$$

Consequently, we can obtain the energy of the THz pulses:

$$W_{THz} = \eta \times W_{opt} = \eta A F_{opt} \quad (19)$$

$$W_{THz}^{max} = \eta_{max} A F_{opt} = \frac{\tau A E_{bias}^2}{8\eta_0} \quad (20)$$

From equation (20), we conclude that the maximum THz energy only depends on the square of the bias field E_{bias}^2 and the area of the PCA A . In addition, in contrast to other THz sources, the energy of the THz pulse is extracted primarily from the DC field applied to the substrate instead of the optical pump. This characteristic is particularly advantageous for obtaining high optical-to-THz conversion efficiency while using relatively low optical energy.

The bandgap determines the laser wavelength that we can use to generate THz. To greatly improve the absorption of photons, the energy of the photons of the laser pulse must be slightly higher than the bandgap. It allows efficient absorption with high quantum efficiency and generates free carriers at the bottom of the conduction band. For example, the 3.03 eV bandgap of 6H-SiC allows 6H-SiC PCAs to be pumped efficiently with the second harmonic of the 800 nm Ti:sapphire laser.

Dielectric strength marks the highest bias electric field one can apply to a PCA before breakdown happens. The dielectric strength of semiconductors E_c is closely related to the bandgap E_G , given by an empirical formula [67]:

$$E_c = 1.36 \times 10^7 \left(\frac{E_G}{4} \right)^3 \quad (21)$$

Apparently, a small difference in bandgap will result in a huge variation in dielectric strength. This is significant for LAPCA since the radiated peak electric field is linearly proportional to the bias electric field. From this equation, we find that using a wide bandgap semiconductor as the substrate of LAPCA is very favorable.

From equations (15) and (17), we can conclude that if the carrier mobility increases, the saturation fluence will decrease, and the optical-to-THz conversion efficiency will increase. So we should use semiconductors with high carrier mobility as the LAPCA substrate. Table 2 demonstrates some basic physical properties of wide bandgap semiconductors including carrier mobility.

Table 2. Basic physical properties of wide bandgap semiconductors [102].

Semiconductor	ZnSe	GaN	6H-SiC	4H-SiC
Bandgap (eV)	2.7	3.28	3.01	3.23
Direct(D)/indirect(I)	D	D	I	I
Dielectric strength (MV cm ⁻¹)	1	4	3	3
Carrier mobility (cm ² V ⁻¹ S ⁻¹)	500	1000	400	800

As shown in Table 2, ZnSe, GaN, 6H-SiC and 4H-SiC all have large bandgaps, making them good candidates for substrates of LAPCA. Among them, GaN has a large bandgap of 3.28 eV, which is higher than 3.1 eV, preventing it from being pumped by the second harmonic of the 800 nm Ti:sapphire laser. However, it has been demonstrated that for $\text{In}_x\text{Ga}_{1-x}\text{N}$, by increasing the indium concentration to 15%, the bandgap of InGaN decreases to a value lower than 3.1 eV [68-71], as shown in Figure 8.

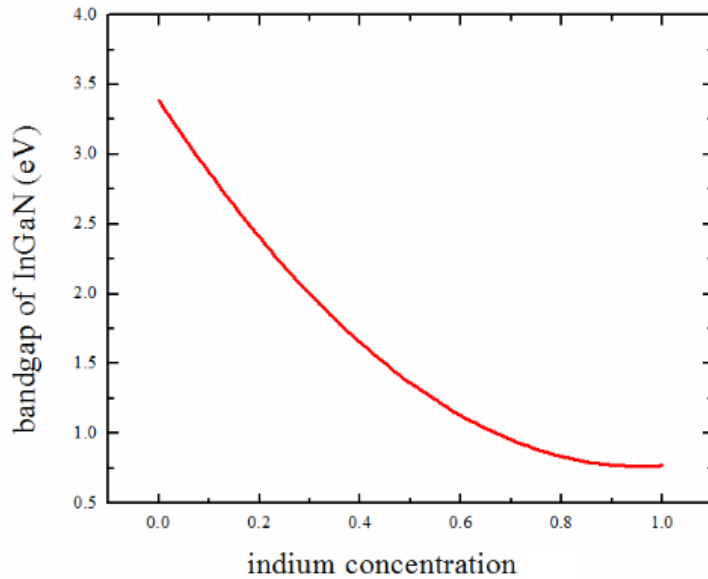


Figure 8. Bandgap of InGaN versus the indium concentration [70].

As can be seen in equation (15), saturation fluence F_{sat} is inversely proportional to the electron mobility. To increase the THz electric field, lower saturation fluence and higher electron mobility are desired. However, as shown in Figure 9, if we look at the data from [72] (dark blue dot), electron mobility decreases with increasing indium concentration. In Figure 9, the dashed blue curve shows the theoretical mobility, the inset shows the InGaN sample structure used in [72], and other data is obtained from [73-77]. Therefore, instead of choosing a high indium concentration, an indium concentration at which the bandgap of InGaN is slightly lower than 3.1 eV is preferred.

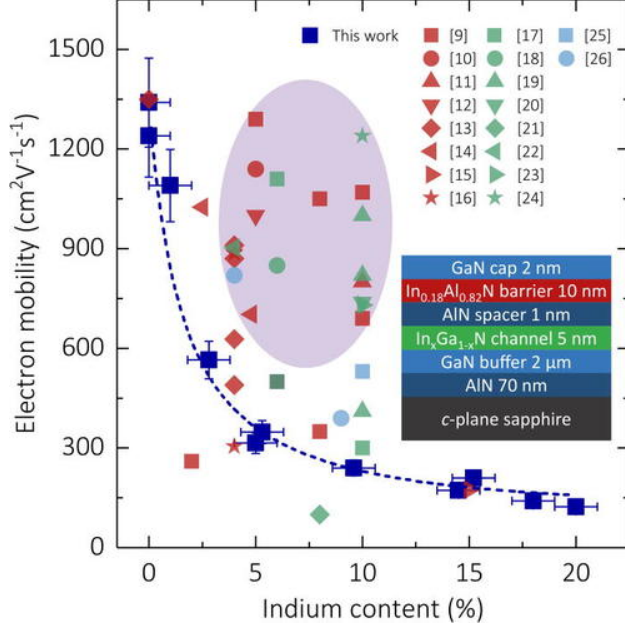


Figure 9. Electron mobility of the InGaN as a function of indium concentration [72].

A superb approach to generating intense THz radiation is to use interdigitated LAPCA (iLAPCA) structure, as shown in Figure 10 [54]. With non-interdigitated LPACA, higher-voltage supplies are necessary, which are dangerous and difficult to handle. However, iLAPCA possesses a large photoexcitation surface area, and due to the reduced distance between different pairs of electrodes, we can avoid applying high voltage in the experiment.

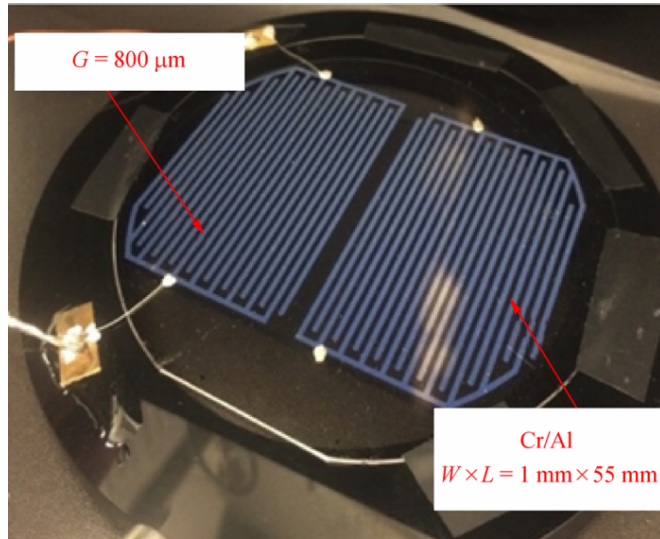


Figure 10. A typical 6H-SiC interdigitated LAPCA. Here, the iLAPCA is composed of 38 electrodes with a gap distance of 800 μm and a width and length of 1 and 55 mm, respectively [54].

For LAPCAs, two adjacent electrodes with the same gap size will generate THz pulses having opposite polarity, which can interfere destructively when propagating in the far-field. Therefore, it is necessary to block the illumination of all antennas biased with one specific bias field direction (positive or negative) by using a shadow mask. As shown in Figure 11 [13], with a shadow mask, constructive interference of pulses emitted with the same polarity will improve the overall far-field THz emission performance.

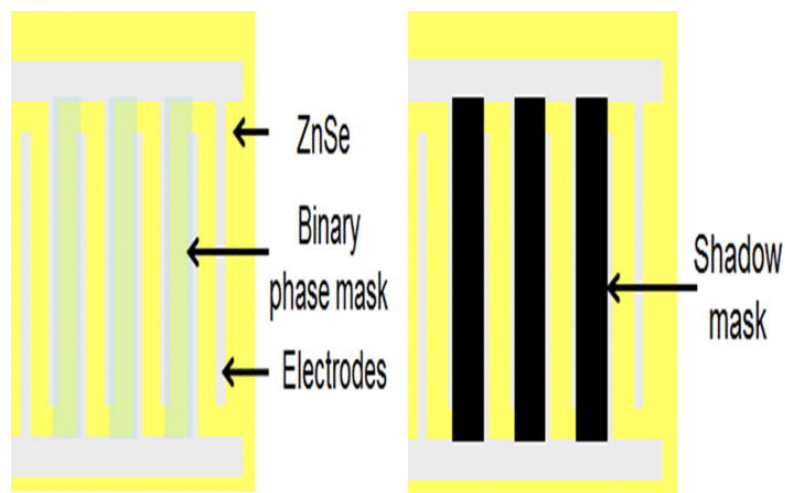


Figure 11. Schematic view of the interdigitated ZnSe antenna covered with a binary phase mask and shadow mask [13].

As shown in Figure 12 [13], the ZnSe interdigitated LAPCA with the shadow mask (blue curves) generates a half-cycle THz pulse. The THz waveform becomes symmetric and single-cycle with the 1 mm thick binary phase mask (red curve). Using a mask thickness of 0.65 mm instead of 1 mm reduces the THz pulse duration (black curve).

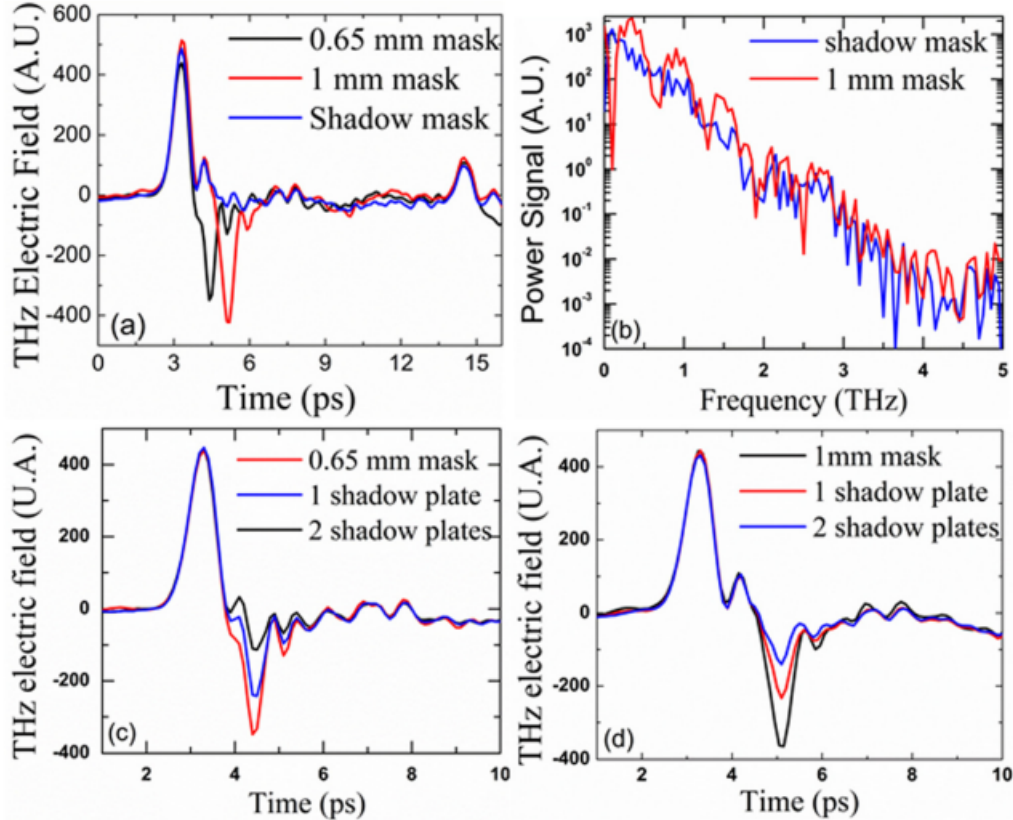


Figure 12. (a) THz pulses shapes generated from the ZnSe iLAPCA excited at 400 nm with a fluence of 0.2 mJ/cm^2 , at a bias field of 10 kV/cm with 0.65 and 1 mm binary mask and a shadow mask. (b) Power spectrum with a shadow mask (blue line) and the 1 mm binary mask (red line). (c) and (d) THz pulse shapes obtained with the 0.65 mm (c) and the 1 mm (d) binary mask on the ZnSe iLAPCA [13].

Using iLPCAs, THz pulses with MV/cm peak electric fields can be generated, and THz pulses with a 1 MV/cm field at 1 THz can accelerate free electrons up to 11 eV, which is sufficient to generate many nonlinear effects [14].

2.3 THz detection by PCAs

The PCA can also be used in THz detection [83,84]. A femtosecond probe laser pulse illuminates the gap of a PCA and excites carriers into the conduction band, and the excited carriers are accelerated by the THz electric field $E_{THz}(t')$. This leads to a transient photocurrent signal across the antenna gap. We can detect the THz electric field from the transient photocurrent using the lock-in amplifier.

More precisely, the femtosecond laser pulse creates free electrons in the antenna gap. When the THz pulse irradiates the antenna, the THz electric field induces a voltage between the two antenna electrodes. Driven by the THz induced voltage, a transient photocurrent flows through the gap. Subsequently, an electrical charge is shifted from one antenna electrode to the other. The amount of the transferred charge is proportional to the THz field strength. Therefore, we can detect the THz electric field from the photocurrent $I(t)$ with the amplifier connected to the PCA detector.

$$I(t) \propto \int_{-\infty}^t \sigma_s(t-t') E_{THz}(t') dt' \quad (22)$$

2.4 Free-space electro-optic sampling

Free-space electro-optic sampling exploits the linear Pockels effect in an electro-optic (EO) crystal together with a femtosecond laser pulse, to detect the electric field of the THz pulse [36,85-90]. The probe beam samples the THz electric field at a particular delay time. By varying the delay time, the entire THz transient waveform is mapped. A schematic view of this technique is shown in Figure 13.

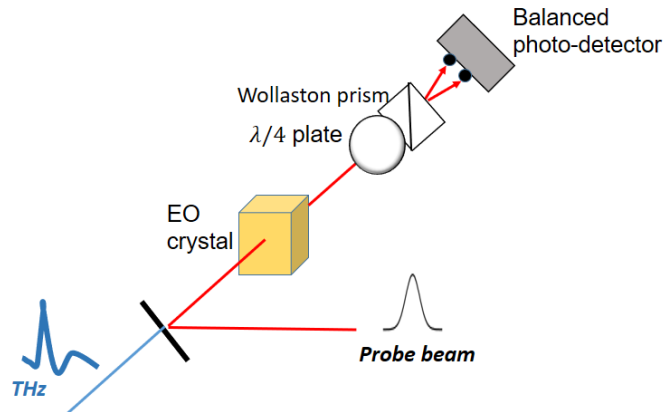


Figure 13. Schematic view of THz detection using the electro-optic sampling technique.

When there is no THz field, a linearly polarized femtosecond laser pulse traverses an EO crystal and passes through a $\lambda/4$ waveplate, and it becomes circularly polarized. The orthogonal polarization components of the laser pulse are then equally separated by a Wollaston prism and sent to the balanced photo-detector. The detector is connected to a lock-in amplifier, which measures the difference signal $I_y - I_x$ from the two photodiodes and gives a zero reading.

However, when the THz field overlaps the femtosecond laser pulse in time, the polarization of the laser beam is modified slightly, introducing an imbalance between I_y and I_x . The difference between the two signals is proportional to the THz electric field, for example, for ZnTe crystal, we can obtain equation (23) [36]:

$$I_s = I_y - I_x = I_0 \Delta\phi = \frac{I_0 \omega L}{c} n_o^3 r_{41} E_{THz} \propto E_{THz} \quad (23)$$

Here

$$I_x = \frac{I_0}{2} (1 - \sin \Delta\phi) \approx \frac{I_0}{2} (1 - \Delta\phi) \quad (24)$$

$$I_y = \frac{I_0}{2} (1 + \sin \Delta\phi) \approx \frac{I_0}{2} (1 + \Delta\phi) \quad (25)$$

Where I_0 is the intensity of the incident probe, n_o is the refractive index at the optical frequency, r_{41} is the EO coefficient, and $\Delta\phi$ is phase retardation between the two polarization components ($\Delta\phi \ll 1$). Thus, by measuring the signal of the balanced photo-detector, the THz electric field strength can be determined.

2.5 THz time-domain spectroscopy (THz-TDS)

2.5.1 Introduction

THz time-domain spectroscopy (THz-TDS) is a spectroscopic technique in which the properties of matter are detected with short pulses of THz radiation. Since THz-TDS determines both the amplitude and the phase of the THz radiation, it can be perfectly utilized in assessing the complex dielectric constants of various materials [92-100].

The complex index of refraction of the sample is given by $\hat{n}(\omega) = n(\omega) + i\kappa(\omega)$, here, $\kappa(\omega)$ is the extinction coefficient, related to the absorption coefficient $\alpha(\omega)$ through $\kappa(\omega) = \alpha(\omega)c/(2\omega)$. Considering Fresnel field transmission and reflection for normal incidence, we can obtain the following formulas:

$$n(\omega) = 1 + \frac{\varphi(\omega)c}{\omega d} \quad (26)$$

$$\alpha(\omega) = -\frac{2}{d} \ln \left(\frac{(n+1)^2}{4n} T(\omega) \right) \quad (27)$$

Here, n is the real part of the index of refraction, α is the absorption coefficient, and ω is the angular frequency. $\varphi(\omega) = \varphi_{sam}(\omega) - \varphi_{ref}(\omega)$, where $\varphi_{sam}(\omega)$ and $\varphi_{ref}(\omega)$ are the

unwrapped phase of sample signal and unwrapped phase of reference signal obtained from Fourier transform. Also c is the velocity of light in vacuum, and d is the thickness of the sample. $T(\omega) = \frac{E_{sam}}{E_{ref}}$, where E_{sam} and E_{ref} are the amplitude of sample signal and amplitude of reference signal obtained from Fourier transform.

In THz-TDS measurements, the experimental conditions should be identical for sample and reference measurements. For example, a holder is put at the focal point of the THz beam in reference measurement, since we put the sample on a holder in sample measurement. Further, in the THz-TDS system, the optical length of the pump line and the probe line should be approximately equal.

In this chapter, we will present a THz-TDS system based on the PCA emitter and PCA detector, along with the experimental results of CdTe and ZnTe characterization.

2.5.2 THz-TDS system based on PCA emitter and PCA detector

To obtain the THz signal with broad bandwidth, we use a free space PCA THz emitter (TERAVIL EMT-10) and free space PCA THz detector (TERAVIL DET-10). The PCA is based on GaBiAs photoconductive material and is optimized for wavelengths around 1060 nm, which matches the wavelength of the ytterbium laser (Newport Spectra-Physics HighQ-2). It also has a wide spectral range and low noise level with sub-picosecond temporal resolution. The THz emitter consists of a microstrip PCA fabricated on GaAs substrate, which is illuminated by laser beams from the panel side. Laser beams must be focused on the gap between two electrodes. Typically, the laser spot is smaller than the gap between metallic electrodes. THz radiation is collected by an integrated lens, manufactured from high-resistivity silicon.

To align the PCA emitter and detector, a CCD camera is used to take images of the electrodes. As shown in Figure 14, the antenna gap can be observed clearly. The idea of aligning is to make the pump and probe beam focused on the gap. Afterward, we measure the resistivity with and without laser illumination. In theory, the resistivity is very high when there is no laser illumination since the substrate is semi-insulating. However, when the laser is focused on the antenna, the resistivity decreases dramatically, since the photons are absorbed by the substrate, exciting carriers from the valence band to the conduction band.

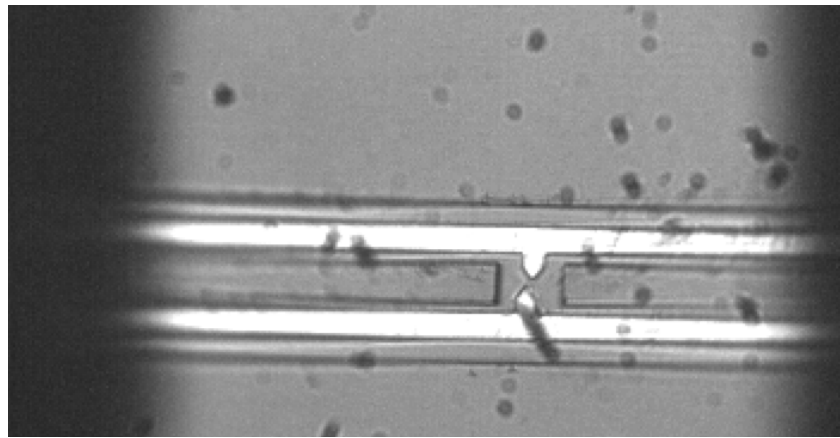


Figure 14. CCD image of the PCA emitter.

The schematic of the THz-TDS system using the PCA emitter and PCA detector is shown in Figure 15.

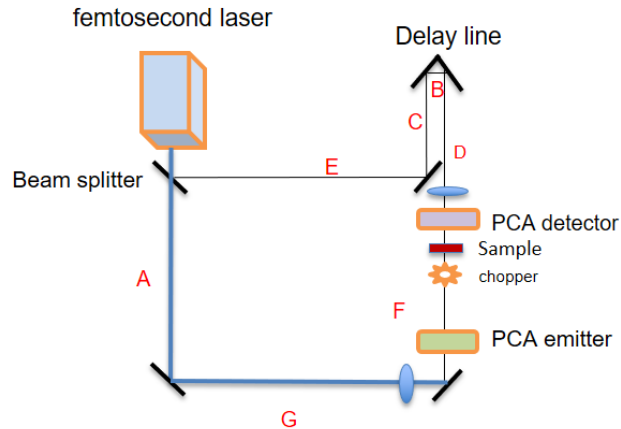


Figure 15. Schematic of THz-TDS system using the PCA emitter and PCA detector.

Figure 16 shows the THz waveforms generated and detected using GaBiAs PCA emitter and detector. Both of them are pumped by the 1045 nm laser with 20 mW optical power. We optimized the THz-TDS system by adjusting the position of the silicon lens installed before the PCA. After optimization, the peak electric field increases more than 2 times, and the THz pulse duration decreases from 2 ps to 1.5 ps. The bandwidth is 2 THz.

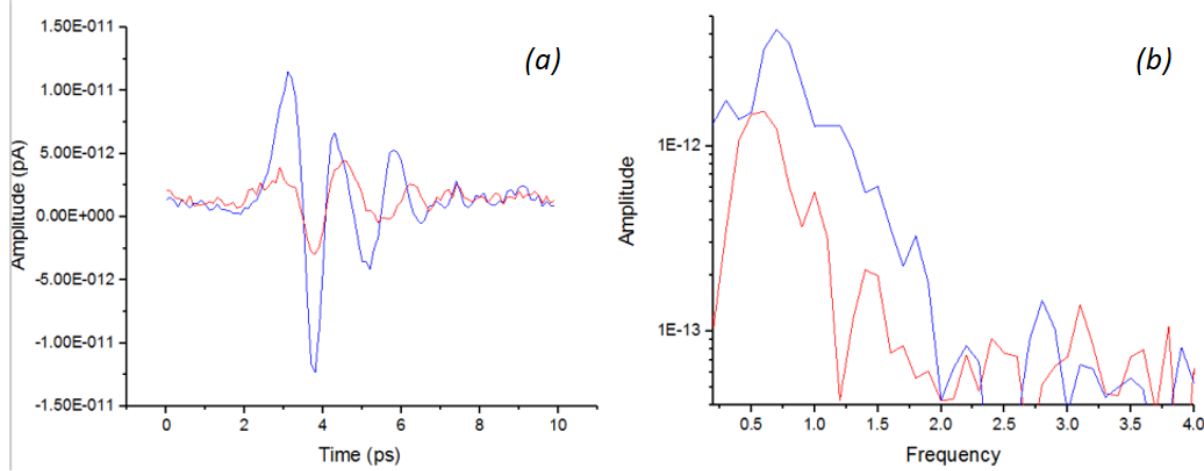


Figure 16. (a) THz waveforms and (b) amplitude spectrum, generated and detected by Teravil's GaBiAs PCA emitter and detector before (red) and after (blue) rough alignment of the HR Si lenses.

2.5.3 Phase retrieval in THz-TDS

To get the phase difference between the sample and the reference signal $\varphi(\omega)$, phase unwrapping is needed. In principle, the unwrapped phase curves of the sample and reference signal should be monotonically increasing in the frequency domain, and the phase difference $\varphi(\omega)$ is always greater than zero. We can obtain the unwrapped phase from Origin software, but this software can give us systematic errors, as shown in Figure 18 (a), the unwrapped phase of the sample signal is erroneous.

The errors can be corrected automatically by subtracting the overall phase of the signals from the wrapped phase before unwrapping, and then adding the same phase after unwrapping. This reduced phase is best calculated by multiplying the complex-valued spectra by $\exp(-i\varphi_{0sam})$ and $\exp(-i\varphi_{0ref})$, respectively, before unwrapping [91]. Here, the overall phase $\varphi_{0sam} = 2\pi ft_{0sam}$, $\varphi_{0ref} = 2\pi ft_{0ref}$, noting that the position of the peak of the THz signal is at time t_0 , as shown in Figure 17 (a).

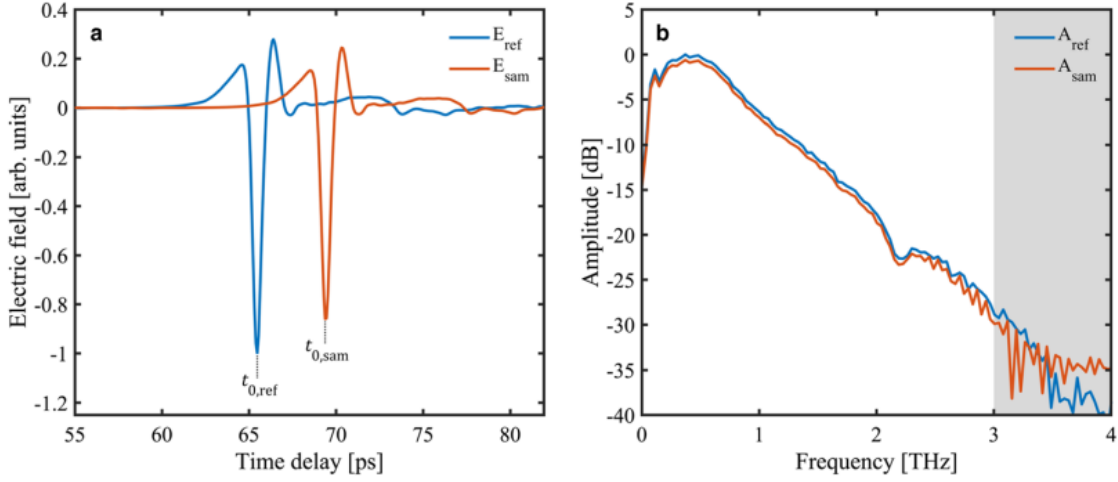


Figure 17. (a) Typical waveform for a THz-TDS experiment. The blue curve is the measurement of reference through air, and the red curve is the measurement of the sample. (b) The frequency spectrum. The gray-shaded area represents the upper limit of the useful spectral region of the measurements [91].

The strategy for the most stable phase unwrapping is to ensure that the slope of the phase to be unwrapped is as low as possible, in order to minimize the possibility of unintentional overcompensation of the phase [91]. As shown in Figure 18 (b), with the inclusion of the overall phase of the signals in the unwrapping procedure, unwrapping now works as expected, since the subtraction of the overall phases of the signals leads to relatively small variations of the phase spectrum.

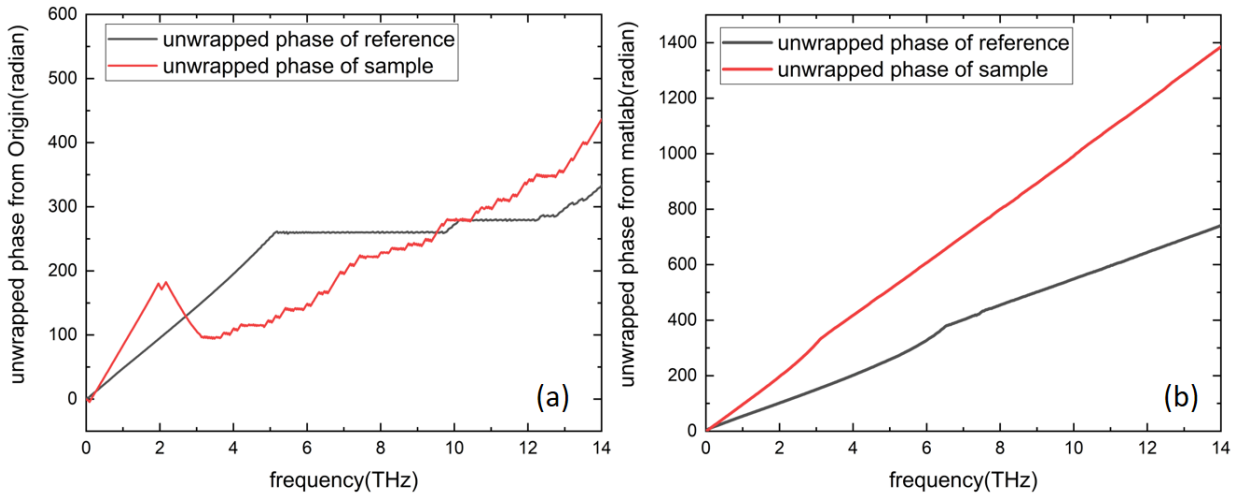


Figure 18. Unwrapped phase (a) from Origin (before correction), (b) from MATLAB (after correction).

In principle, the unwrapped phase should be zero when the frequency is zero. Otherwise, the calculated index of refraction will tend to infinity, which is incorrect. However, sometimes the unwrapped phase does not start with zero, which indicates that there is a global phase offset (integer multiples of 2π). To solve this problem, we can first check if there is a global phase offset using the linear regression method in MATLAB. If there is a global phase offset, we need to subtract it from the unwrapped phase [91].

The index of refraction can be calculated using the phase delay φ , and $\varphi = [n(\omega) - 1]\omega d/c$, as shown in Figure 19 (a). The phase delay φ can be calculated using the temporal offset of the reference and sample THz pulses, that is, $\varphi = \varphi_{0sam} - \varphi_{0ref} = 2\pi f(t_{0sam} - t_{0ref})$, where t_{0sam} is the temporal position of the maximum value of the sample THz pulses, and t_{0ref} is the temporal position of the maximum value of the reference THz pulses. We can estimate the index of refraction by substituting the phase difference φ into the following equation:

$$n(\omega) = 1 + \frac{\varphi c}{\omega d} \quad (28)$$

The estimated index of refraction shows no variation in the whole THz frequency range, which does not reflect the interaction between the THz radiation and the sample. For example, the estimated index of refraction of a silicon wafer is about 3.4 in the THz frequency range.

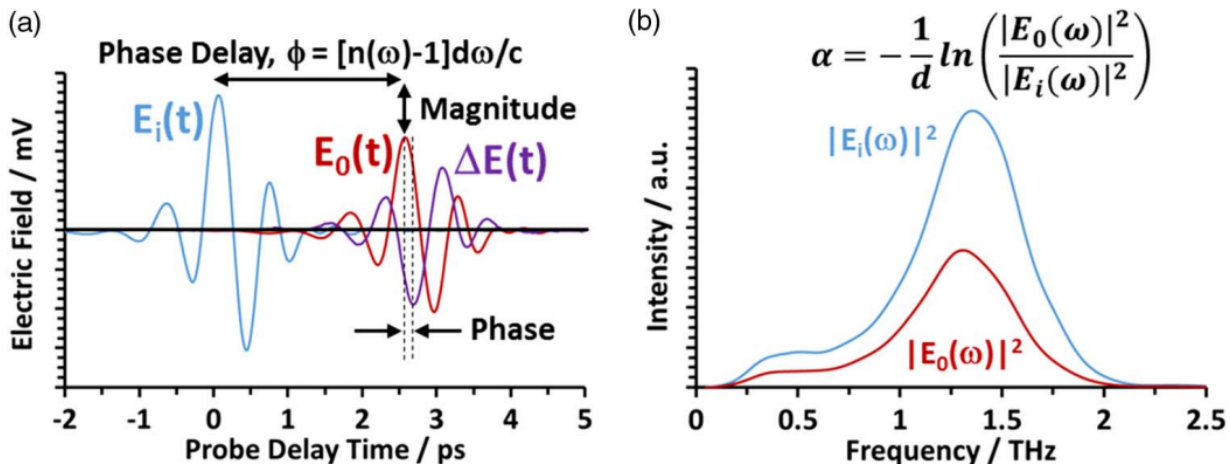


Figure 19. (a) Representation of time-domain electric field waveforms measured by THz-TDS and time-resolved terahertz spectroscopy (TRTS). (b) Corresponding frequency-domain intensity spectra obtained from the Fast Fourier transform (FFT) [101].

2.5.4 THz-TDS of CdTe sample

A THz-TDS measurement of 1 mm CdTe sample is done at École de technologie supérieure (ÉTS). The system is based on the PCA emitter and PCA detector, both of which are pumped by the 800 nm laser with 20 mW optical power. The electric field, amplitude spectrum and unwrapped phase of the THz signal are shown in Figure 20, Figure 21 and Figure 22, respectively.

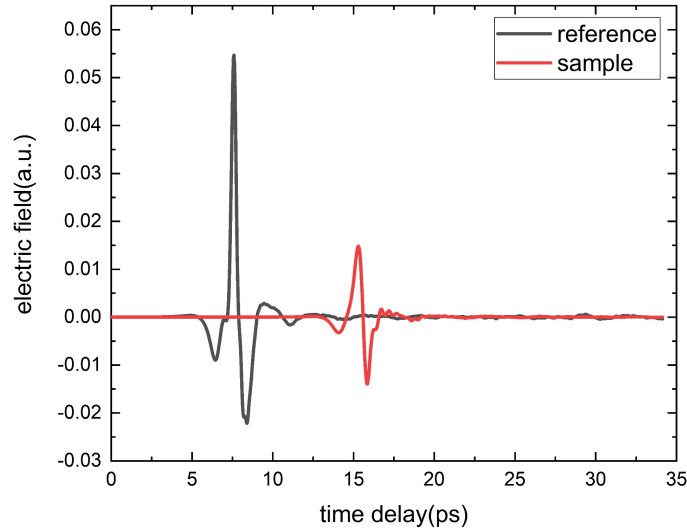


Figure 20. Electric field of THz signal in THz-TDS measurement of the 1 mm CdTe sample.

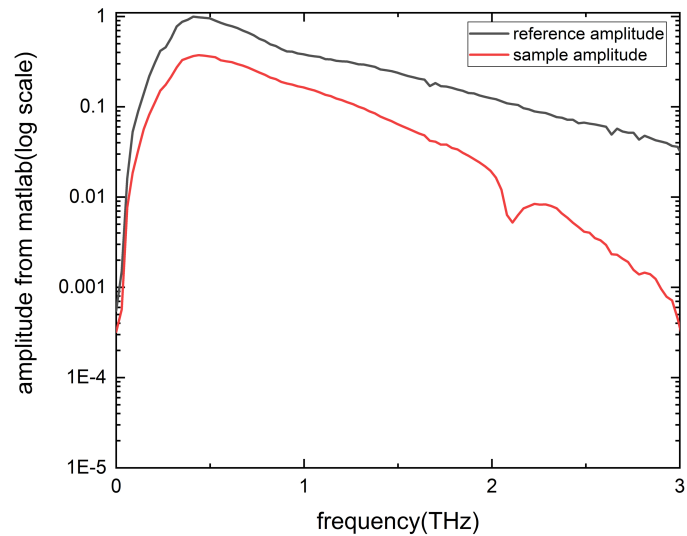


Figure 21. Amplitude spectrum of THz signal in THz-TDS measurement of the 1 mm CdTe sample.

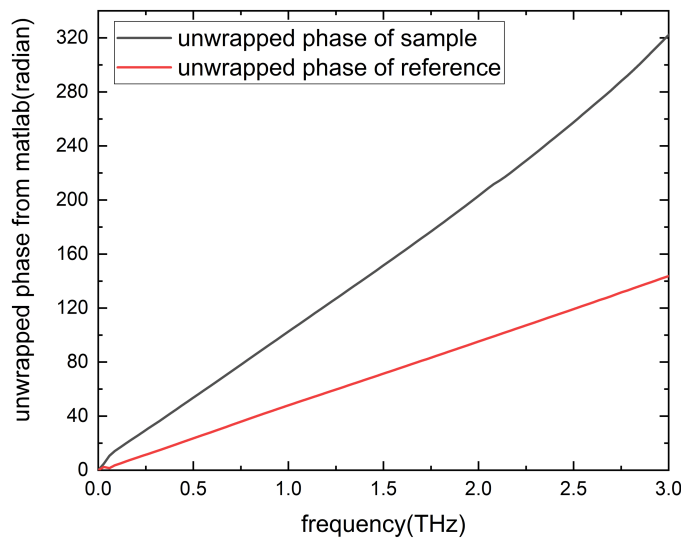


Figure 22. Unwrapped phase of THz signal in THz-TDS measurement of the 1 mm CdTe sample.

The calculated index of refraction and absorption coefficient results are shown in Figure 23 and Figure 24, respectively.

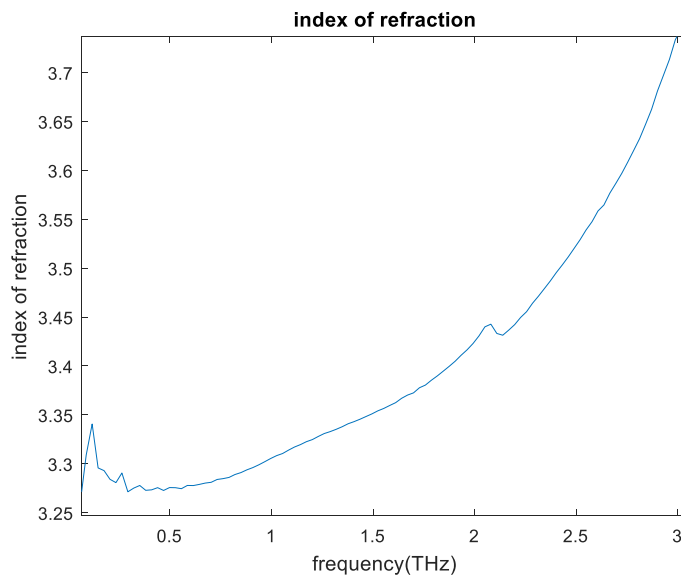


Figure 23. Index of refraction of the 1 mm CdTe sample.

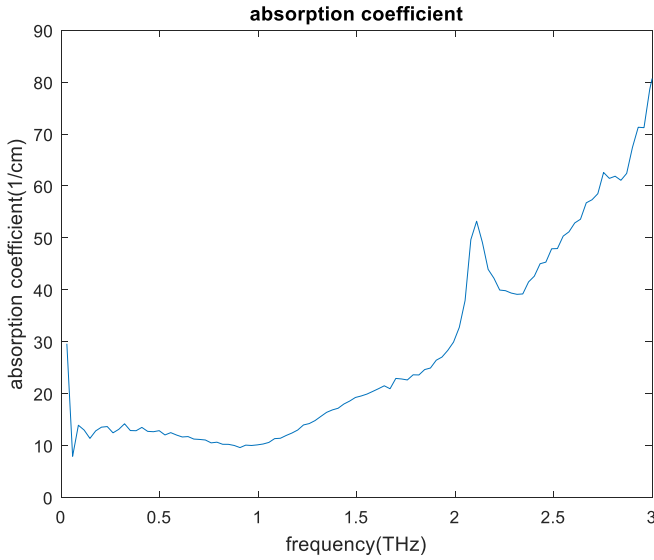


Figure 24. Absorption coefficient of the 1 mm CdTe sample.

As shown in Figure 25 (B), our results for the characterization of CdTe are very close to the literature. The rise in the refractive index and absorption is due to the TO phonon resonance at 141 cm^{-1} in CdTe. A sharp resonance at 2.1 THz (70 cm^{-1}) appears superimposed on the Lorentzian absorption profile. It is suggested that second-order phonon processes are responsible for the features [105].

The accuracy of the measurement is mainly limited by the uncertainty in measuring the thickness of the samples. Oscillation in the index of refraction curve at low frequency (below 0.5 THz) might originate from slightly different diffraction environments of the THz beam through the sample and reference apertures [108].

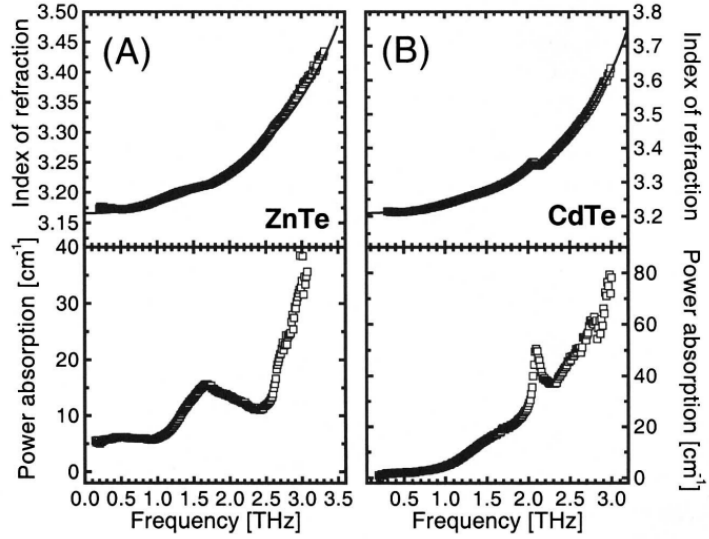


Figure 25. Index of refraction and absorption coefficient of (A) ZnTe and (B) CdTe from literature [105].

A preprocessing method known as zero-padding is used before analyzing the data. That is, the beginning and the end of THz pulses are set to zero. As a result, the oscillation in the amplitude is mitigated, as shown in Figure 26.

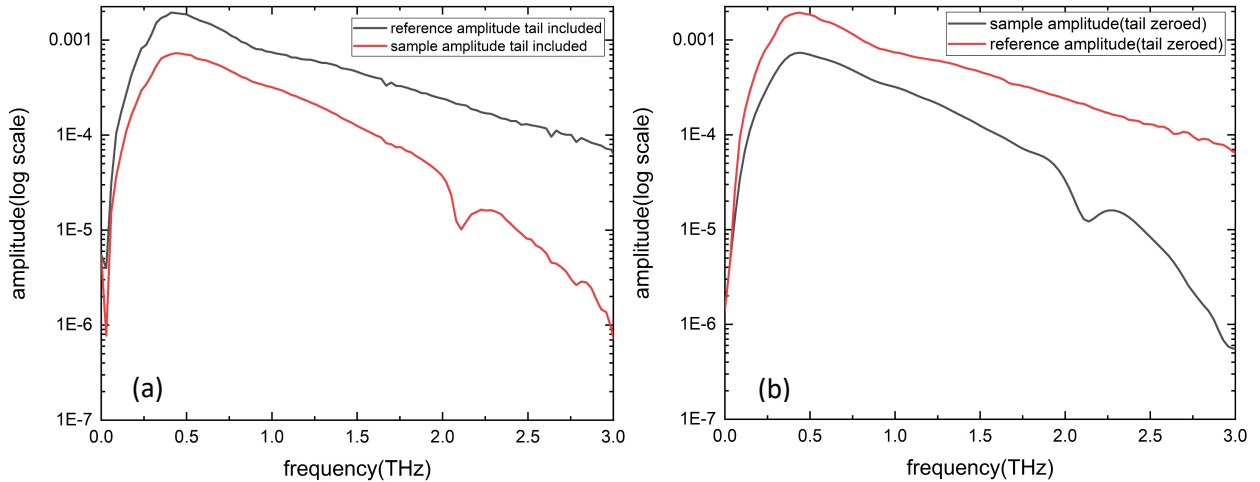


Figure 26. (a) Amplitude when the end of THz pulse is included. (b) Amplitude when the end of THz pulse is set to zero. When the end of the THz pulse is set to zero, the oscillation in the amplitude is mitigated.

The zero-padding method can improve the Fast Fourier transform (FFT) results (both amplitude and phase spectrum), mitigating the oscillation in the absorption coefficient when the end of the THz pulse is set to zero, as shown in Figure 27.

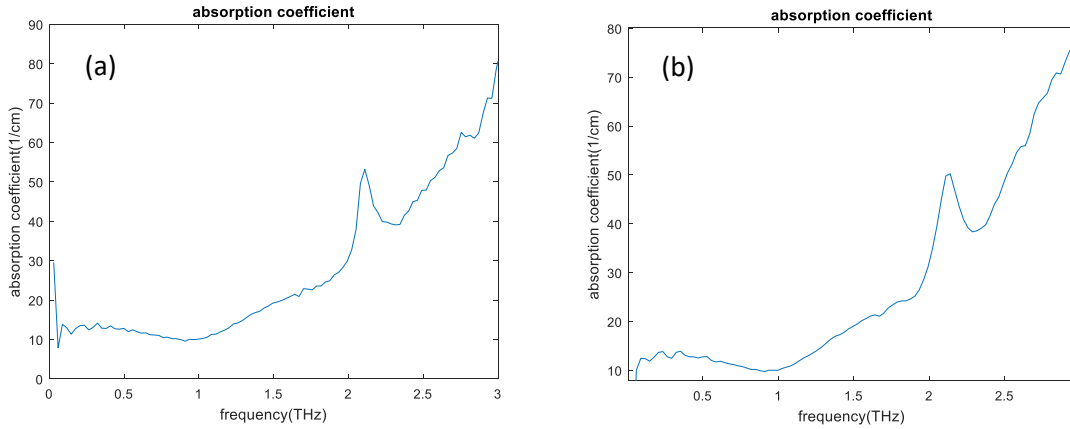


Figure 27. (a) Absorption coefficient when the end of THz pulse is included. (b) Absorption coefficient when the end of THz pulse is set to zero. The oscillation is mitigated when the end of the THz pulse is set to zero.

Dynamic range (DR) is defined as the ratio of the maximum measurable signal to the standard deviation of the noise signal. The calculated absorption coefficient will be considered accurate only when it is below the dynamic range. Figure 28 shows the largest absorption coefficient that can be measured reliably.

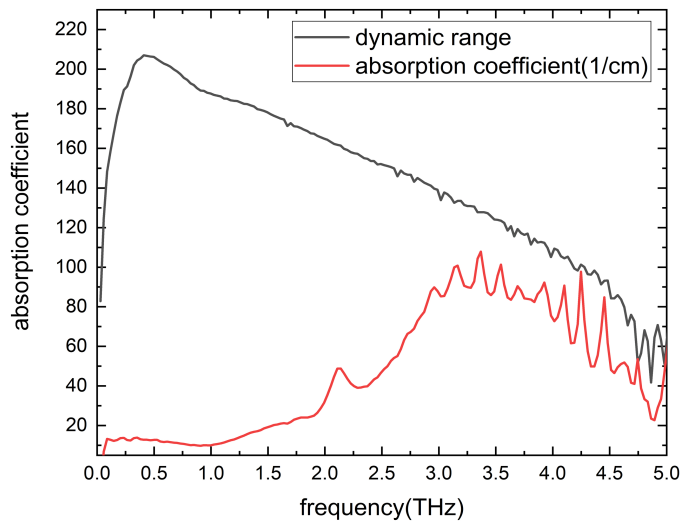


Figure 28. The upper limit of the detectable absorption of CdTe (dynamic range).

In this experiment, there is considerable noise when the frequency is above 3 THz, so we do not analyze the index of refraction and absorption coefficient after 3 THz. As shown in Figure 28, the calculated absorption coefficient is below the dynamic range between 0 and 3 THz, so the measurement can be considered accurate.

2.5.5 THz-TDS of ZnTe sample

A measurement of a 2 mm ZnTe sample was done using 0.8 mm CdTe crystal as THz emitter and PCA as THz detector. The schematic of the setup is shown in Figure 29. In the THz-TDS system, the optical length of the pump line and the optical length of the probe line should be approximately equal. Here, a nonlinear crystal is used as the THz emitter, so the black polyethylene is put behind the emitter to decrease laser leakage, thus increasing the signal-to-noise ratio (SNR).

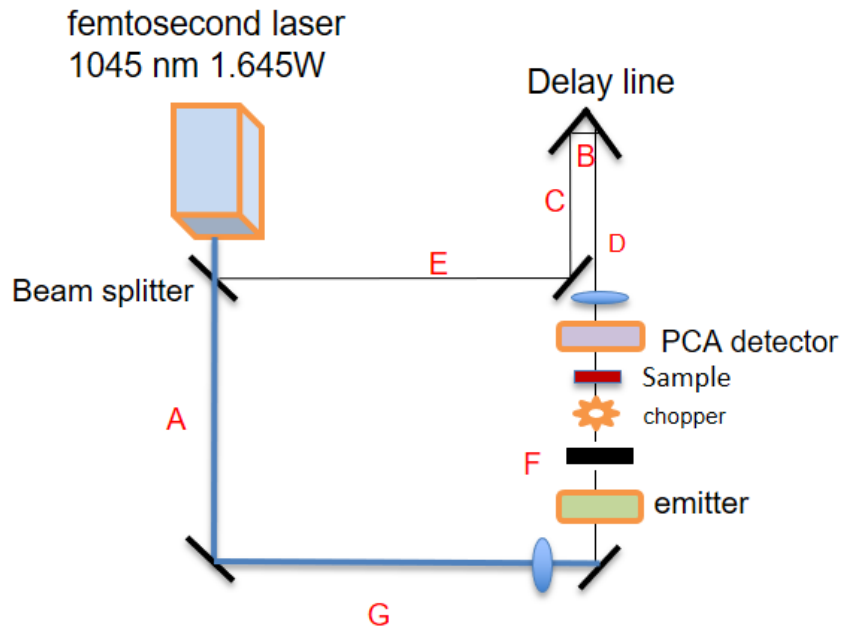


Figure 29. Schematic of the THz-TDS system using a nonlinear crystal as the THz emitter and the PCA as the THz detector.

The CdTe emitter is pumped by the 1045 nm laser with 500 mW of optical power, and the PCA detector is pumped by the 1045 nm laser with 20 mW power. The electric field, amplitude

spectrum and unwrapped phase of the THz signal are shown in Figure 30, Figure 31 and Figure 32, respectively.

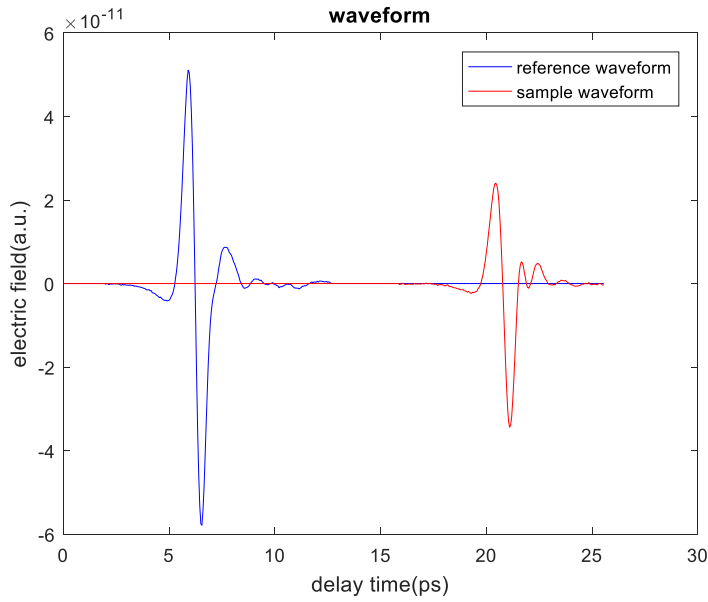


Figure 30. Electric field of THz signal in THz-TDS measurement of the 2 mm ZnTe sample.

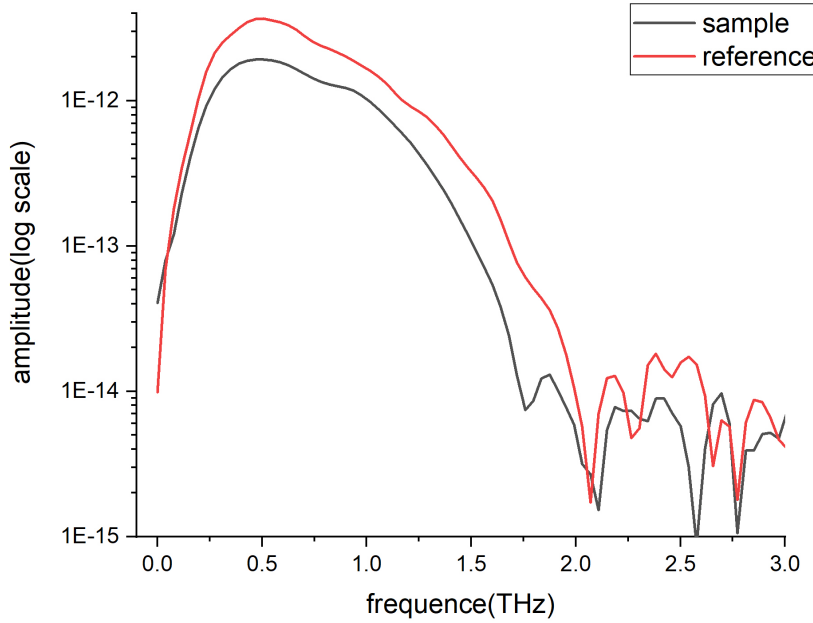


Figure 31. Amplitude of THz signal in THz-TDS measurement of the 2 mm ZnTe sample.

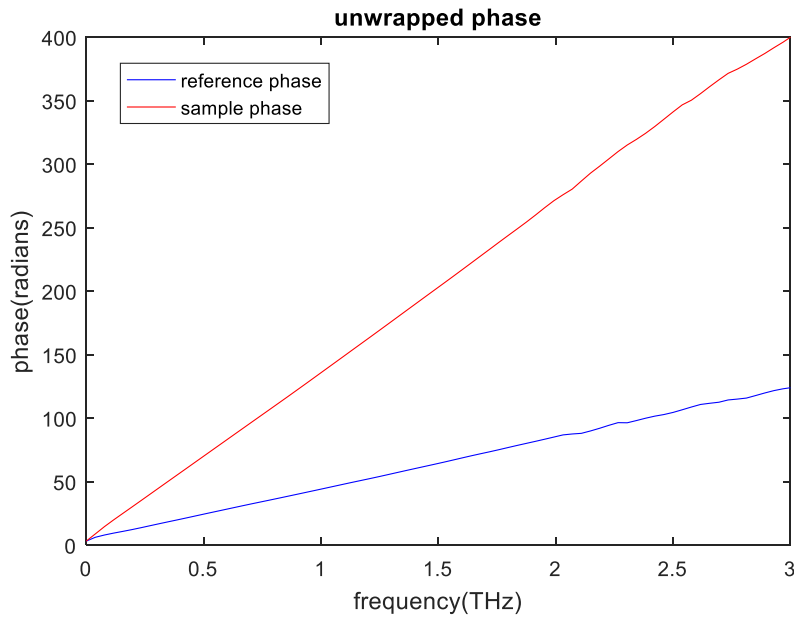


Figure 32. Unwrapped phase of THz signal in THz-TDS measurement of the 2 mm ZnTe sample.

The calculated index of refraction and absorption coefficient of the 2 mm ZnTe sample are shown in Figure 33 and Figure 34, respectively.

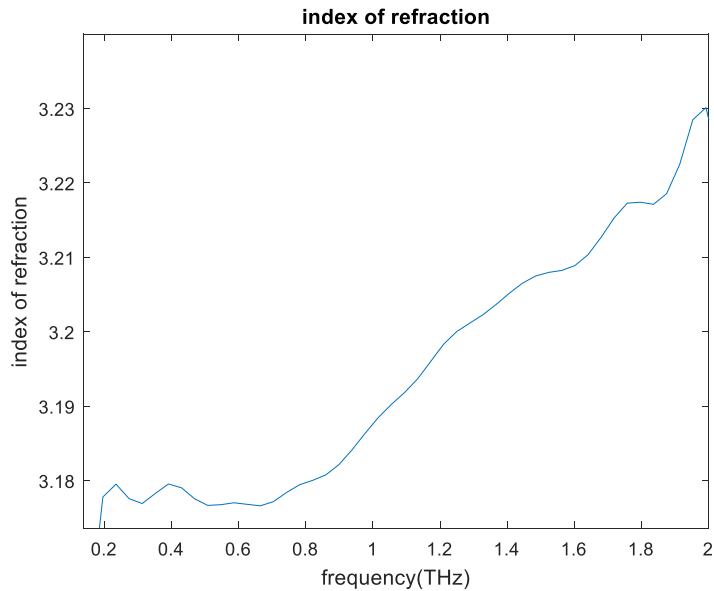


Figure 33. Index of refraction of the 2 mm ZnTe sample.

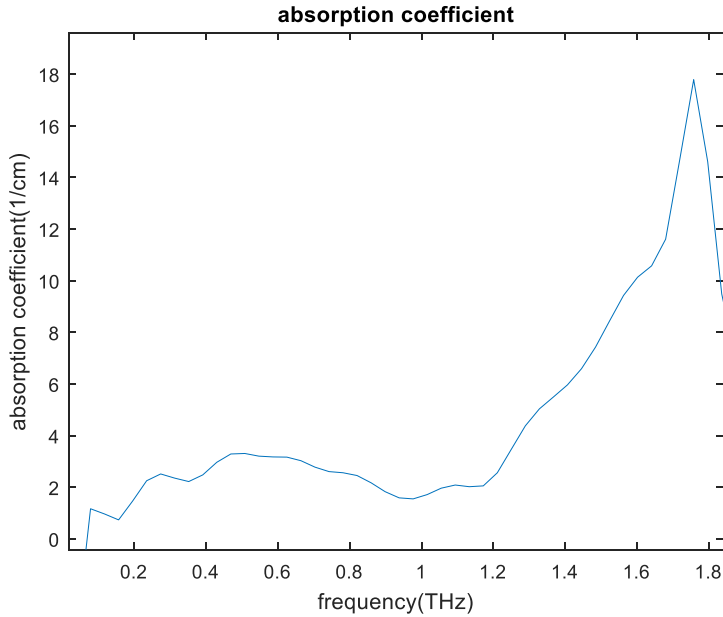


Figure 34. Absorption coefficient of the 2 mm ZnTe sample.

As shown in Figure 25 (A), our results for the characterization of ZnTe are very close to the literature between 0.2 to 1.8 THz. The rise in the refractive index and absorption is due to the TO phonon resonance at 177 cm^{-1} in ZnTe [105].

Figure 35 shows the largest absorption coefficient that can be measured reliably. Here the absorption coefficient is below the dynamic range (alphamax) between 0.2 and 1.8 THz, so the calculated absorption coefficient can be considered accurate.

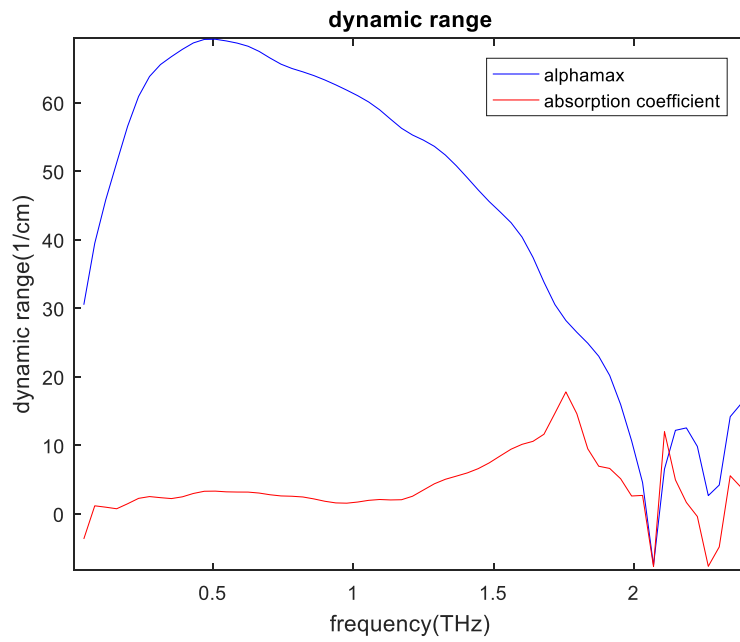


Figure 35. The upper limit of the detectable absorption of the 2 mm ZnTe sample (dynamic range).

Chapter 3

Increasing the THz intensity generated from LAPCA

3.1 introduction

The large aperture photoconductive antenna (LAPCA) is an efficient and compact table-top THz source. With the laser facilities of the Advanced Laser Light Source (ALLS) at the INRS-EMT, the generated THz pulse energies from LAPCAs are getting more and more intense, increasing from a few nJ up to several μJ , making it possible to study a lot of fascinating nonlinear phenomena and novel applications, such as the intraband and interband carrier dynamics [5] and nonlinear transmission enhancement of THz pulses in n-doped semiconductors [1,3].

We can fabricate PCAs using semiconductors with a bandgap slightly lower than the energy of the photons of the laser pulse, which allows efficient absorption with high quantum efficiency. It is also very promising that by covering the PCA with insulators like TiO_2 , Si_3N_4 and Al_2O_3 , we can avoid air breakdown, thus increasing the bias field we can apply [14,77-80]. In the previous chapters, we demonstrate that the generated THz electric field is proportional to the applied bias field, so by increasing the applied bias field, we can increase the generated THz electric field. Further, the insulator layer has less reflectivity compared to the substrate, so more carriers can be generated in the substrate [78]. The THz electric field will be enhanced due to the increase in the carrier density.

In this study, we will discuss the fabrication of PCAs on high-resistivity semiconductor substrates, the breakdown field of GaAs PCAs with and without insulator coating, as well as the THz generation from the GaAs-based PCA after surface passivation.

3.2 Paschen's law

Breakdown voltage is the minimum voltage needed for an electric arc or discharge between two electrodes in a gas as a function of pressure and gap size. And Paschen's law is an equation that gives the breakdown voltage, named after Friedrich Paschen, who discovered it empirically in 1889 [57]. The breakdown voltage can be expressed by the following equation:

$$V_B = \frac{Bpd}{\ln(Apd) - \ln \left[\ln \left(1 + \frac{1}{\gamma_{se}} \right) \right]} \quad (29)$$

where V_B is the breakdown voltage in volts, p is the pressure in pascals, d is the gap distance in meters, γ_{se} is the secondary-electron-emission coefficient, A is the saturation ionization in the gas, and B is related to the excitation and ionization energies. Paschen curves can be obtained using equation (29) [58,82], as shown in Figure 36.

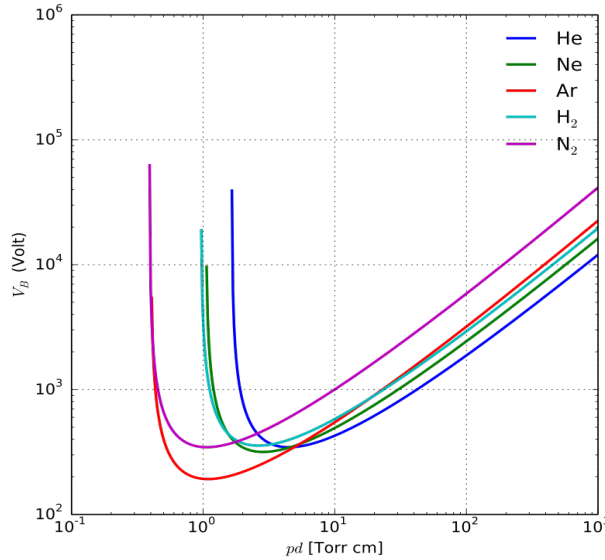


Figure 36. Paschen curves obtained for helium, neon, argon, hydrogen and nitrogen, using the expression for the breakdown voltage [58].

For a given gas, the voltage is only related to the product of the pressure and gap distance. In this study, we use a gap size of 0.9066 mm, which is a relatively large gap distance. At atmospheric pressure, the breakdown voltage scales almost linearly with the product of pressure and gap distance.

When air breakdown happens, the air is ionized, and it becomes an electrical conductor, preventing the PCAs from working. To generate intense THz radiation, we need to apply high bias fields beyond the air breakdown limit by surface passivation.

3.3 Breakdown field of GaAs-based PCA

Gallium arsenide (GaAs) is a III-V direct bandgap semiconductor with a Zincblende structure, with a bandgap $E_g = 1.42 \text{ eV}$. The band structure of GaAs at a temperature of 300 K is shown in Figure 37 [61], indicating important satellite valleys at the L and X points, located 1.71 eV and 1.90 eV above the valence band maximum at the Γ point. Understanding the band structure is important when studying the electronic properties of semiconductors, since it determines the effective mass of a charge carrier, and also since it indicates whether a carrier can scatter into a lower-mobility satellite valley.

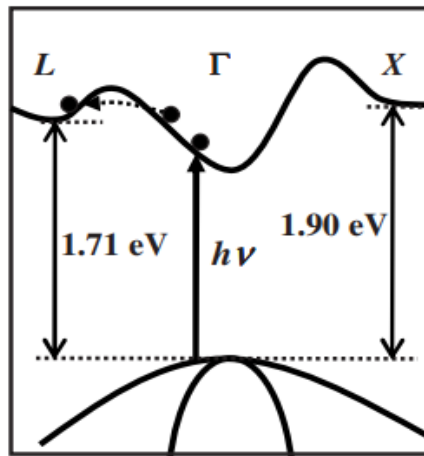


Figure 37. The schematic view of GaAs band structure. Optical photons can excite electrons directly into the Γ valley [61].

GaAs has some electronic properties superior to those of silicon. It is used to manufacture devices such as microwave frequency integrated circuits, infrared light-emitting diodes, laser diodes, solar cells and optical windows. Moreover, it has been widely used for various transistor types [59], such as a high-electron-mobility transistor (HEMT), junction field-effect transistor (JFET) and metal-oxide-semiconductor field-effect transistor (MOSFET) [60]. Table 3 summarizes some electrical properties of GaAs.

Table 3. Basic physical properties of GaAs.

Semiconductor	GaAs
Electron diffusion coefficient (cm^2s^{-1})	≤ 200
Electron thermal velocity (m/s)	4.4×10^5
Breakdown field (MV/cm)	0.6
Electrons mobility ($\text{cm}^2\text{V}^{-1}\text{S}^{-1}$)	≤ 8500

We use high-resistivity GaAs substrates (MTI Corporation GAUa101005S2US) to fabricate PCAs. The GaAs is undoped with two sides polished and grown by the vertical gradient freeze (VGF) method with a dimension of $10 \times 10 \times 0.5$ mm. The orientation is (100), and the resistivity is $0.6\sim 2 \times 10^8 \Omega \cdot cm$. In theory, GaAs has a dielectric strength of 0.6 MV/cm [103]. It is higher than the air breakdown field, which is 30 kV/cm [104]. We will experimentally test the dielectric strength of the GaAs sample in this work.

To fabricate PCAs through photolithography, we need first to make a design in AutoCAD. As shown in Figure 38, a PCA with a large gap size of 0.9066 mm is presented.

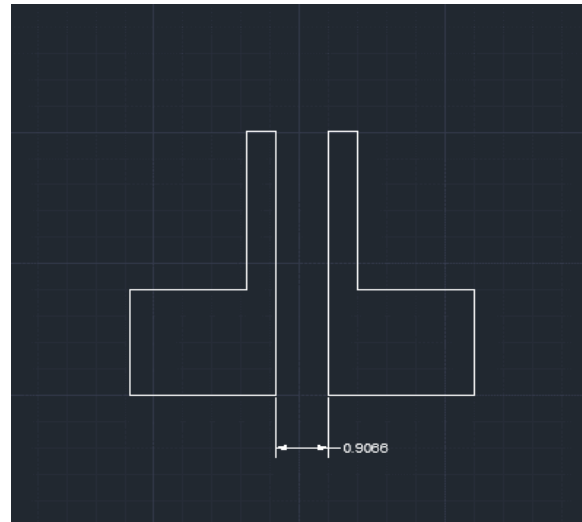


Figure 38. PCA with a large gap size of 0.9066 mm designed in AutoCAD.

The substrate is cleaned using acetone and IPA solution with a temperature of 35 °C for 5 minutes. The microscope image of GaAs substrate after cleaning is shown in Figure 39.

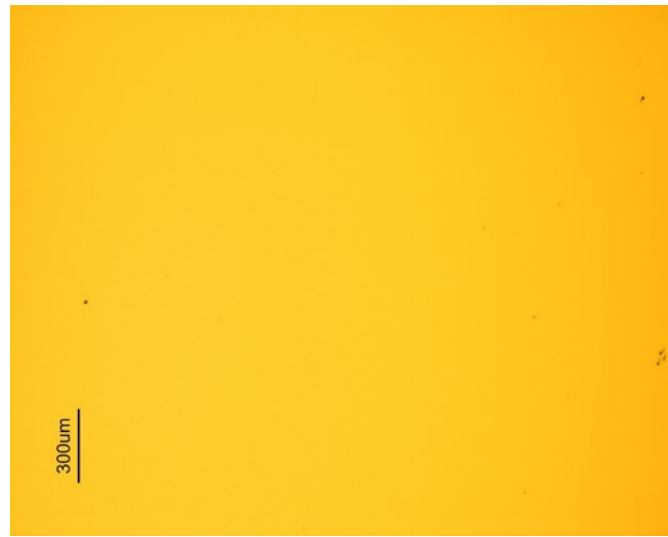


Figure 39. The GaAs substrate after cleaning.

It can be seen from the microscope image that the substrate surface is very clean and flat, which is very important for the following fabrication process. Afterward, the antenna is fabricated by photolithography and e-beam deposition. The electrodes of the GaAs antenna are made using 5 nm Cr and 80 nm Au. The fabricated antenna based on GaAs substrate is shown in Figure 40.

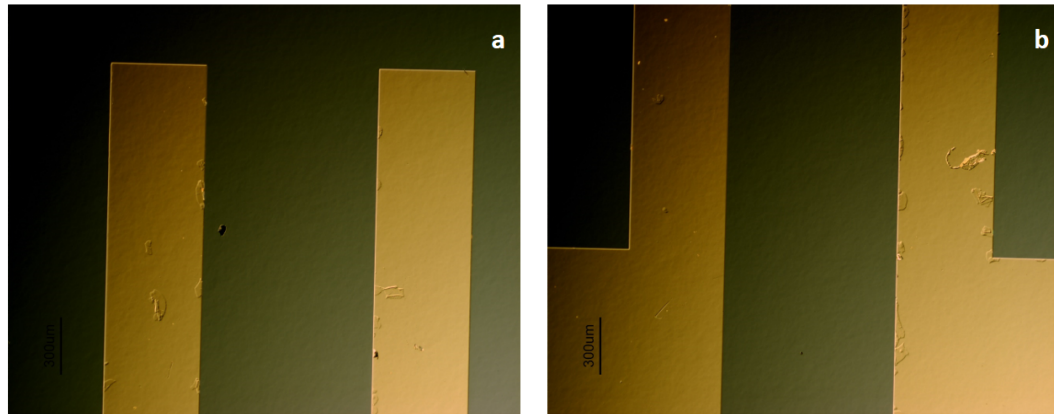


Figure 40. PCA with a large gap size of 0.9066 mm fabricated on GaAs substrate.

The antenna is fixed on the mount using silver paint and soldering, as shown in Figure 41. The dark resistance is measured to be $25\text{ M}\Omega$. We gradually increase the bias voltage applied to the GaAs antenna. At 2.44 kV, air breakdown is observed. Therefore, the air breakdown field of the GaAs PCA is measured to be 23.3 kV/cm.

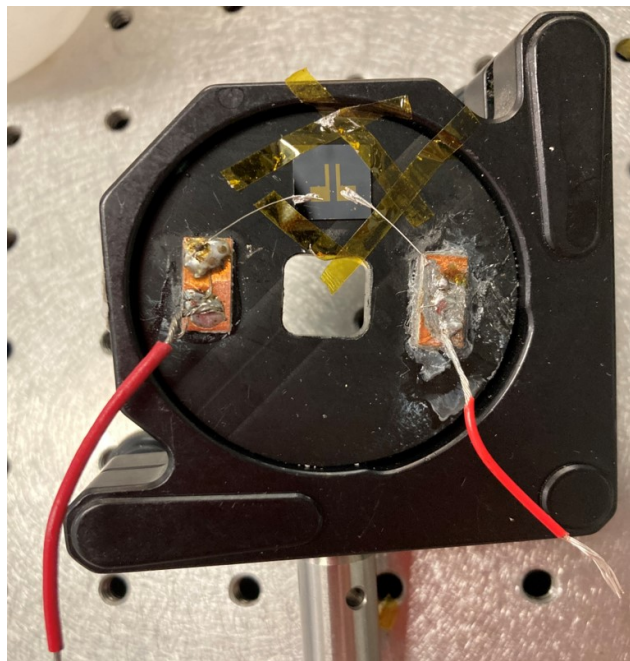


Figure 41. GaAs PCA with a large gap size of 0.9066 mm fixed on the mount for measuring the air breakdown field.

Figure 42 shows the microscope image of PCAs after air breakdown. When air breakdown happens, the air is ionized, and it becomes an electrical conductor, preventing the PCAs from working. Here we don't observe the breakdown of GaAs substrate.

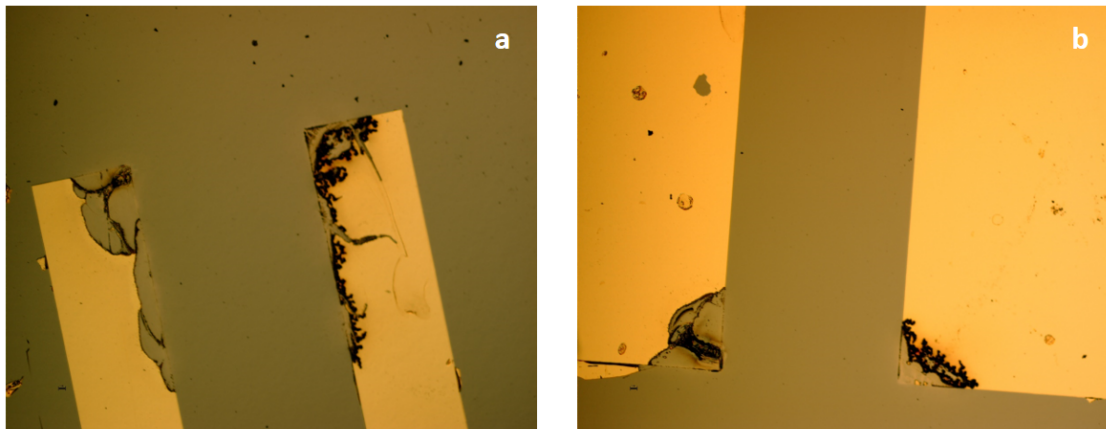


Figure 42. Air breakdown observed in the GaAs PCA when a bias field of 23.3 kV/cm is applied.

The breakdown field of GaAs PCA with an epoxy coating is measured. We first mix the epoxy resin (EFI Polymers 20003) and the epoxy hardener (EFI Polymers 50013) at room temperature. Then we manually add a few drops of the mixed solution on the gap of PCA. We wait 72 hours before testing the PCA, allowing the epoxy to cure. The thickness of the epoxy coating is estimated to be 0.15 mm.

We gradually increase the bias voltage, and the breakdown is observed at a field of 53.3 kV/cm, as shown in Figure 43. The GaAs substrate seems to be damaged, perhaps due to the high temperature induced by the high bias voltage. In this experiment, we successfully demonstrate that by covering the GaAs PCA with an epoxy layer, we can overcome the air breakdown limit and apply higher bias fields to the PCA.

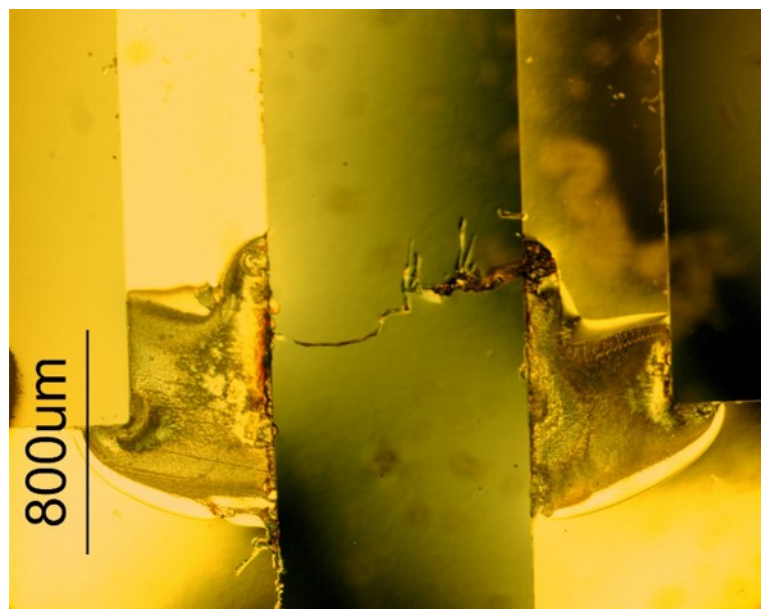


Figure 43. Breakdown observed in the GaAs PCA when a bias field of 53.3 kV/cm is applied.

3.4 THz generated from GaAs-based PCA

The 0.9 mm gap size GaAs PCA is used to generate THz. Figure 44 shows the schematic of the setup. A 1 mm thick (110) CdTe crystal is used as the THz detector. A lithium triborate (LBO) crystal is used for generating the second harmonic of the 1045 nm laser, allowing the laser beam to excite carriers from the valence band to the conduction band in the GaAs substrate. The laser beam with a pump power of 84 mW is focused on the gap of the GaAs PCA, and the probe beam is focused on the CdTe crystal detector.

femtosecond laser
1045 nm <40nJ

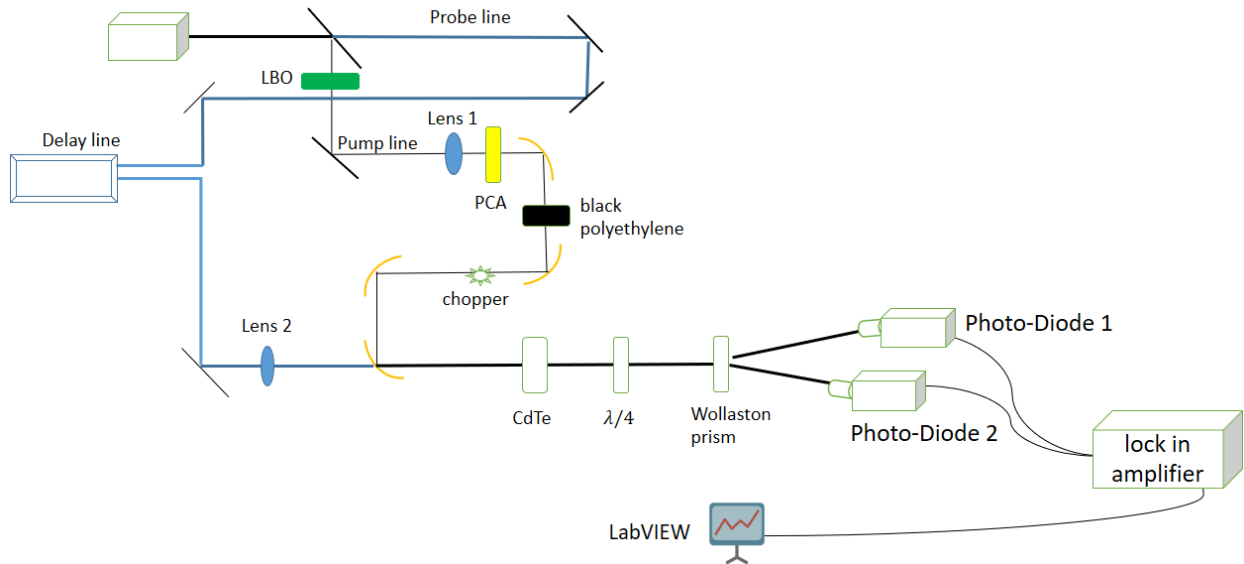


Figure 44. Schematic of the setup using GaAs PCA as THz emitter.

The dark resistance is measured to be $25 \text{ M}\Omega$. When the laser beam is focused on the PCA, the resistance decreases to $130 \text{ k}\Omega$. We increase the bias voltage from 200 V to 550 V, the current on the PCA increases from 1.5 mA to 2.15 mA, and Figure 45 shows the THz waveforms at different bias voltages.

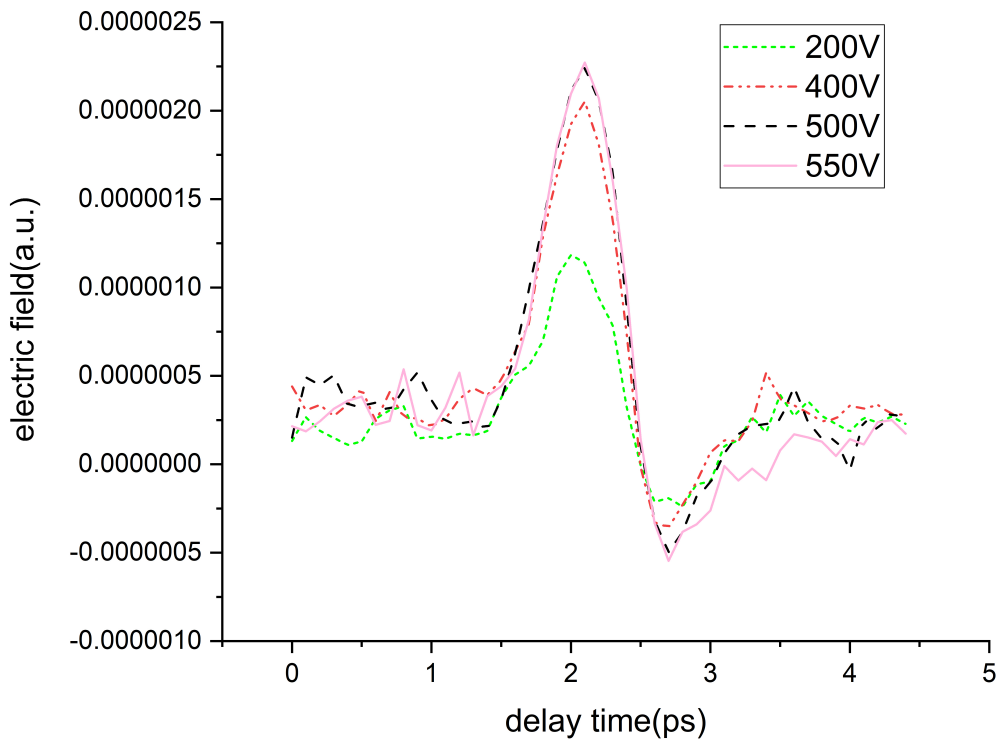


Figure 45. THz waveforms at different bias voltages. The THz peak electric field increases as the bias voltage increases.

The relationship between the THz peak electric field and the applied bias field is shown in Figure 46.

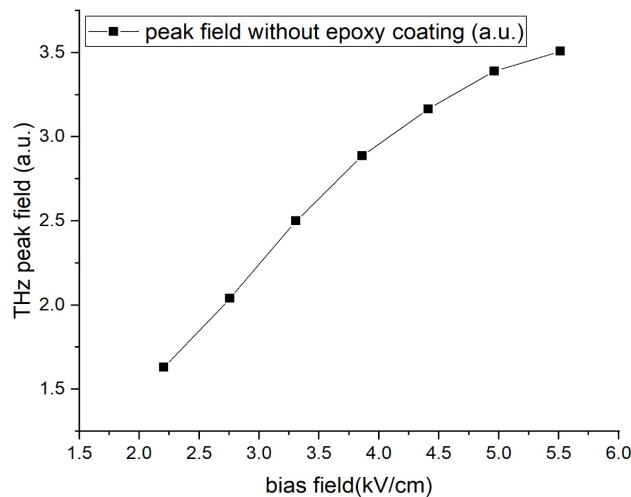


Figure 46. Relationship between the THz peak electric field and the applied bias field. From 2.2 kV/cm to 4.4 kV/cm, the THz peak electric field scales linearly with the bias field.

From 2.2 kV/cm to 4.4 kV/cm, the THz peak electric field scales linearly with the bias field, which is in accordance with equation (16). However, we observe a saturation effect when the bias field is higher than 4.4 kV/cm. In fact, it has been demonstrated that GaAs PCAs often experience significant degradation with time and subsequent failure, primarily due to the increased temperature resulting from Joule heating [15]. As temperature increases, the GaAs fails to work properly, and thus the THz peak electric field is less than what we expect when the bias field is higher than 4.4 kV/cm.

The failure of GaAs PCA with an epoxy coating after applying a bias field of 5.5 kV/cm is observed, as shown in Figure 47. The epoxy coating can prevent PCA from dissipating the heat. Due to the increase in temperature, some electromigration of the gold electrodes occurred, resulting in a total electrical short-cut of the electronic circuit preventing the PCA from working [54].

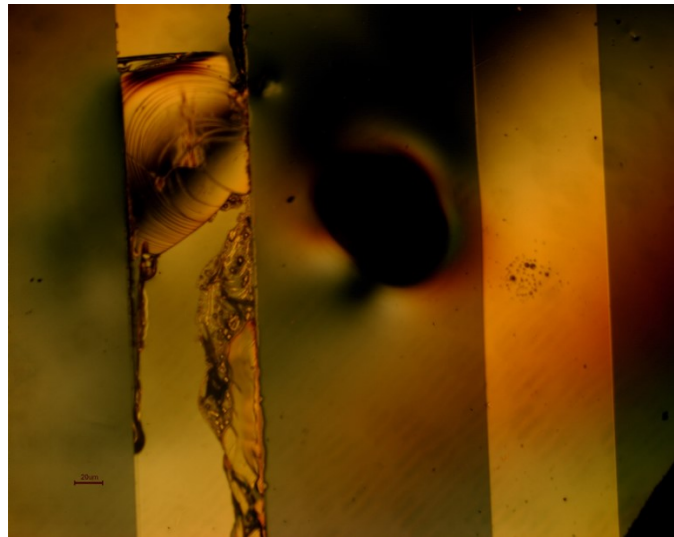


Figure 47. Failure of GaAs PCA after applying a bias field of 5.5 kV/cm, due to the increase in temperature.

It is preferable to choose semiconductor substrates with high thermal conductivity for dissipating the heat. In addition, it is important to realize high-quality Ohmic contacts on the substrate. Another option is to use a substrate with a short carrier lifetime and high dark resistivity to limit the heating of the PCA. The short lifetime reduces the duration of the photocurrent. Dark resistivity is the resistivity of the PCA without laser illumination, and is mainly determined by the bandgap of the semiconductor substrate. The use of wide bandgap

semiconductors with high dark resistivity reduces the heating of PCAs by lower the dark current [54].

The waveforms and amplitude spectrums of THz generated from PCAs with and without the epoxy coating are shown in Figure 48 and Figure 49. It is found that by covering the GaAs PCA with the epoxy resin, the THz peak electric field increases 1.37 times and 1.66 times at 200 V and 400 V bias voltage, respectively. The spectrum of the radiated field showed a bandwidth of 1.5 THz and a peak frequency of 0.2 THz.

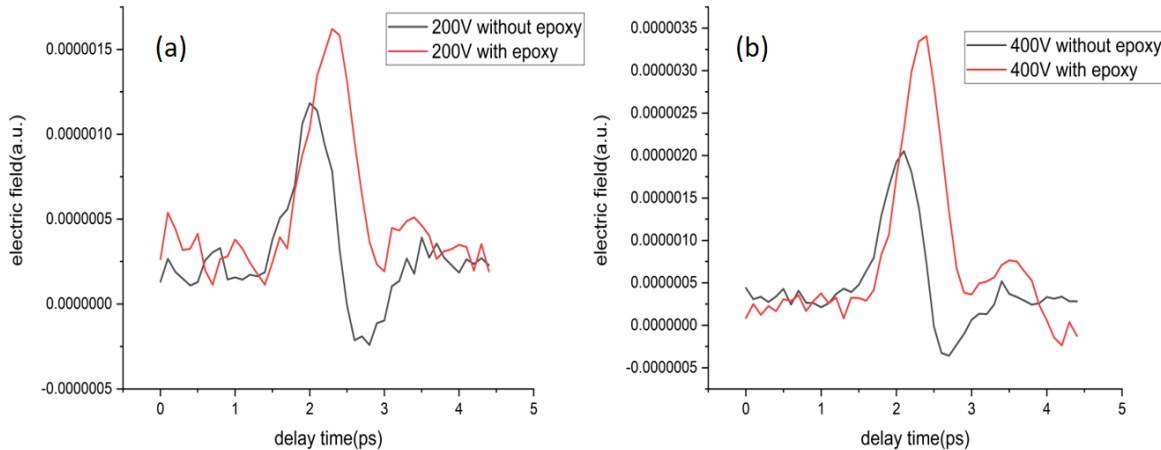


Figure 48. THz waveform (a) at 200 V bias voltage, (b) at 400 V bias voltage, with (red curve) and without the epoxy coating (black curve). By covering the GaAs PCA with the epoxy resin, the THz peak electric field increases.

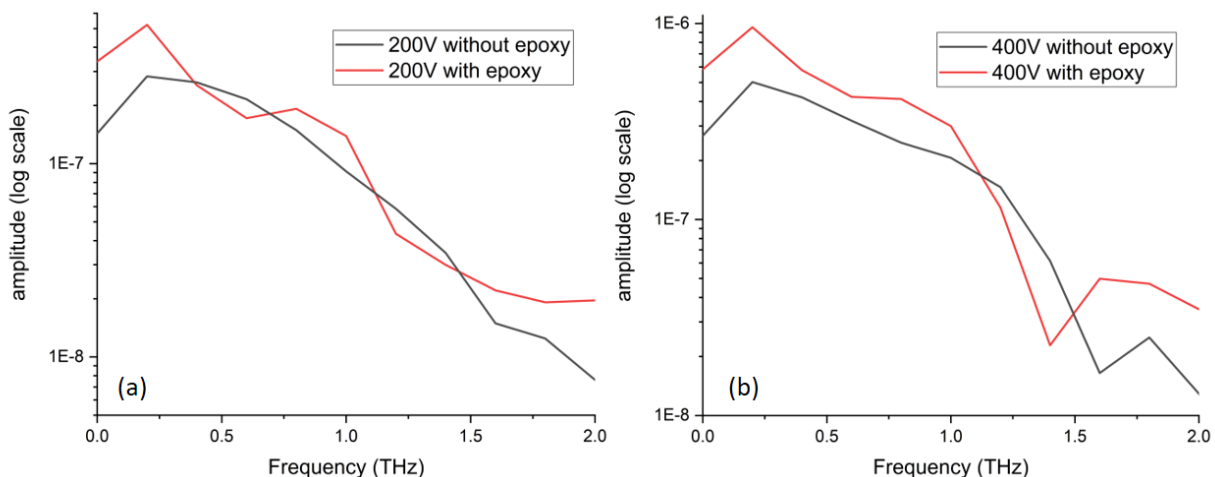


Figure 49. THz amplitude spectrum (a) at 200 V bias voltage, (b) at 400 V bias voltage, with (red curve) and without the epoxy coating (black curve).

To explore this enhancement of THz peak electric field after covering the GaAs PCA with the epoxy resin, we perform simulations calculating the laser intensity irradiating the GaAs surface using FDTD solutions. The schematic is shown in Figure 50. The thickness of epoxy in this simulation is 0.7 μm .

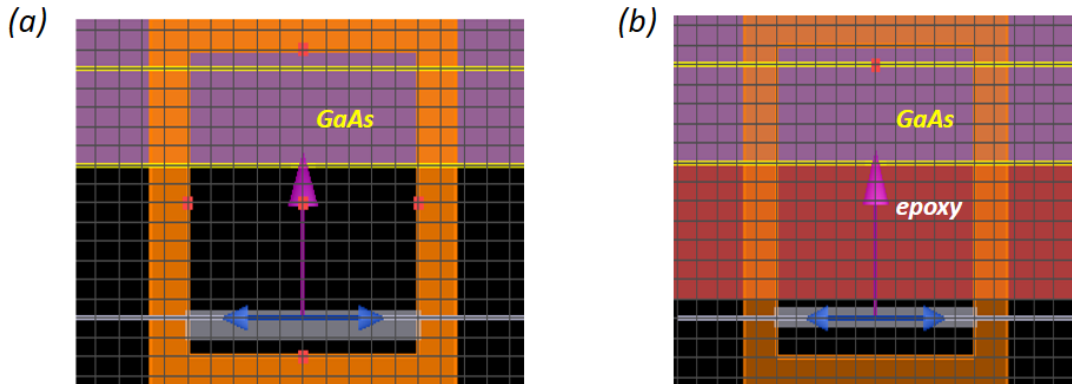


Figure 50. (a) Schematic of the 522 nm femtosecond laser transmitting into bare GaAs substrate. (b) Schematic of the 522 nm femtosecond laser transmitting into GaAs substrate with an 0.7 μm thick epoxy coating.

The 522 nm laser beam is incident on the GaAs surface at $z = 0$. Thus we can obtain the laser intensity irradiating the GaAs surface by calculating the $|E|^2$ at $z = 0$ using FDTD solutions, where E is the transmitted electric field of the 522 nm laser. If there is an enhancement in the laser intensity irradiating the GaAs surface after covering the GaAs substrate with the epoxy, more carriers will be generated in the GaAs substrate. The calculated results of the laser intensity irradiating the GaAs surface without and with the epoxy coating are presented in Figure 51 and Figure 52, respectively.

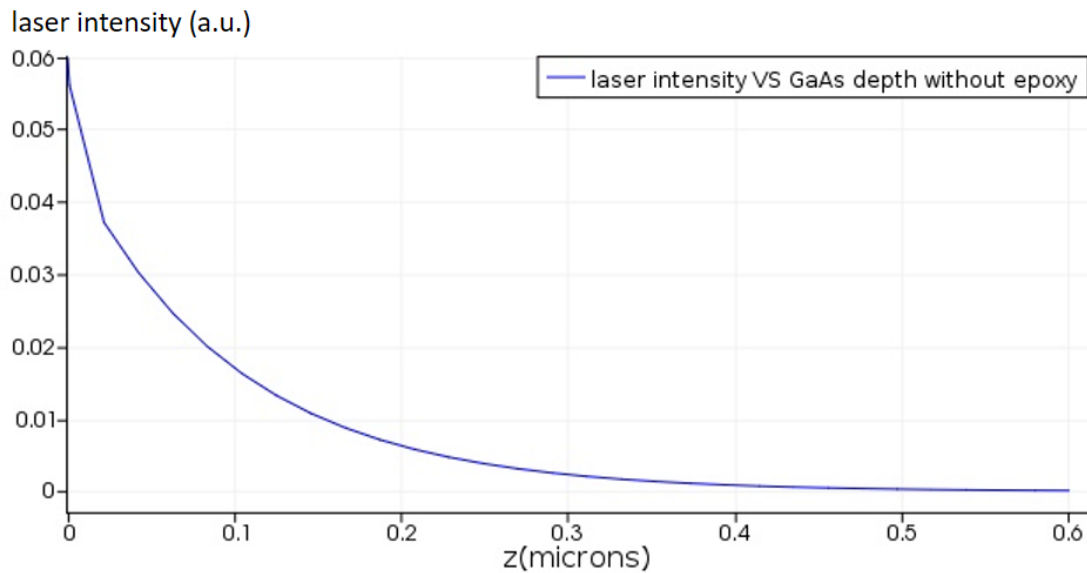


Figure 51. The intensity of the laser after travelling through z microns of GaAs without epoxy layer.

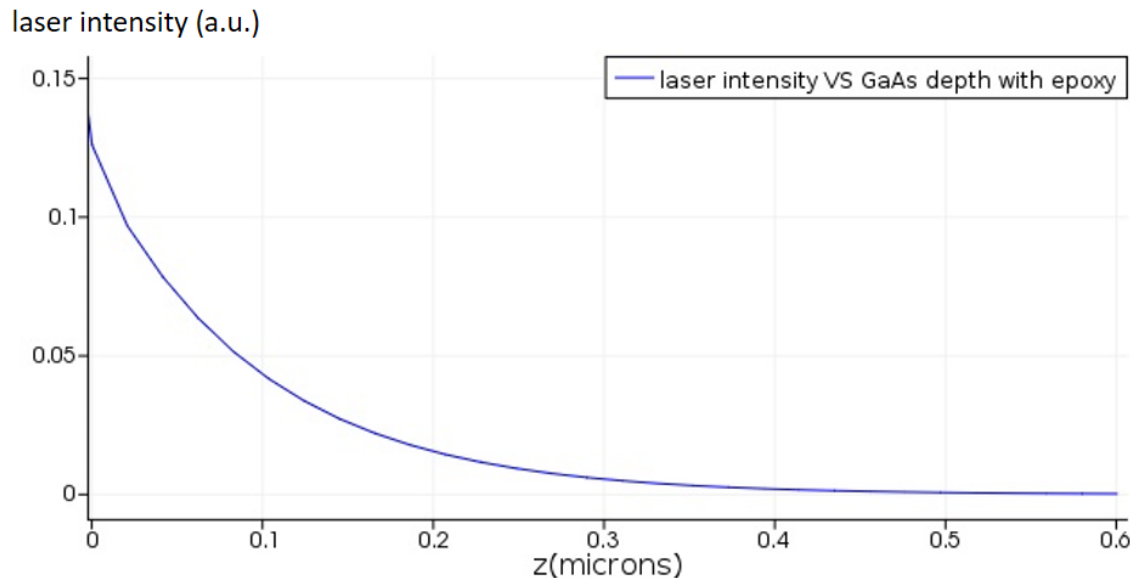


Figure 52. The intensity of the laser after travelling through z microns of GaAs with the epoxy layer.

The 522 nm laser beam is incident on the GaAs surface at $z = 0$. Without the epoxy coating, the laser intensity incident on the GaAs surface is 0.056. While with the epoxy layer, the laser intensity incident on the GaAs surface is 0.126. At a depth of 0.6 microns, the laser intensity

decreases to less than 10^{-6} , which means GaAs almost completely absorbs the 522 nm laser beam. The intensity of the laser after travelling through z microns of GaAs without an epoxy layer can be expressed as:

$$T_1 = 0.056 \times e^{-z/D} \quad (30)$$

Here, D is a constant. The intensity of the laser after travelling through z microns of GaAs with the epoxy layer can be expressed as:

$$T_2 = 0.126 \times e^{-z/D} \quad (31)$$

As we can see, after covering the GaAs PCA with the epoxy layer, the laser intensity irradiating the GaAs surface increases 2.25 (T_2/T_1) times, which means more photons will be absorbed by the GaAs substrate, and thus more carriers should be generated in the GaAs substrate. According to equation (16), the generated THz electric field should increase as the carrier density increases.

As shown in Figure 48 and Figure 49, it is found that by covering the GaAs PCA with the epoxy resin, the THz peak electric field increases 1.37 times and 1.66 times at 200 V and 400 V bias voltage, respectively. It should be pointed out that in this experiment, we cannot control the thickness of the epoxy. The epoxy layer used in the experiments is not a thin film. It has a thickness of approximately 0.15 mm (much larger than 0.7 μm used in the simulations). The mechanism of the transmission enhancement with the epoxy coating may be different. Thus we may not have a 2.25 times enhancement in the laser intensity irradiating the GaAs surface. The structure with a thickness of 0.15 mm requires a tremendous amount of memory, and our computing equipment cannot support that simulation. However, the simulation using 0.7 μm verifies that the laser intensity that irradiates the GaAs surface increases after covering the GaAs PCA with the epoxy layer, which can direct future investigations.

We calculate reflectance with and without the epoxy coating using Fresnel equations for normal incidence. The schematic is shown in Figure 53.

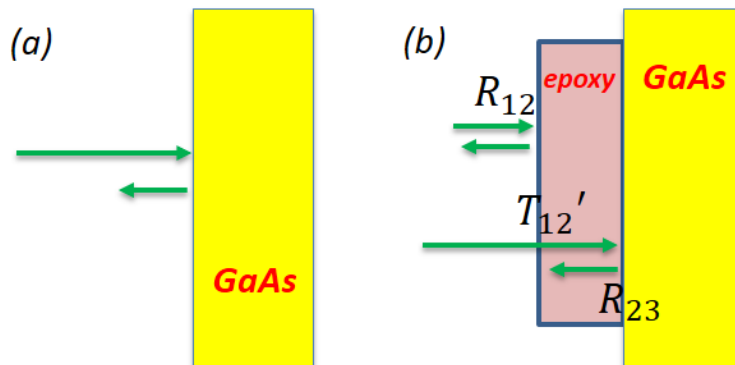


Figure 53. (a) Schematic of the laser beam transmitting into bare GaAs substrate. (b) Schematic of the laser beam transmitting into GaAs substrate with an 0.15 mm thick epoxy coating.

We calculate the reflectance of the air-GaAs interface, as shown in Figure 53 (a). Using Fresnel equations for normal incidence, the reflectance without the epoxy coating is given by:

$$\frac{(n_{GaAs} - n_{air})^2}{(n_{GaAs} + n_{air})^2} = 37.4\% \quad (32)$$

As shown in Figure 53 (b), with the epoxy coating, neglecting the absorption of epoxy resin and considering only one back reflection in the epoxy layer, the reflectance is given by:

$$R_{12} + T'_{12} \times R_{23} = 23.9\% \quad (33)$$

Here, at 522 nm, the refractive index of air $n_{air} = 1$, the refractive index of GaAs $n_{GaAs} = 4.15$ [109], and the refractive index of epoxy $n_{epoxy} = 1.6$ [110]. R_{12} is the reflectance of the air-epoxy interface, and $R_{12} = \frac{(n_{epoxy}-n_{air})^2}{(n_{epoxy}+n_{air})^2} = 0.053$. T'_{12} is the transmittance of the air-epoxy interface, and $T'_{12} = \frac{4n_{air}n_{epoxy}}{(n_{air}+n_{epoxy})^2} = 0.947$. R_{23} is the reflectance of the epoxy-GaAs interface, and $R_{23} = \frac{(n_{GaAs}-n_{epoxy})^2}{(n_{GaAs}+n_{epoxy})^2} = 0.197$.

As we can see, the reflectance decreases 13.5% ($37.4\% - 23.9\%$) with the encapsulation layer. Therefore, the epoxy coating can act as an index-matching material, through which the reflectivity is reduced and the transmission is enhanced, thus more carriers should be generated in the GaAs substrate [78].

Further, the surface of the epoxy coating is not flat. Instead, the coating could form a convex lens, which can focus the laser beam and increase the optical fluence irradiating the GaAs surface.

The fluence of a laser pulse is the optical energy delivered per unit area. The high-energy pulsed laser is not used in this experiment. The optical power of the 522 nm laser is 84 mW, the repetition rate is 64 MHz, and the beam diameter is approximately 1 mm. Therefore, the optical fluence irradiating the GaAs surface is estimated to be 167 nJ/cm^2 , which is much lower than the saturation fluence ($\sim 0.1 \text{ mJ/cm}^2$ for GaAs LAPCAs [52]). Therefore, the signal-to-noise ratio (SNR) is very low, which can lead to experimental errors.

It has been demonstrated that for LAPCAs, the generated THz peak electric field can be expressed as the following equation [15]:

$$E_{THz}^{peak} \propto \beta \frac{F}{F + F_{sat}} \quad (34)$$

Here, β is a constant, F and F_{sat} are the fluence and the saturation fluence, respectively.

When the optical fluence is much lower compared to the saturation fluence, the generated THz peak electric field scales almost linearly with the fluence. The laser beam might be focused

by the epoxy coating, causing an increase in the optical fluence. At 200 V and 400 V bias voltage, the alignment is changed for optimizing the THz signal, thus the degree to which the laser is focused may be different. Therefore, the enhancement of the optical fluence irradiating the GaAs surface may be different at 200 V and 400 V bias voltage, leading to different enhancements of the generated THz electric field.

For example, a 10% reduction in the beam diameter results in a 23.5% increase in the optical fluence. A 20% reduction in the beam diameter results in a 56.3% increase in the optical fluence. As we can see, a slight decrease in the beam diameter can lead to a large increase in the optical fluence, and thus a large increase in the generated THz electric field.

In conclusion, the increased optical fluence irradiating the GaAs surface due to the transmission enhancement and the focusing effect with the epoxy coating partially explains the increased THz output observed in Figure 48 and Figure 49.

Chapter 4

Conclusions and Perspectives

In this thesis, we discussed the generation and detection techniques of THz radiation, studied the THz time-domain spectroscopy (THz-TDS) and investigated new methods to increase the THz intensity. LAPCA can generate intense THz, which makes it possible to study many fascinating nonlinear phenomena.

We introduced a phase retrieval method in THz-TDS measurements and presented the experimental results of the index of refraction and absorption coefficient of CdTe and ZnTe samples. We successfully demonstrated the generation of THz radiation from 0.9 mm gap size GaAs PCAs, which provides the basis for interdigitated LAPCA. It was also demonstrated that we could overcome the air breakdown limit and apply 2.28 times higher bias fields to the PCAs by surface passivation.

An enhancement of the THz electric field after covering the GaAs PCA with an epoxy layer is observed. We demonstrate that with the epoxy coating, the optical fluence irradiating the GaAs surface increases, leading to the increase in the generated THz electric field.

However, failure of GaAs PCA with an epoxy coating after applying a bias field of 5.5 kV/cm is discovered. As we know, GaAs PCAs often experience significant degradation with time and subsequent failure, primarily due to the increased temperature resulting from Joule heating. Therefore, it is preferable to choose semiconductor substrates with high thermal conductivity for dissipating heat.

Further experimental as well as theoretical work is needed to understand the enhancement of the THz electric field after surface passivation. In addition, we can use semiconductors with high thermal conductivity and wide bandgap like 6H-SiC to fabricate LAPCA and apply high bias fields beyond the air breakdown limit by surface passivation to generate intense THz radiation.

Reference

- [1] G. Sharma, L. Razzari, F. H. Su, F. Blanchard, A. Ayesheshim, T. L. Cocker, L. V. Titova, H. C. Bandulet, T. Ozaki, J. C. Kieffer, R. Morandotti, M. Reid, and F. A. Hegmann, "Time-Resolved Terahertz Spectroscopy of Free Carrier Nonlinear Dynamics in Semiconductors," *IEEE Photonics J.* 2, 578 (2010).
- [2] X. Chai, X. Ropagnol, S. M. Raeis-Zadeh, M. Reid, S. Safavi-Naeini, and T. Ozaki, "Subcycle Terahertz Nonlinear Optics," *Phys. Rev. Lett.* 121, 143901 (2018).
- [3] L. Razzari, F. H. Su, G. Sharma, F. Blanchard, A. Ayesheshim, H. C. Bandulet, R. Morandotti, J. C. Kieffer, T. Ozaki, M. Reid, and F. A. Hegmann, "Nonlinear ultrafast modulation of the optical absorption of intense few-cycle terahertz pulses in n-doped semiconductors," *Phys. Rev. B* 79, 193204 (2009).
- [4] J. T. Devreese and R. G. van Welzenis, "Impact Ionisation Probability in InSb," *Appl. Phys. A* 29, 125-132 (1982).
- [5] X. Chai, X. Ropagnol, A. Ovchinnikov, O. Chefonov, A. Ushakov, C. M. Garcia-Rosas, E. Isgandarov, M. Agranat, T. Ozaki, and A. Savel'ev, "Observation of crossover from intraband to interband nonlinear terahertz optics," *Optics Letters* Vol. 43, Issue 21, pp. 5463-5466 (2018).
- [6] P. Lugli, P. Bordone, L. Reggiani, M. Rieger, P. Kocevar, and S. M. Goodnick, "Monte Carlo studies of nonequilibrium phonon effects in polar semiconductors and quantum wells. I. Laser photoexcitation," *Phys. Rev. B* 39, 7852 (1989).
- [7] J. E. Bjarnason, T. L. J. Chan, A. W. M. Lee, M. A. Celis, and E. R. Brown, "Millimeter-wave, terahertz, and mid-infrared transmission through common clothing," *Appl. Phys. Lett.* 85, 519 (2004).
- [8] K. Ahi and M. Anwar, "A survey on GaN-based devices for terahertz photonics," *Proc. SPIE*, vol. 9957, pp. 99570A-1–99570A-13, 2016.
- [9] Kiarash Ahi, "Mathematical Modeling of THz Point Spread Function and Simulation of THz Imaging Systems," *IEEE Transactions on Terahertz Science and Technology*, vol. 7, no. 6, pp. 747-754, Nov. 2017.
- [10] Anastasiia Tukmakova, Ivan Tkhorzhevskiy, Artyom Sedinin, Aleksei Asach, Anna Novotelnova, Natallya Kablukova, Petr Demchenko, Anton Zaitsev, Dmitry Zykov and Mikhail Khodzitsky, "FEM Simulation of Frequency-Selective Surface Based on Thermoelectric Bi-Sb Thin Films for THz Detection," *Photonics* 2021, 8, 119.
- [11] D. You, R. R. Jones, P. H. Bucksbaum, and D. R. Dykaar, "Generation of high-power sub-single-cycle 500-fs electromagnetic pulses," *Optics Letters* Vol. 18, Issue 4, pp. 290-292 (1993).
- [12] F. Blanchard, L. Razzari, H.-C. Bandulet, G. Sharma, R. Morandotti, J.-C. Kieffer, T. Ozaki, M. Reid, H. F. Tiedje, H. K. Haugen, and F. A. Hegmann, "Generation of 1.5 μ J single-cycle terahertz pulses by optical rectification from a large aperture ZnTe crystal," *Optics Express* Vol. 15, Issue 20, pp. 13212-13220 (2007).

- [13] X. Ropagnol, F. Blanchard, T. Ozaki, and M. Reid, "Intense terahertz generation at low frequencies using an interdigitated ZnSe large aperture photoconductive antenna," *Appl. Phys. Lett.* 103, 161108 (2013).
- [14] X. Ropagnol, M. Khorasaninejad, M. Raeiszadeh, S. Safavi-Naeini, M. Bouvier, C. Y. Côté, A. Laramée, M. Reid, M. A. Gauthier, and T. Ozaki, "Intense THz Pulses with large ponderomotive potential generated from large aperture photoconductive antennas," *Opt. Express* 24, 11299 (2016).
- [15] X. Ropagnol, Marcel Bouvier, M. Reid, and T. Ozaki, "Improvement in thermal barriers to intense terahertz generation from photoconductive antennas," *Journal of Applied Physics* 116, 043107 (2014).
- [16] X Ropagnol, Zs Kovács, B Gilicze, M Zhuldybina, F Blanchard, C M Garcia-Rosas, S Szatmári, I B Földes and T Ozaki, "Intense sub-terahertz radiation from wide-bandgap semiconductor based large-aperture photoconductive antennas pumped by UV lasers," *New J. Phys.* 21 (2019) 113042.
- [17] Hang Zhao, Yong Tan, Tong Wu, Gunther Steinfeld, Yan Zhang, Cunlin Zhang, Liangliang Zhang, and Mostafa Shalaby, "Efficient broadband terahertz generation from organic crystal BNA using near infrared pump," *Appl. Phys. Lett.* 114, 241101 (2019).
- [18] Mostafa Shalaby and Christoph P. Hauri, "Demonstration of a low-frequency three-dimensional terahertz bullet with extreme brightness," *Nat Commun* 6, 5976 (2015).
- [19] F. Blanchard, G. Sharma, X. Ropagnol, L. Razzari, R. Morandotti, and T. Ozaki, "Improved terahertz two-color plasma sources pumped by high intensity laser beam," *Opt. Express* 17, 6044 (2009).
- [20] F. Blanchard, G. Sharma, L. Razzari, X. Ropagnol, H.-C. Bandulet, F. Vidal, R. Morandotti, J.-C. Kieffer, T. Ozaki, H. Tiedje, H. Haugen, M. Reid, and F. Hegmann, "Generation of Intense Terahertz Radiation via Optical Methods," *IEEE J. Select. Topics Quantum Electron.* 17, 5 (2011).
- [21] X. Ropagnol, R. Morandotti, T. Ozaki, and M. Reid, "THz pulse shaping and improved optical-to-THz conversion efficiency using a binary phase mask," *Opt. Lett.* 36, 2662 (2011).
- [22] F. Blanchard, X. Ropagnol, H. Hafez, H. Razavipour, M. Bolduc, R. Morandotti, T. Ozaki, and D. G. Cooke, "Effect of extreme pump pulse reshaping on intense terahertz emission in lithium niobate at multimilliJoule pump energies," *Opt. Lett.* 39, 4333 (2014).
- [23] S. Mondal, H. A. Hafez, X. Ropagnol, and T. Ozaki, "MV/cm terahertz pulses from relativistic laser-plasma interaction characterized by nonlinear terahertz absorption bleaching in n-doped InGaAs," *Opt. Express* 25, 17511 (2017).
- [24] Bernd M. Fischer, Matthias Hoffmann, Hanspeter Helm, Rafal Wilk, Frank Rutz, Thomas Kleine-Ostmann, Martin Koch, and Peter Uhd Jepsen, "Terahertz time-domain spectroscopy and imaging of artificial RNA," *Optics Express* Vol. 13, Issue 14, pp. 5205-5215 (2005).
- [25] Jianming Dai, Jiangquan Zhang, Weili Zhang, and D. Grischkowsky, "Terahertz time-domain spectroscopy characterization of the far-infrared absorption and index of refraction of high-resistivity, float-zone silicon," *J. Opt. Soc. Am. B/Vol.* 21, No. 7/July 2004.
- [26] M. Naftalya and R. E. Miles, "Terahertz time-domain spectroscopy of silicate glasses and the relationship to material properties," *J. Appl. Phys.* 102, 043517 (2007).

- [27] S. Karthick, D. Ganesh, K. Thirupugalmani, A.K. Chaudhary, S. Brahadeeswaran, "Terahertz generation and optical properties of N-benzyl-2-methyl-4-nitroaniline single crystals in 0.1–2.0 THz range for photonic applications," *Materials Letters* 246 (2019) 95–98.
- [28] Isaac C. Tangen, Gabriel A. Valdivia-Berroeta, Larry K. Heki, Zachary B. Zaccardi, Erika W. Jackson, Charles B. Bahr, David J. Michaelis, and Jeremy A. Johnson, "Comprehensive Characterization of Terahertz Generation with the Organic Crystal BNA," *Journal of the Optical Society of America B* Vol. 38, Issue 9, pp. 2780–2785 (2021).
- [29] M. Bass, P. A. Franken, J. F. Ward, and G. Weinreich, "Optical Rectification," *Physical Review Letters*, Vol. 9, p. 446, 1962.
- [30] T. J. Carrig, G. Rodriguez, T. S. Clement, A. J. Taylor, and K. R. Stewart, "Scaling of terahertz radiation via optical rectification in electro-optic crystals," *Applied Physics Letters*, Vol. 66, p. 121, 1995.
- [31] Q. Chen and X. C. Zhang, "Polarization modulation in optoelectronic generation and detection of terahertz beams," *Applied Physics Letters*, Vol. 74, p. 3435, 1999.
- [32] P. Y. Han and X. C. Zhang, "Coherent, broadband midinfrared terahertz beam sensors," *Applied Physics Letters*, Vol. 73, p. 3049, 1998.
- [33] A. Nahata, A. S. Weling, and T. F. Heinz, "A wideband coherent terahertz spectroscopy system using optical rectification and electro-optic sampling," *Applied Physics Letters*, Vol. 69, p. 2321, 1996.
- [34] X. C. Zhang, Y. Jin, and X. F. Ma, "Coherent measurement of THz optical rectification from electro-optic crystals," *Applied Physics Letters*, Vol. 61, p. 2764, 1992.
- [35] L. Xu, X. C. Zhang, and D. H. Auston, "Terahertz beam generation by femtosecond optical pulses in electro-optic materials," *Applied Physics Letters*, Vol. 61, p. 1784, 1992.
- [36] Y.-S. Lee, *Principles of Terahertz Science and Technology*. New York: Springer, 2008.
- [37] X. Ropagnol, M. Matoba, J. E. Nkeck, F. Blanchard, E. Isgandarov, J. Yumoto, and T. Ozaki, "Efficient terahertz generation and detection in cadmium telluride using ultrafast ytterbium laser," *Appl. Phys. Lett.* 117, 181101 (2020).
- [38] Klaus Reimann, "Table-top sources of ultrashort THz pulses," *Rep. Prog. Phys.* 70 (2007) 1597–1632.
- [39] A. Rice, Y. Jin, X. F. Ma, X. C. Zhang, D. Bliss, J. Larkin, *et al.*, "Terahertz optical rectification from zinc-blende crystals," *Applied Physics Letters*, Vol. 64, p. 1324, 1994.
- [40] B. B. Hu, X. C. Zhang, D. H. Auston, and P. R. Smith, "Free-space radiation from electro-optic crystals," *Applied Physics Letters*, Vol. 56, p. 506, 1990.
- [41] A. Nahata, D. H. Auston, T. F. Heinz, and C. Wu, "Coherent detection of freely propagating terahertz radiation by electro-optic sampling," *Applied Physics Letters*, Vol. 68, p. 150, 1996.
- [42] M. Nagai, K. Tanaka, H. Ohtake, T. Bessho, T. Sugiura, T. Hirosumi, *et al.*, "Generation and detection of terahertz radiation by electro-optical process in GaAs using 1.56 μm fiber laser pulses," *Applied Physics Letters*, Vol. 85, p. 3974, 2004.

- [43] A. Syouji, S. Saito, K. Sakai, M. Nagai, K. Tanaka, H. Ohtake, *et al.*, "Evaluation of a terahertz wave spectrum and construction of a terahertz wave-sensing system using a Yb-doped fiber laser," *Journal of the Optical Society of America B-Optical Physics*, Vol. 24, p. 2006, 2007.
- [44] Q. Wu and X.-C. Zhang, "Ultrafast electro-optic field sensors," *Appl. Phys. Lett.* 68, 1604 (1996).
- [45] János Hebling, Ka-Lo Yeh, Matthias C. Hoffmann, Balázs Bartal, and Keith A. Nelson, "Generation of high-power terahertz pulses by tilted-pulse-front excitation and their application possibilities," *Journal of the Optical Society of America B* Vol. 25, Issue 7, pp. B6-B19 (2008).
- [46] Mojca Jazbinsek, Uros Puc, Andreja Abina, and Aleksander Zidansek, "Organic Crystals for THz Photonics," *Appl. Sci.* 2019, 9, 882.
- [47] Jia Xu, Björn Globisch, Christina Hofer, Nikolai Lilienfein, Thomas Butler, Nicholas Karpowicz, and Joachim Pupeza, "Three-octave terahertz pulses from optical rectification of 20 fs, 1μm, 78MHz pulses in GaP," *J. Phys. B: At. Mol. Opt. Phys.* 51 (2018) 154002.
- [48] Katsuyoshi Aoki, Janne Savolainen, and Martina Havenith, "Broadband terahertz pulse generation by optical rectification in GaP crystals," *Appl. Phys. Lett.* 110, 201103 (2017).
- [49] C. Vicario, A. V. Ovchinnikov, S. I. Ashitkov, M. B. Agranat, V. E. Fortov, and C. P. Hauri, "Generation of 0.9-mJ THz pulses in DSTMS pumped by a Cr:Mg₂SiO₄ laser," *Optics Letters* Vol. 39, Issue 23, pp. 6632-6635 (2014).
- [50] P. Y. Han, M. Tani, F. Pan, and X.-C. Zhang, "Use of the organic crystal DAST for terahertz beam applications," *Optics Letters* Vol. 25, Issue 9, pp. 675-677 (2000).
- [51] John J. Carey, Ray T. Bailey, D. Pugh, J. N. Sherwood, and F. R. Cruickshank, and Klaas Wynne, "Terahertz pulse generation in an organic crystal by optical rectification and resonant excitation of molecular charge transfer," *Appl. Phys. Lett.* 81, 4335 (2002).
- [52] Darrow J T, Zhang X-C, Auston D H and Morse J D, "Saturation properties of large-aperture photoconducting antennas," *IEEE J. Quantum Electron.* 28 1607–16 (1992)
- [53] H A Hafez, X Chai, A Ibrahim, S Mondal, D Féralchou, X Ropagnol and T Ozaki, "Intense terahertz radiation and their applications," *J. Opt.* 18 093004 (2016)
- [54] Elchin Isgandarov, Xavier Ropagnol, Mangaljit Singh and Tsuneyuki Ozaki, "Intense terahertz generation from photoconductive antennas," *Front. Optoelectron* 14, 64–93 (2021).
- [55] Peter Uhd Jepsen, David G. Cooke, and Martin Koch, "Terahertz spectroscopy and imaging – Modern techniques and applications," *Laser Photonics Rev.* 5, No. 1, 124–166 (2011)
- [56] Duvillaret L, Garet F, Roux J F, Coutaz J L, "Analytical modeling and optimization of terahertz time-domain spectroscopy experiments using photoswitches as antennas," *IEEE Journal of Selected Topics in Quantum Electronics*, 2001, 7(4): 615–623
- [57] Paschen, F. (1889), "Ueber die zum Funkenübergang in Luft, Wasserstoff und Kohlensäure bei verschiedenen Drucken erforderliche Potentialdifferenz," *Annalen der Physik*. 273 (5): 69–96.

- [58] Lieberman, Michael A.; Lichtenberg, Allan J. (2005). Principles of plasma discharges and materials processing (2nd ed.). Hoboken, N.J.: Wiley-Interscience. 546.
- [59] Dennis Fisher; I. J. Bahl (1995). Gallium Arsenide IC Applications Handbook. Vol. 1. Elsevier. p. 61.
- [60] Ye P., Xuan Y., Wu Y., Xu M., "Atomic-Layer Deposited High-k/III-V Metal-Oxide-Semiconductor Devices and Correlated Empirical Model," In: Oktyabrsky S., Ye P. (eds) Fundamentals of III-V Semiconductor MOSFETs. Springer, Boston, MA, (2010).
- [61] Qing-li Zhou, Yulei Shi, Bin Jin, and Cunlin Zhang, "Ultrafast carrier dynamics and terahertz conductivity of photoexcited GaAs under electric field," *Appl. Phys. Lett.* 93, 102103 (2008).
- [62] Justin T. Darrow, Xi-Cheng Zhang, David H. Auston, Fellow, ZEEE, and Jeffrey D. Morse, "Saturation Properties of Large-Aperture Photoconducting Antennas," *IEEE Journal of Quantum Electronics*, vol. 28, no. 6, pp. 1607-1616, June 1992.
- [63] J. D. Jackson, Classical Electrodynamics, 2nd ed. New York: Wiley, 1975, pp. 339.
- [64] Andreas Gurtler, Carsten Winnewisser, Hanspeter Helm, and Peter Uhd Jepsen, "Terahertz pulse propagation in the near field and the far field," *J. Opt. Soc. Am. A/Vol. 17, No. 1/January 2000*.
- [65] X C Zhang, Introduction to THz Wave Photonics (New York Springer 29, 2010).
- [66] Reid M, Fedosejevs R, "Quantitative comparison of terahertz emission from (100) InAs surfaces and a GaAs large-aperture photoconductive switch at high fluences," *Applied Optics*, 2005, 44(1): 149–153
- [67] Li-Mo Wang, "Relationship between Intrinsic Breakdown Field and Bandgap of Materials," 2006 25th International Conference on Microelectronics, 2006.
- [68] P. Perlin, I. Gorczyca, T. Suski, P. Wisniewski, S. Lepkowski, N. E. Christensen, A. Svane, M. Hansen, S. P. DenBaars, B. Damilano, N. Grandjean, and J. Massies, "Influence of pressure on the optical properties of $\text{In}_x\text{Ga}_{1-x}\text{N}$ epilayers and quantum structures," *Phys. Rev. B* 64, 115319 – Published 31 August 2001.
- [69] Ričardas Norkus, Ramūnas Aleksiejūnas, Arūnas Kadys, Marek Kolenda, Gintautas Tamulaitis, and Arūnas Krotkus, "Spectral dependence of THz emission from InN and InGaN layers," *Scientific Reports* | (2019) 9:7077
- [70] Wang, Xiaoyi (2018) Characterization of InGaN Thin Films and Nanowires by Analytical Transmission Electron Microscopy. PhD thesis, University of Sheffield.
- [71] S. Nacer, A. Aissat, "Simulation and optimization of current matching double-junction InGaN/Si solar cells," *Appl. Phys. A* (2016) 122:138.
- [72] P. Sohi, J.-F. Carlin, and N. Grandjean, "Alloy disorder limited mobility of InGaN twodimensional electron gas," *Appl. Phys. Lett.* 112, 262101 (2018).
- [73] J. Xie, J. H. Leach, X. Ni, M. Wu, R. Shimada, Ü. Özgür, and H. Morkoç, "Electron mobility in InGaN channel heterostructure field effect transistor structures with different barriers," *Appl. Phys. Lett.* 91, 262102 (2007).

- [74] R. Wang, G. Li, G. Karbasian, J. Guo, F. Faria, Z. Hu, Y. Yue, J. Verma, O. Laboutin, Y. Cao, W. Johnson, G. Snider, P. Fay, D. Jena, and H. Xing, "InGaN Channel High-Electron-Mobility Transistors with InAlGaN Barrier and fT/fmax of 260/220 GHz," *Appl. Phys. Express* 6, 016503 (2013).
- [75] N. Pala, S. Rumyantsev, M. Shur, R. Gaska, X. Hu, J. Yang, G. Simin, and M. A. Khan, "Low frequency noise in AlGaN/InGaN/GaN double heterostructure field effect transistors," *Solid-State Electron.* 47, 1099 (2003).
- [76] J. Liberis, I. Matulioniene, A. Matulionis, E. Sermuksnis, J. Xie, J. H. Leach, and H. Morkoc, "InAlN-barrier HFETs with GaN and InGaN channels," *Phys. Status Solidi A* 206, 1385 (2009).
- [77] Abhishek Gupta, Goutam Rana, Arkabrata Bhattacharya, Abhishek Singh, Ravikumar Jain, Rudheer D. Bapat, S. P. Duttagupta, and S. S. Prabhu, "Enhanced optical-to-THz conversion efficiency of photoconductive antenna using dielectric nano-layer encapsulation," *APL Photonics* 3, 051706 (2018).
- [78] C. Headley *et al.*, "Improved Performance of GaAs-Based Terahertz Emitters via Surface Passivation and Silicon Nitride Encapsulation," in *IEEE Journal of Selected Topics in Quantum Electronics*, vol. 17, no. 1, pp. 17-21, Jan.-Feb. 2011.
- [79] Mohammad Bashirpour, Matin Forouzmehr, Seyed Ehsan Hosseininejad, Mohammadreza Kolahdouz, and Mohammad Neshat, "Improvement of Terahertz Photoconductive Antenna using Optical Antenna Array of ZnO Nanorods," *Sci Rep* 9, 1414 (2019).
- [80] Yutaka Ohno, Takeshi Nakao, Shigeru Kishimoto, Koichi Maezawa, and Takashi Mizutani, "Effects of surface passivation on breakdown of AlGaN/GaN high-electron-mobility transistors," *Appl. Phys. Lett.* 84, 2184 (2004).
- [81] C-L. Chen, L. J. Mahoney, M. J. Manfra, F. W. Smith, D. H. Temme and A. R. Calawa, "High-breakdown-voltage MESFET with a low-temperature-grown GaAs passivation layer and overlapping gate structure," in *IEEE Electron Device Letters*, vol. 13, no. 6, pp. 335-337, June 1992.
- [82] Dmitry Levko, Robert R. Arslanbekov, and Vladimir I. Kolobov, "Modified Paschen curves for pulsed breakdown," *Physics of Plasmas* 26, 064502 (2019).
- [83] D. H. Auston, A. M. Johnson, P. R. Smith, and J. C. Bean, "Picosecond optoelectronic detection, sampling, and correlation measurements in amorphous semiconductors," *Appl. Phys. Lett.* 37, 371 (1980).
- [84] P. Uhd Jepsen, R. H. Jacobsen, and S. R. Keiding, "Generation and detection of terahertz pulses from biased semiconductor antennas," *Journal of the Optical Society of America B* Vol. 13, Issue 11, pp. 2424-2436 (1996).
- [85] Q. Wu and X.-C. Zhang, "Free-space electro-optic sampling of terahertz beams," *Appl. Phys. Lett.* 67, 3523 (1995).
- [86] G. Gallot and D. Grischkowsky, "Electro-optic detection of terahertz radiation," *Journal of the Optical Society of America B* Vol. 16, Issue 8, pp. 1204-1212 (1999).
- [87] J. A. Valdmanis, G. Mourou, and C. W. Gabel, "Picosecond electro-optic sampling system," *Appl. Phys. Lett.* 41, 211 (1982).

- [88] Ajay Nahata, Aniruddha S. Weling, and Tony F. Heinz, "A wideband coherent terahertz spectroscopy system using optical rectification and electro-optic sampling," *Appl. Phys. Lett.* 69, 2321 (1996).
- [89] Shunsuke Kono, Masahiko Tani, and Kiyomi Sakai, "Ultrabroadband photoconductive detection: Comparison with free-space electro-optic sampling," *Appl. Phys. Lett.* 79, 898 (2001).
- [90] Ajay Nahata, David H. Auston, and Tony F. Heinz, "Coherent detection of freely propagating terahertz radiation by electro-optic sampling," *Appl. Phys. Lett.* 68, 150 (1996).
- [91] Peter Uhd Jepsen, "Phase Retrieval in Terahertz Time-Domain Measurements: a 'how to' Tutorial," *Journal of Infrared, Millimeter, and Terahertz Waves* 40, 395–411 (2019).
- [92] M. van Exter, C. Fattinger, and D. Grischkowsky, "Terahertz time-domain spectroscopy of water vapor," *Opt. Lett.* 14, 1128–1130 (1989).
- [93] W. Withayachumnankul, and M. Naftaly, "Fundamentals of Measurement in Terahertz Time-Domain Spectroscopy," *J. Infrared Millim. Terahertz Waves* 35, 610–637 (2014).
- [94] L. Duvillaret, F. Garet, and J. L. Coutaz, "A reliable method for extraction of material parameters in terahertz time-domain spectroscopy," *IEEE J. Sel. Top. Quantum Electron.* 2, 739–746 (1996).
- [95] L. Duvillaret, F. Garet, and J. L. Coutaz, "Highly precise determination of optical constants and sample thickness in terahertz time-domain spectroscopy," *Appl. Opt.* 38, 409–415 (1999).
- [96] I. Pupeza, R. Wilk, and M. Koch, "Highly accurate optical material parameter determination with THz timedomain spectroscopy," *Opt. Express* 15, 4335–4350 (2007).
- [97] M. Scheller, C. Jansen, and M. Koch, "Analyzing sub-100- μm samples with transmission terahertz time domain spectroscopy," *Opt. Comm.* 282, 1304–1306 (2009).
- [98] M. Kruger, S. Funkner, E. Brundermann, and M. Havenith, "Uncertainty and Ambiguity in Terahertz Parameter Extraction and Data Analysis," *J. Infrared Millim. Terahertz Waves* 32, 699–715 (2011).
- [99] M. Naftaly, and R. Dudley, "Methodologies for determining the dynamic ranges and signal-to-noise ratios of terahertz time-domain spectrometers," *Opt. Lett.* 34, 1213–1215 (2009).
- [100] P. U. Jepsen, and B. M. Fischer, "Dynamic range in terahertz time-domain transmission and reflection spectroscopy," *Opt. Lett.* 30, 29–31 (2005).
- [101] Brian G. Alberding, W. Robert Thurber, and Edwin J. Heilweil, "Direct comparison of time-resolved terahertz spectroscopy and Hall Van der Pauw methods for measurement of carrier conductivity and mobility in bulk semiconductors," *Journal of the Optical Society of America B* Vol. 34, Issue 7, pp. 1392–1406 (2017).
- [102] B. J. Baliga, "Semiconductors for high-voltage, vertical channel field-effect transistors," *Journal of Applied Physics* 53, 1759 (1982).
- [103] Max N. Yoder, "Wide Bandgap Semiconductor Materials and Devices," *IEEE Transactions on Electron Devices*, vol. 43, no. 10, pp. 1633–1636, Oct. 1996.

- [104] D. Xiao, "Dielectric strength of atmosphere air," *Gas Discharge and Gas Insulation* pp 149-194 (2016).
- [105] M. Schall, H. Helm, and S. R. Keiding, "Far Infrared Properties of Electro-Optic Crystals Measured by THz Time-Domain Spectroscopy," *International Journal of Infrared and Millimeter Waves* volume 20, 595–604 (1999).
- [106] F. Blanchard, D. Golde, F. H. Su, L. Razzari, G. Sharma, R. Morandotti, T. Ozaki, M. Reid, M. Kira, S. W. Koch, and F. A. Hegmann, "Effective Mass Anisotropy of Hot Electrons in Nonparabolic Conduction Bands of n-Doped InGaAs Films Using Ultrafast Terahertz Pump-Probe Techniques," *Phys. Rev. Lett.* 107, 107401 (2011).
- [107] Laboratory of Terahertz Spectroscopy, Prague. <https://lts.fzu.cz/en/intro.php>. (2012). [Online; Accessed: 08/01/2021].
- [108] M. Schall, M. Walther, and P. Uhd Jepsen, "Fundamental and second-order phonon processes in CdTe and ZnTe," *Phys. Rev. B* 64, 094301.
- [109] RefractiveIndex.INFO Refractive index database.
<https://refractiveindex.info/?shelf=main&book=GaAs&page=Aspnes>. [Online; Accessed: 05/03/2022].
- [110] Peter R. Cooper, "Refractive-index measurements of paraffin, a silicone elastomer, and an epoxy resin over the 500–1500-nm spectral range," *Applied Optics* Vol. 21, Issue 19, pp. 3413-3415 (1982).

Sommaire Récapitulatif-Amélioration de la limite de claquage de l'air dans les antennes photoconductrices par passivation de surface pour une génération intense de térahertz

1. Introduction

Dans les semi-conducteurs, les porteurs de charge sont à la base d'une série de technologies importantes telles que les lasers à semi-conducteurs et les dispositifs électroluminescents, qui ont fait l'objet d'études approfondies pendant plusieurs décennies. [1-6]. La gamme des térahertz (THz), située entre les micro-ondes et l'infrarouge, est une région spectrale particulièrement intéressante pour ces études. Comme montre le montre la Figure. 1, le domaine THz couvre un spectre de fréquences allant de 0.1×10^{12} à 10×10^{12} Hz, et 1 THz équivaut à une échelle du temps de 1 picoseconde qui correspond à une longueur d'onde de 0.3 mm et à une énergie de photon de 4.14 meV [36]. Le rayonnement THz établit une liaison entre les dispositifs photoniques et électroniques en fournissant une grande quantité de largeur de bande utile.

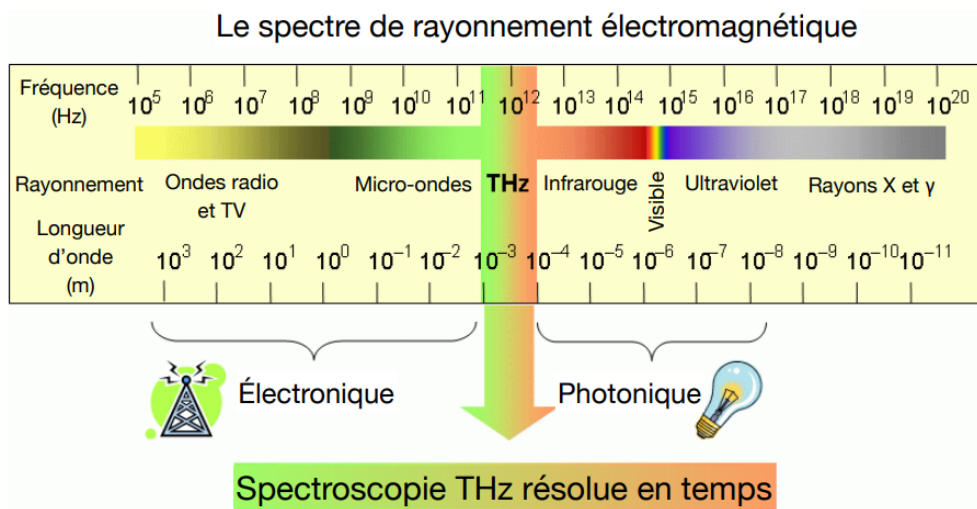


Figure 1: Le spectre de rayonnement électromagnétique. [64]

Bien que le rayonnement THz soit invisible à l'œil humain, il possède de nombreux attributs uniques et possède un grand potentiel d'applications dans notre vie quotidienne. Par exemple, de nombreux matériaux qui bloquent la lumière visible et infrarouge se révèlent transparents dans la gamme des fréquences THz [7], et le THz est sélectivement absorbé par l'eau et les substances organiques [10]. De plus, l'imagerie THz peut atteindre des résolutions spatiales à l'échelle submillimétrique, alors que l'imagerie en champ proche permet des résolutions à l'échelle nanométrique. [8]. En raison de la faible énergie des photons, les ondes THz sont également non invasives et non ionisantes. Elles ne présentent donc aucun danger pour les humains, les plantes et les animaux, en comparaison avec les rayons X [9].

Jusqu'à la fin des années 1980, les chercheurs étaient confrontés à d'énormes problèmes techniques pour générer et détecter efficacement des impulsions THz, notamment à cause de l'absence de sources laser pulsées de haute énergie et de détecteurs sensibles. Il est à noter que la première source intense de THz a été démontré par You *et al.* en 1992. [11]. Après une longue période, Blanchard *et al.* ont démontré la génération d'impulsions THz intenses par la méthode du redressement optique en utilisant un cristal de ZnTe de grande ouverture en 2007. [12]. Par ailleurs, en 2013 Ropagnol *et al.* ont développé une source THz intense intégrée aux antennes photoconductrices de grande ouverture (APCGO) fabriquées sur des cristaux de ZnSe [13,14]. Grâce à leur large bande interdite et à une rigidité diélectrique élevée, les substrats 6H-SiC et GaN sont également utilisés pour la fabrication des APCGO [15,16]. Dans la recherche de nouveaux matériaux, le cristal organique BNA et le cristal DAST sont considérés comme capables de générer un rayonnement THz intense [17,18]. Grâce à le Laboratoire de Sources Femtosecondes (LSF) installé à l'INRS-EMT, les énergies des impulsions THz générées sont de plus en plus intenses et sont passées de quelques nJ à plusieurs μJ [12-14,19-23].

Les sources THz efficaces et compactes de haute intensité nous permettent d'étudier de nombreux phénomènes non linéaires fascinants, telles que la variation de la masse effective anisotrope d'électrons chauds dans la bande non parabolique d'InGaAs [63], la diffusion interbande et intrabande des porteurs de charge [5] et la blanchiment par absorption des impulsions THz dans les semi-conducteurs dopés [1,3]. En outre, le développement de la spectroscopie THz dans le domaine temporel (THz-TDS) ouvre une nouvelle voie dans la science THz, permettant de développer diverses applications pour exploiter les possibilités uniques offertes par les ondes THz [24-28].

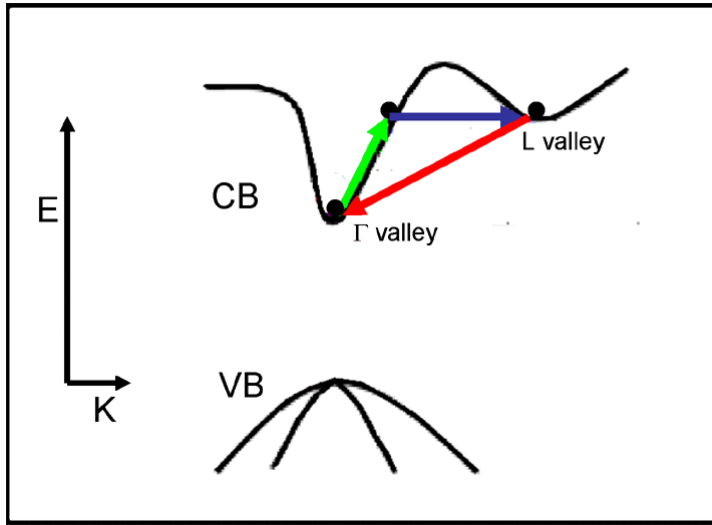


Figure 2: Mécanisme de diffusion intermittente induite par des impulsions THz intenses. Les électrons de la bande de conduction sont accélérés par le champ électrique THz (flèche verte) ; après avoir acquis suffisamment d'énergie cinétique, ils peuvent se disperser dans la vallée L [1].

L'impulsion THz peut servir de polarisation de tension transitoire, entraînant de nombreux phénomènes non linéaires dans les semi-conducteurs. Comme le montre la Figure 2 [1], les porteurs au bas de la bande de conduction sont accélérés par le champs électrique THz de haute intensité. Les électrons sont donc accélérés et gagnent de l'énergie cinétique. Lorsque l'énergie cinétique est supérieure à la séparation d'intervalle la plus proche, ils peuvent se disperser dans une vallée supérieure, par exemple, la vallée L. Dans la vallée L, la masse effective d'électrons est plus élevée ce qui induit une réduction de la mobilité des porteurs. La conséquence est une diminution de la conductivité de la couche semi-conductrice et une augmentation de la transmission des ondes THz. Ce phénomène est connue sous le nom de blanchiment par absorption ce qui est observé dans les semi-conducteurs dopés n soumis à des champs THz élevés, comme le montre la Figure 3 [14].

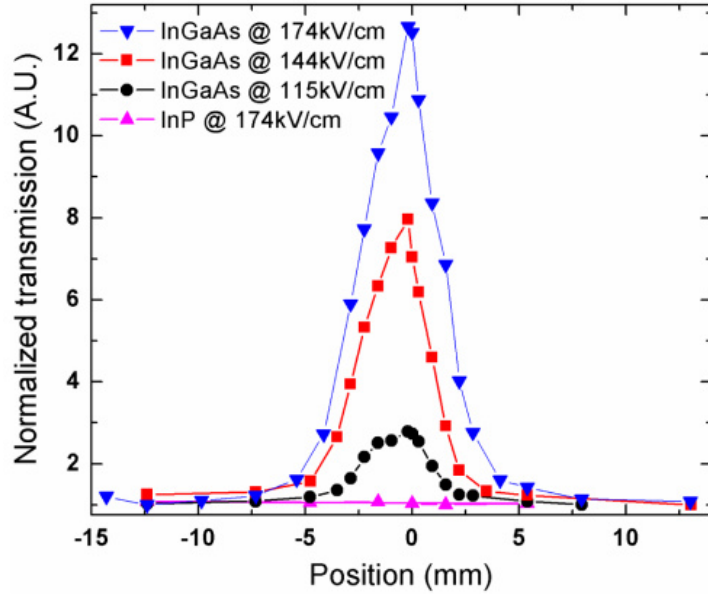


Figure 3. Intégrale temporelle normalisée du module au carré du champ électrique transmis en fonction de la position du balayage Z de l'échantillon InGaAs pour trois champs THz de crête différents (174, 144 et 115 kV/cm) et pour le substrat InP à un champ de crête de 174 kV/cm [14].

Dans ce cas précis, l'impulsion THz de haute intensité est générée par une antenne photoconductrice à grande ouverture ZnSe interdigitée [14]. Il s'agit d'une source THz compacte très efficace, qui peut générer des impulsions THz en espace libre avec une énergie allant jusqu'à $8.3 \pm 0.2 \mu\text{J}$. Cette source THz de haute intensité est très pratique puisqu'on peut facilement contrôler le champ électrique crête en appliquant un champ de polarisation spécifique.

2. Techniques de génération et de détection de THz intenses

2.1 Redressement optique

Le redressement optique est une approche largement utilisée pour la génération de rayonnement THz intense. Il s'agit d'un processus non linéaire de second ordre qui peut avoir lieu dans des milieux non centrosymétriques. Un faisceau laser femtoseconde intense se propage dans un milieu non linéaire, induisant une polarisation transitoire qui entraîne l'émission d'un rayonnement THz. Le champ électrique de l'impulsion THz générée est proportionnel à la dérivée temporelle du second ordre de la polarisation induite [38-42].

Une configuration simple pour le rayonnement THz généré par le processus de rectification optique est illustrée à la Figure 4. Comme mentionné ci-dessus, lorsqu'un faisceau laser femtoseconde intense se propage à travers un milieu non linéaire de second ordre, une polarisation transitoire est induite, entraînant l'émission de rayonnement THz. Le champ électrique de l'impulsion THz générée est proportionnel à la dérivée seconde de cette polarisation.

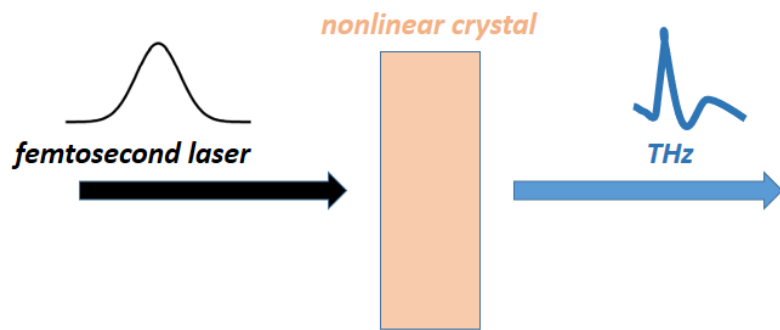


Figure 4. Schéma de la génération THz par redressement optique dans un cristal non linéaire. Une impulsion laser femtoseconde, traversant un milieu non linéaire, génère une impulsion THz à large bande en utilisant des processus de génération de fréquence de différence.

Avec la configuration présentée ci-dessus, les chercheurs ont démontré la génération de rayonnement THz intense et à large bande en utilisant des cristaux non linéaires tels que le LiNbO₃, le ZnTe, le GaAs, le CdTe, le GaP, le DAST et le BNA [37, 43-45]. Il a été montré que les cristaux moléculaires organiques comme le DAST sont plus efficaces que les cristaux de ZnTe de même épaisseur, mais ils sont plus fragiles et souffrent normalement de seuils de dommages plus bas [46-48].

2.2 L'antennes photoconductrices (APC)

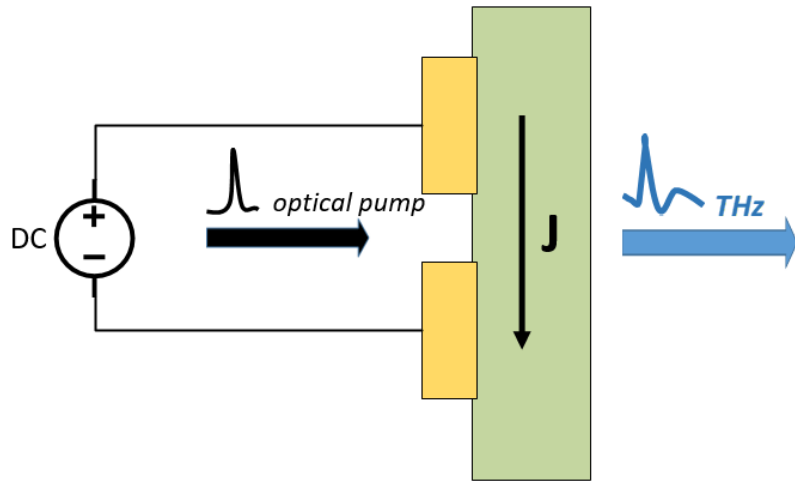


Figure 5. Schéma d'une antenne photoconductrice (APC). Une tension de polarisation est appliquée au substrat semi-conducteur pour piloter les porteurs photoexcités.

Comme le montre la Figure 5, l'APC se compose généralement d'un substrat semi-conducteur de haute résistivité avec deux électrodes déposées sur une seule face [21]. L'impulsion laser femtoseconde illumine le substrat semi-conducteur où les électrodes métalliques ont été déposées, et un champ de polarisation est appliqué. Si l'énergie des photons de l'impulsion laser femtoseconde est supérieure à la bande interdite, les photons peuvent être absorbés par le substrat et les porteurs sont excités de la bande de valence à la bande de conduction. Ces porteurs libres sont accélérés par le champ de polarisation pour générer un photo-courant. Les variations de la densité de photo-courant sont dans une échelle de temps picoseconde ce qui entraînent la génération d'ondes électromagnétiques pulsées qui se situent dans la gamme de fréquences THz.

Une propriété unique de ces impulsions THz générées est la grande asymétrie dans l'amplitude des composantes positive et négative du profil temporel. Ici, une impulsion THz quasi-demi-cycle est générée naturellement. La deuxième propriété unique des ondes THz générées est la présence de basse fréquence, typiquement dans la plage de fréquences inférieure à 1 THz puisque comprise entre 0.05 et 1 THz. Pour générer des impulsions THz à haute énergie, il est nécessaire d'augmenter l'ouverture de l'APC. Par conséquent, des antennes photoconductrices à grande ouverture (APCGO) ont été étudiées et développées [49,50].

$$E_{far}(t) \propto \frac{\partial J}{\partial t} \propto E_{bias} \frac{\partial \sigma}{\partial t} \quad (1)$$

Comme le montre l'équation (1), le champ électrique THz est proportionnel au champ de polarisation E_{bias} et à la dérivée temporelle de la conductivité de surface σ . La rigidité diélectrique détermine le champ électrique de polarisation le plus élevé qui peut être appliqué à

un APC avant qu'une dégradation ne se produise. Et la rigidité diélectrique E_c est liée à la bande interdite E_G , donnée par une formule empirique [51]:

$$E_c = 1.36 \times 10^7 \left(\frac{E_G}{4}\right)^3 \quad (2)$$

Apparemment, une petite différence de bande interdite entraînera une énorme variation de la rigidité diélectrique. Ceci est très important pour augmenter l'intensité des APCGOs puisque le champ électrique de crête THz est linéairement proportionnel au champ électrique de polarisation. À partir de cette équation, nous constatons que l'utilisation d'un semi-conducteur à large bande interdite comme substrat de APCGO est très favorable.

2.3 Détection THz avec une APC

L'APC est également largement utilisée pour la détection des ondes THz [52]. Une impulsion laser femtoseconde éclaire l'espace interélectrode ce qui génère des porteurs dans la bande de conduction. Les porteurs excités sont accélérés par le champ électrique THz. Cela conduit à un signal de photocourant transitoire à travers l'espace d'antenne. Nous pouvons détecter le champ électrique THz du photocourant transitoire à l'aide d'un amplificateur.

$$I(t) \propto \int_{-\infty}^t \sigma_s(t-t') E_{THz}(t') dt' \quad (3)$$

Un facteur qui affecte grandement le signal détecté est la taille de l'APC. Par exemple, une taille d'écart plus petite permettra la détection de signaux de fréquence et d'amplitude plus élevées, tandis que des électrodes plus longues augmenteront l'amplitude du signal détecté mais seront plus sensibles aux basses fréquences [53].

2.4 L'échantillonnage électro-optique

Pour l'échantillonnage électro-optique, une impulsion laser femtoseconde à polarisation linéaire se superpose avec une impulsion THz picoseconde dans le cristal électro-optique. Le champ électrique THz induit une biréfringence dans le cristal, qui modifie la polarisation de l'impulsion laser en la chevauchant linéairement. Le changement de phase entre les deux composantes de la polarisation du faisceau sonde (qui est proportionnel au champ électrique THz) peut être mesuré en utilisant des polariseurs croisés installés avant et après le cristal détecteur. Dans ce cas, le changement de phase apparaît comme une modulation dans l'intensité du faisceau sonde. La forme d'onde THz complète peut être reconstruite en balayant le faisceau sonde sur la totalité de l'impulsion THz. Un schéma de cette technique est illustré à la Figure 6.

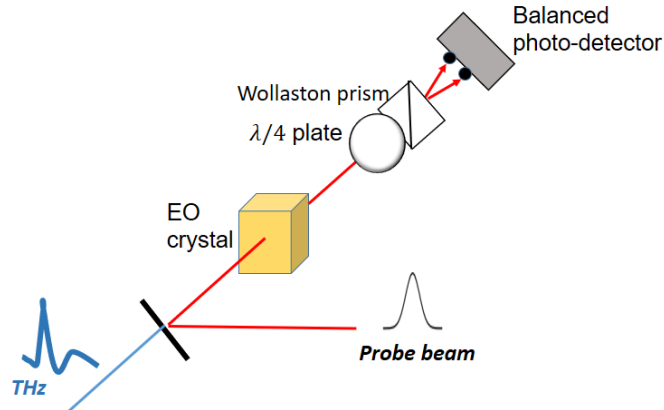


Figure 6. Schéma de détection THz utilisant la technique d'échantillonnage EO.

3. Spectroscopie THz résolue en temps (THz-TDS)

Spectroscopie THz résolue en temps (THz-TDS) est une technique spectroscopique dans laquelle les propriétés de la matière sont détectées avec des impulsions. Étant donné que THz-TDS détermine à la fois l'amplitude et la phase du rayonnement THz, il peut être parfaitement utilisé pour évaluer les constantes diélectriques complexes de divers matériaux [54-62].

En considérant la transmission et la réflexion du champ de Fresnel pour une incidence normale, on peut obtenir les formules suivantes:

$$n(\omega) = 1 + \frac{\varphi(\omega)c}{\omega d} \quad (4)$$

$$\alpha(\omega) = -\frac{2}{d} \ln \left(\frac{(n+1)^2}{4n} T(\omega) \right) \quad (5)$$

Ici, n est l'indice de réfraction, α est le coefficient d'absorption et ω est la fréquence angulaire. La différence de phase $\varphi(\omega) = \varphi_{sam}(\omega) - \varphi_{ref}(\omega)$, c est la vitesse de la lumière dans le vide et d est l'épaisseur de l'échantillon. $T(\omega) = \frac{E_{sam}}{E_{ref}}$, où E_{sam} et E_{ref} sont respectivement le spectre en amplitude du signal transmis au travers de l'échantillon et de la référence obtenues par transformée de Fourier.

Pour obtenir la différence de phase entre l'échantillon et le signal de référence, il est nécessaire d'ajuster des phases. Nous pouvons obtenir la phase non-ajustée (unwrapped phase en anglais) à partir du logiciel Origin, mais ce logiciel peut nous donner des erreurs automatiques, comme le montre la Figure 7 (a). La stratégie d'ajustement de phase la plus stable consiste à s'assurer que la pente de la phase à dérouler est aussi faible que possible, afin de minimiser la possibilité d'une surcompensation de phase non intentionnelle. Comme le montre la Figure 7 (b), avec l'inclusion de la phase globale des signaux dans la procédure de déroulement, le déroulement fonctionne

maintenant comme prévu, puisque la soustraction des phases globales des signaux conduit à des variations plutôt faibles du spectre de phase.

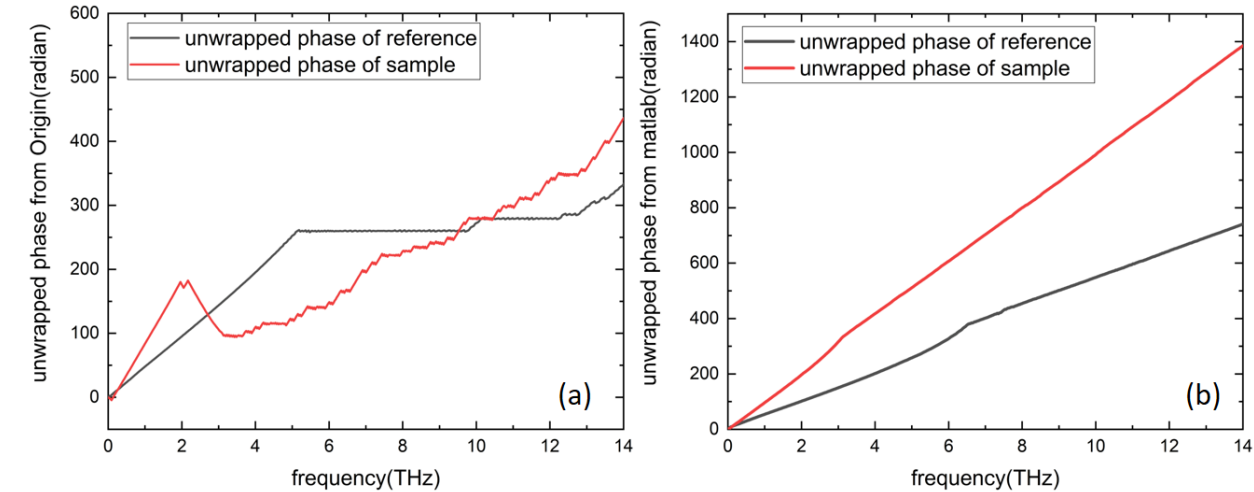


Figure 7. Phase non emballée (a) de Origin (avant correction), (b) de MATLAB (après correction).

Une mesure THz-TDS de l'échantillon de CdTe est effectuée à l'École de technologie supérieure (ÉTS). Le système est basé sur les APCs pour l'émission et la détection avec une puissance optique de 20 mW à une longueur d'onde de 800 nm pour l'émetteur et le détecteur. L'indice de réfraction et le coefficient d'absorption mesuré de l'échantillon de CdTe sont très précis, comme le montrent la Figure 8 et la Figure 9, respectivement.

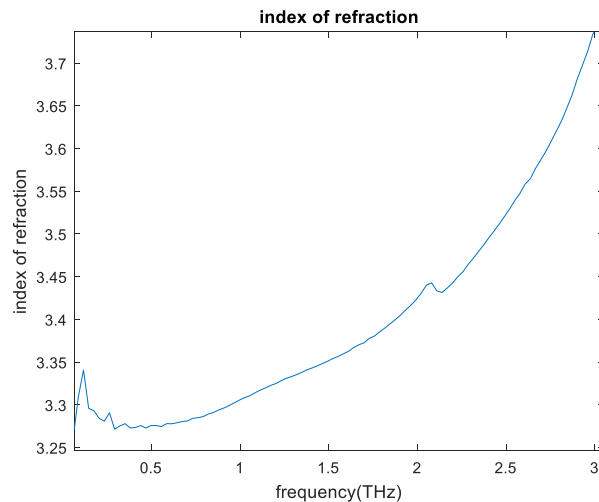


Figure 8. Indice de réfraction de l'échantillon CdTe.

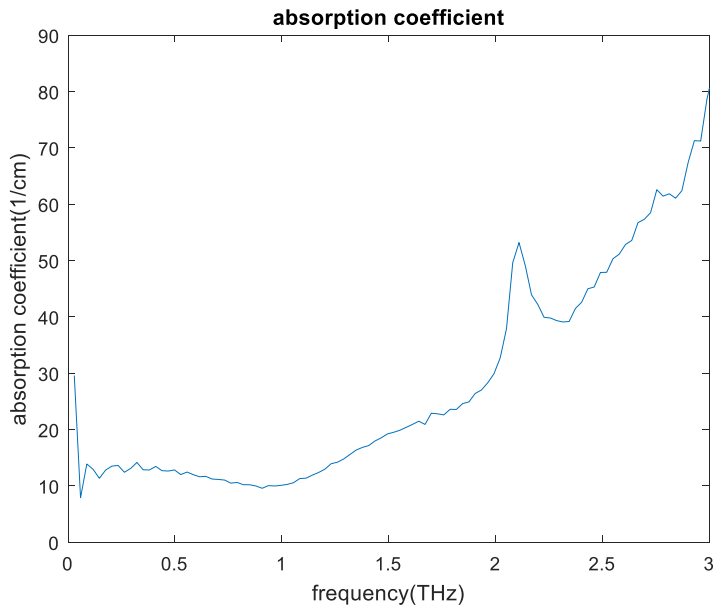


Figure 9. Coefficient d'absorption de l'échantillon de CdTe.

Comme le montre la figure 10 (B), nos résultats pour la caractérisation de CdTe sont très proches de la littérature.

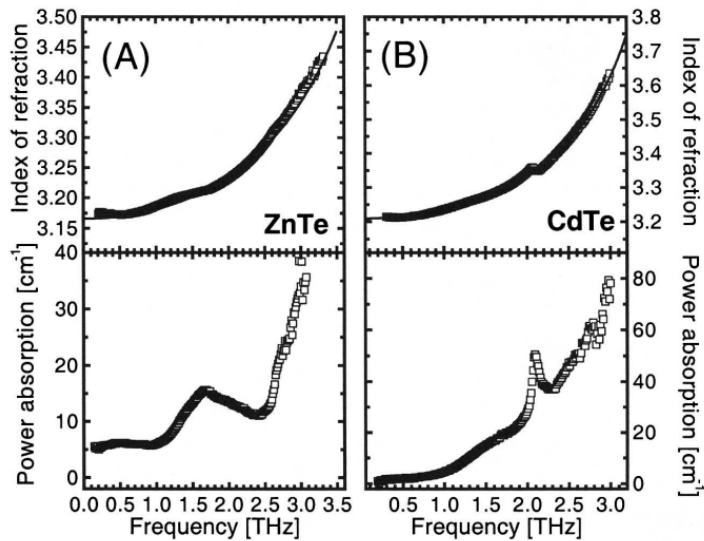


Figure 10. Indice de réfraction et coefficient d'absorption de (A) ZnTe et (B) CdTe de la littérature [65].

4. Augmentation de l'intensité THz générée par APCGO

Lorsqu'une tension de claquage entre les électrodes se produit, l'air est ionisé et devient un conducteur électrique, empêchant l'APC de fonctionner. Nous pouvons fabriquer des APC en utilisant des semi-conducteurs avec une bande interdite légèrement inférieure à l'énergie des photons de l'impulsion laser, ce qui permet une absorption efficace avec une efficacité quantique élevée. Il est également très prometteur qu'en recouvrant l'APC d'isolants comme TiO_2 , Si_3N_4 et Al_2O_3 , nous puissions éviter le claquage d'air, générant ainsi un rayonnement THz intense.

Nous utilisons des substrats GaAs à haute résistivité (MTI Corporation GAUa101005S2US) pour fabriquer des APC. Le GaAs est non dopé avec deux faces polies et fait croître par la méthode VGF avec une dimension de 10 x 10 x 0.5 mm. L'orientation est (100) et la résistivité est de $0.6\sim 2 \times 10^8 \Omega \cdot cm$.

L'antenne de GaAs est fabriquée par photolithographie et dépôt par faisceau électronique. Les électrodes de l'antenne sont réalisées en utilisant 5 nm de chrome et 80 nm d'or. L'antenne est fixée sur le support à l'aide de peinture à l'argent et de soudure, comme illustré à la Figure 11.

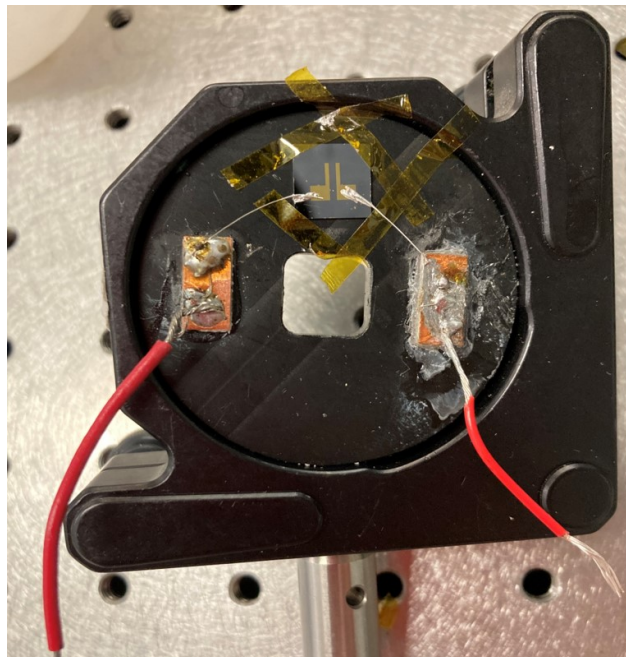


Figure 11. GaAs PCA fixé sur la monture.

Nous augmentons progressivement la tension de polarisation appliquée à l'antenne GaAs. Lorsqu'un champ de polarisation de 23.3 kV/cm est appliqué, on observe la génération d'un flash de lumière indiquant le claquage de l'air par la tension, comme le montre la Figure 12.

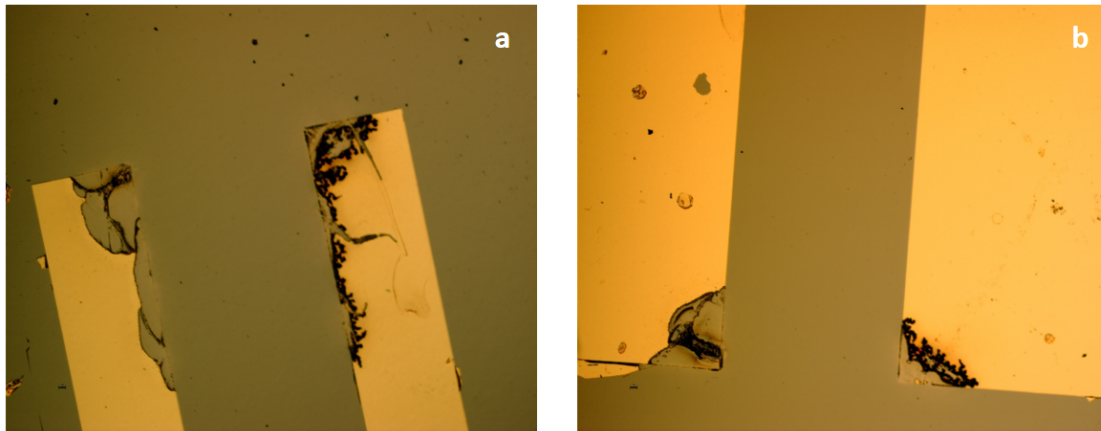


Figure 12. Lorsqu'un champ de polarisation de 23.3 kV/cm est appliqué, on observe la génération d'un flash de lumière indiquant le claquage de l'air par la tension.

Le champ de claquage de l'APC de GaAs avec un revêtement époxy est mesuré à 53.3 kV/cm. Nous avons démontré avec succès qu'en recouvrant l'APC de GaAs avec une couche d'époxy, nous pouvons dépasser la limite de la force diélectrique de l'air et donc appliquer des champs de polarisation plus élevés entre les électrodes de l'APC.

L'APC de GaAs est utilisé pour générer le rayonnement THz. La Figure 13 montre le schéma de la configuration. Un cristal CdTe de 1 mm d'épaisseur (110) est utilisé comme détecteur THz. Un cristal de triborate de lithium (LBO) est utilisé pour générer la deuxième harmonique du laser à 1045 nm, permettant au faisceau laser d'exciter les porteurs de la bande de valence à la bande de conduction dans le substrat GaAs. Le faisceau laser d'une puissance de pompe de 84 mW est focalisé sur l'entrefer du GaAs APC, et le faisceau sonde est focalisé sur le détecteur à cristal CdTe.

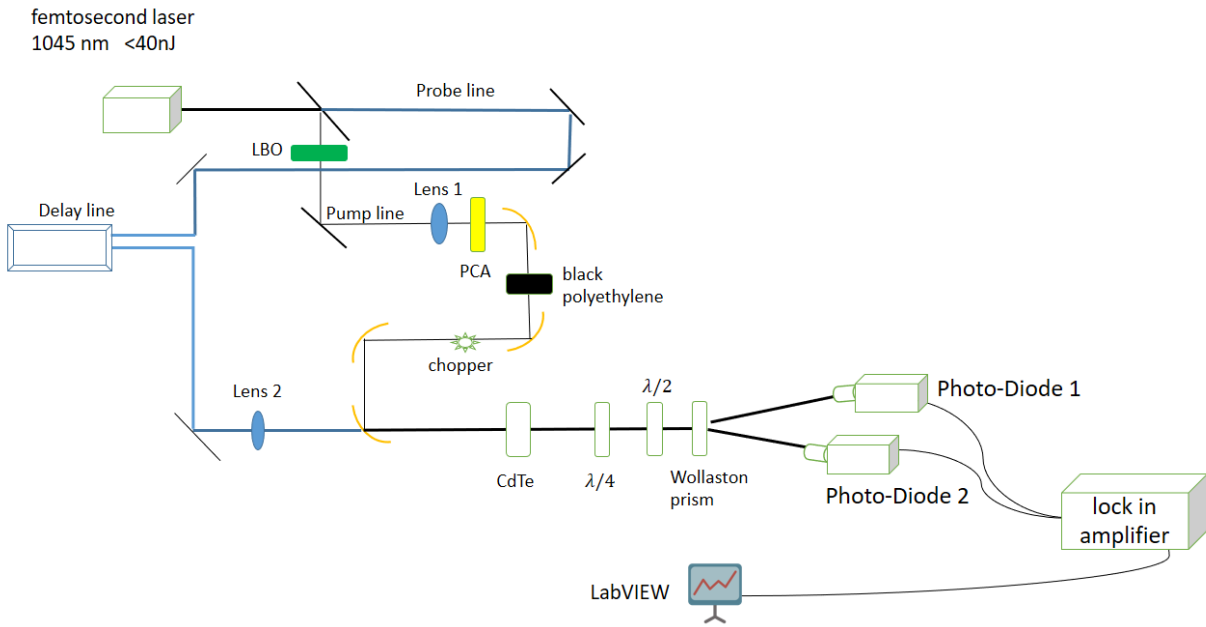


Figure 13. Schéma de la configuration utilisant GaAs APC comme émetteur THz.

La résistance à l'obscurité est mesurée à $25\text{ M}\Omega$. Lorsque le faisceau laser est focalisé sur le APC, la résistance diminue à $130\text{ k}\Omega$. Nous augmentons la tension de polarisation de 200 V à 550 V, le courant sur le APC augmente de 1.5 mA à 2.15 mA et la Figure 14 montre les formes d'onde THz à différentes tensions de polarisation.

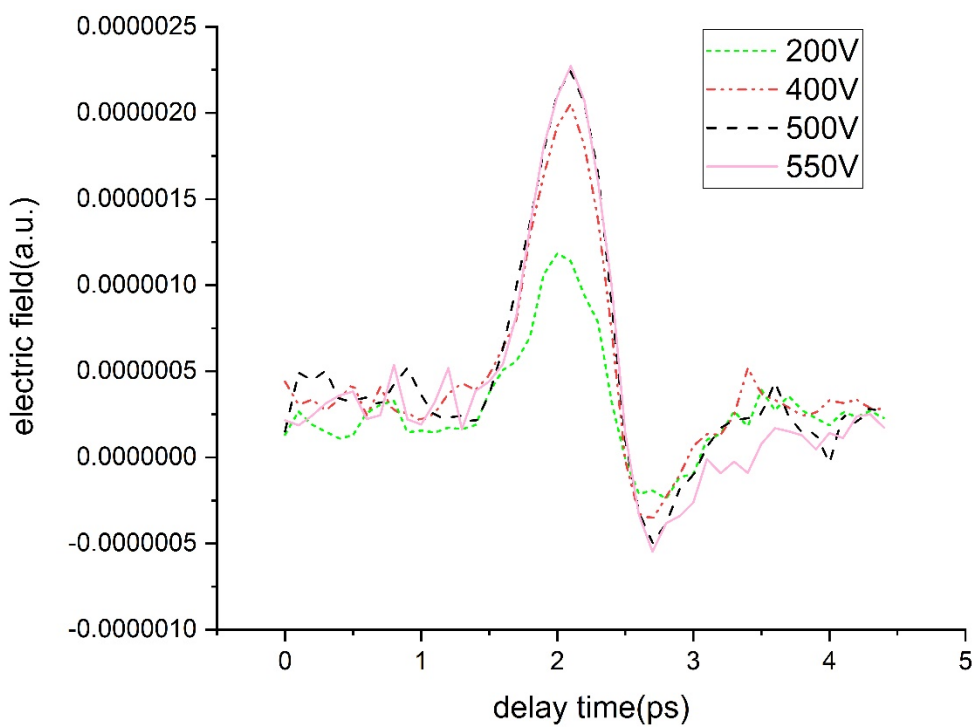


Figure 14. Formes d'onde THz à différentes tensions de polarisation. Le champ électrique de crête THz augmente à mesure que la tension de polarisation augmente.

La relation entre le champ électrique de THz crête et le champ de polarisation appliqué est illustrée à la Figure 15.

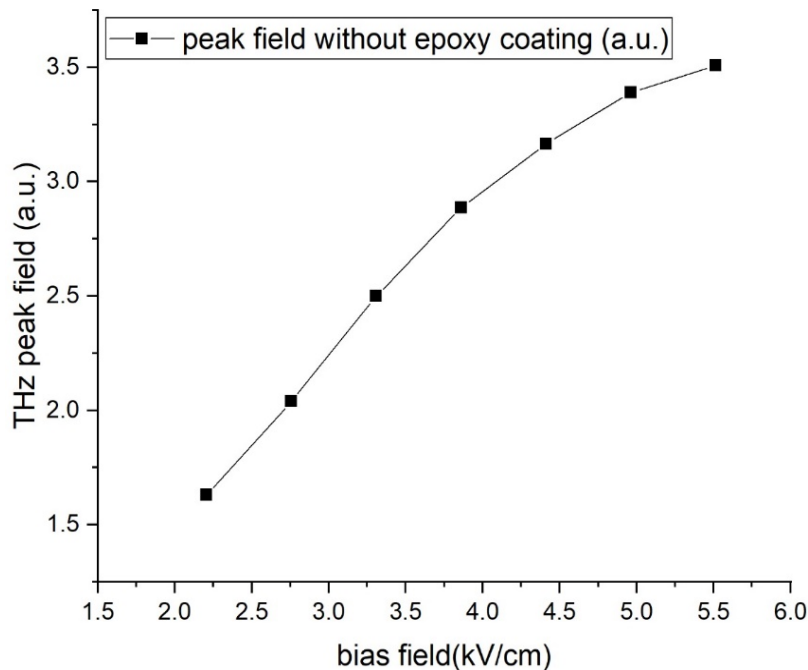


Figure 15. Relation entre le champ électrique de crête THz et le champ de polarisation appliquée. De 2.2 kV/cm à 4.4 kV/cm, le champ électrique de crête THz évolue linéairement avec le champ de polarisation.

Le champ électrique de pointe THz évolue linéairement lorsque le champ de polarisation est dépassé de 2.2 kV/cm à 4.4 kV/cm, ce qui est conforme à l'équation suivante (1). Cependant, on observe un effet de saturation lorsque le champ de polarisation est supérieur à 4.4 kV/cm. En effet, il a été démontré que l'APC de GaAs subissent souvent une dégradation importante au cours du temps et une défaillance ultérieure, principalement en raison de l'augmentation de la température résultant du chauffage par effet Joule [15]. La défaillance du GaAs APC avec un revêtement époxy après application d'un champ de polarisation de 5.5 kV/cm est observée, comme le montre la Figure 16. Le revêtement époxy peut empêcher le APC de dissiper la chaleur. En raison de l'augmentation de la température, une certaine électromigration des électrodes en or s'est produite, entraînant un court-circuit électrique total du circuit électronique empêchant le APC de fonctionner.

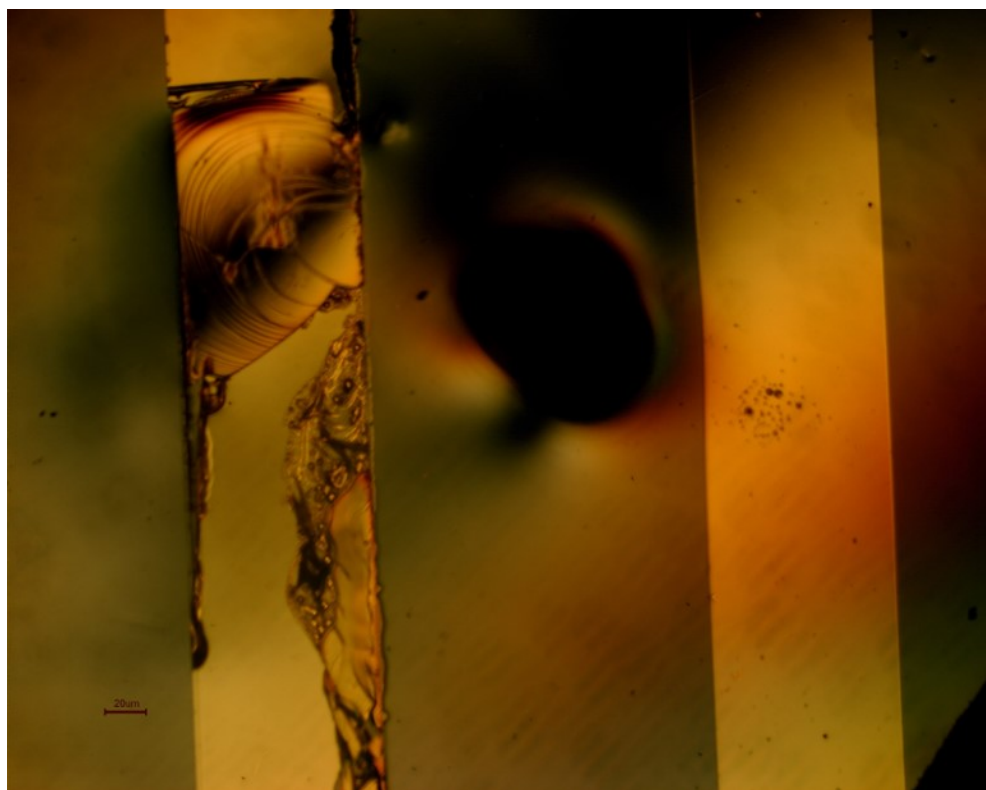


Figure 16. Défaillance de GaAs APC après application d'un champ de polarisation de 5.5 kV/cm, due à l'augmentation de la température.

Les formes d'ondes THz générées à partir de l'APC avec et sans revêtement d'époxy sont illustrées à la Figure 17. On constate qu'en recouvrant l'APC de GaAs avec la résine d'époxy, le champ électrique crête THz augmente d'un facteur 1.37 et 1.66 respectivement pour une tension de polarisation de 200 V et 400 V.

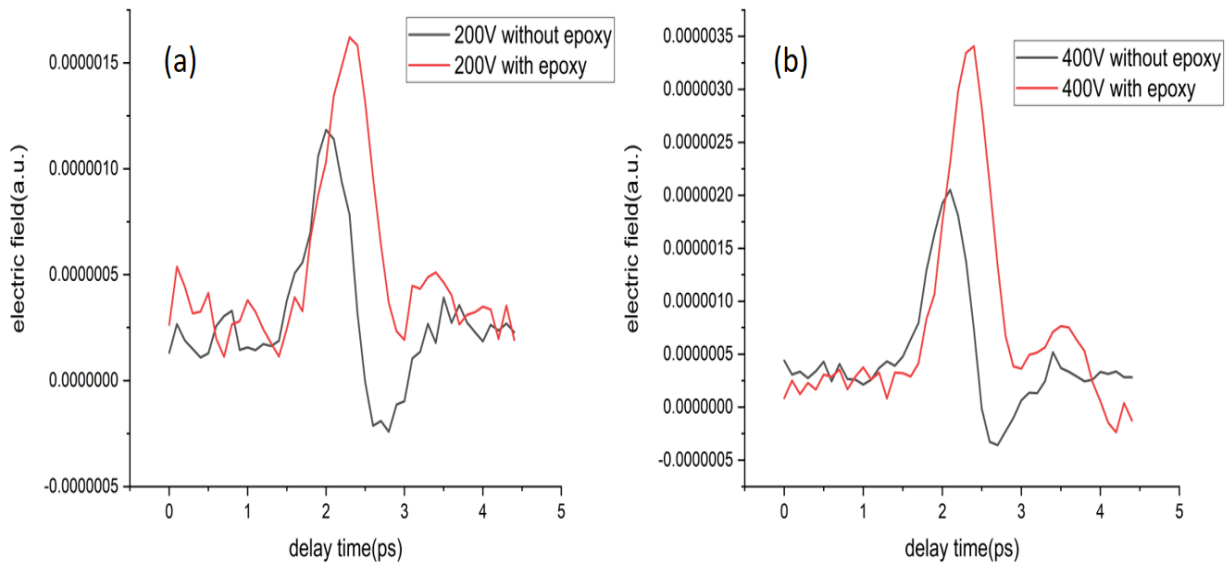


Figure 17. Forme d'onde THz (a) à une tension de polarisation de 200 V, (b) à une tension de polarisation de 400 V, avec (courbe rouge) et sans le revêtement époxy (courbe noire). En recouvrant le GaAs APC avec la résine époxy, le champ électrique de crête THz augmente.

Pour explorer cette amélioration du champ électrique de crête THz après avoir recouvert l'APC de GaAs avec la résine époxy, nous effectuons des simulations calculant l'intensité laser irradiant la surface de GaAs à l'aide de FDTD solutions. Le schéma est illustré à la Figure 18.

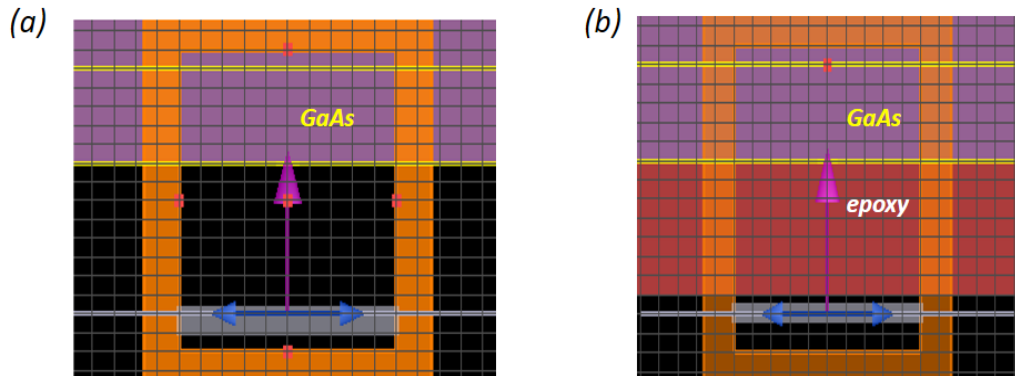


Figure 18. Schéma du laser femtoseconde 522 nm transmettant (a) dans un substrat GaAs. (b) dans un substrat GaAs avec un revêtement époxy.

S'il y a une amélioration de l'intensité du laser irradiant la surface de GaAs après avoir recouvert le substrat de GaAs avec l'époxy, davantage de porteurs seront générés dans le substrat de GaAs.

Les résultats calculés de l'intensité laser irradiant la surface de GaAs sans et avec le revêtement époxy sont présentés dans la Figure 19 et la Figure 20, respectivement.

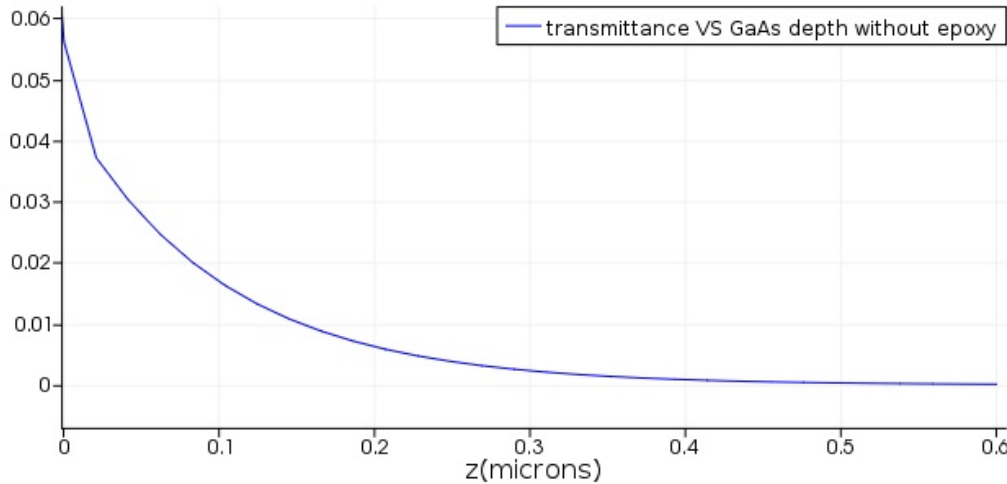


Figure 19. L'intensité du laser après avoir traversé z microns de GaAs sans couche époxy.

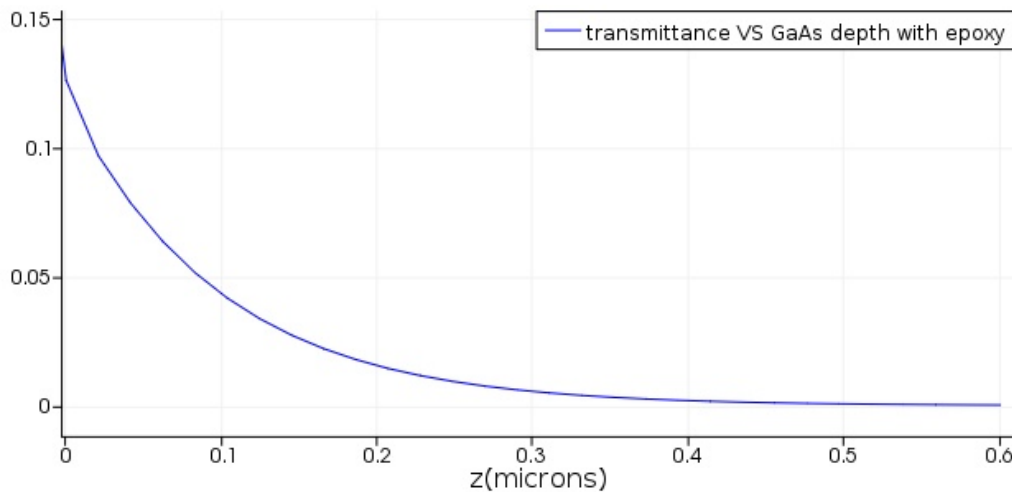


Figure 20. L'intensité du laser après avoir traversé z microns de GaAs avec la couche époxy.

Le faisceau laser de 522 nm est incident sur la surface GaAs à $z = 0$. Sans le revêtement époxy, l'intensité laser incidente sur la surface GaAs est de 0.056. Alors qu'avec la couche époxy, l'intensité du laser incident sur la surface de GaAs est de 0.126. À une profondeur de 0.6 micron, l'intensité du laser diminue à 10^{-6} , ce qui signifie que GaAs absorbe presque complètement le

faisceau laser de 522 nm. L'intensité du laser après avoir traversé z microns de GaAs sans couche époxy peut être exprimée comme suit:

$$T_1 = 0.056 \times e^{-z/D} \quad (6)$$

Ici, D est une constante. L'intensité du laser après avoir traversé z microns de GaAs avec la couche époxy peut être exprimée comme suit:

$$T_2 = 0.126 \times e^{-z/D} \quad (31)$$

Comme nous pouvons le voir, après avoir recouvert le GaAs APC avec la couche époxy, l'intensité du laser irradiant la surface de GaAs augmente de 2.25 fois (T_2/T_1), ce qui signifie que plus de photons seront absorbés par le substrat de GaAs, et donc plus de porteurs devraient être générés dans le substrat GaAs. Selon l'équation (1), le champ électrique THz généré devrait augmenter à mesure que la densité de porteurs augmente.

5. Perspectives

Dans cette thèse, nous avons discuté des techniques de génération et de détection du rayonnement THz, étudié la méthode THz-TDS et étudié des nouvelles méthodes pour augmenter l'intensité THz. L'APCGO peut générer des ondes THz intenses, ce qui permet d'étudier de nombreux phénomènes non linéaires fascinants.

Nous avons démontré avec succès la génération de rayonnement THz à partir de l'APC de GaAs, qui fournit la base d'APCGO. Grace à l'encapsulation par l'époxy, il a également été démontré que nous pouvions dépasser la limite du claquage de l'air et appliquer des champs de polarisation 2.28 fois plus élevés à l'APC.

Une amélioration du champ électrique THz est observée après avoir recouvert l'APC GaAs d'une couche d'époxy. Nous illustrons cette amélioration en interprétant le revêtement époxy comme une couche antireflet, à travers laquelle la transmission est améliorée. Par conséquent, le champ électrique THz augmente en raison de l'amélioration de la densité de porteurs de charge dans le substrat GaAs.

Cependant, nous avons observé une dégradation de l'APC de GaAs avec un revêtement époxy après avoir appliqué un champ de polarisation de 5.5 kV/cm. Comme nous le savons, les APC de GaAs subissent souvent une dégradation importante au cours du temps et une défaillance ultérieure, principalement en raison de l'augmentation de la température résultant du chauffage par effet Joule. En raison de cette augmentation de température, une certaine électromigration des électrodes en or s'est produite, entraînant un court-circuit électrique qui empêche le fonctionnement de l'APC. Par conséquent, il est préférable de choisir des substrats semi-conducteurs à haute conductivité thermique afin de dissiper la chaleur.

D'autres travaux expérimentaux et théoriques sont nécessaires pour comprendre l'amélioration du champ électrique THz après encapsulation. De plus, nous pouvons utiliser des semi-conducteurs à haute conductivité thermique et à large bande interdite comme le 6H-SiC pour fabriquer l'APCGO et appliquer des champs de polarisation élevés au-delà de la limite de claquage de l'air par passivation de surface pour générer un rayonnement THz intense.

Références

- [1] G. Sharma, L. Razzari, F. H. Su, F. Blanchard, A. Ayesheshim, T. L. Cocker, L. V. Titova, H. C. Bandulet, T. Ozaki, J. C. Kieffer, R. Morandotti, M. Reid, and F. A. Hegmann, "Time-Resolved Terahertz Spectroscopy of Free Carrier Nonlinear Dynamics in Semiconductors," *IEEE Photonics J.* 2, 578 (2010).
- [2] X. Chai, X. Ropagnol, S. M. Raeis-Zadeh, M. Reid, S. Safavi-Naeini, and T. Ozaki, "Subcycle Terahertz Nonlinear Optics," *Phys. Rev. Lett.* 121, 143901 (2018).
- [3] L. Razzari, F. H. Su, G. Sharma, F. Blanchard, A. Ayesheshim, H. C. Bandulet, R. Morandotti, J. C. Kieffer, T. Ozaki, M. Reid, and F. A. Hegmann, "Nonlinear ultrafast modulation of the optical absorption of intense few-cycle terahertz pulses in n-doped semiconductors," *Phys. Rev. B* 79, 193204 (2009).
- [4] J. T. Devreese and R. G. van Welzenis, "Impact Ionisation Probability in InSb," *Appl. Phys. A* 29, 125-132 (1982).
- [5] X. Chai, X. Ropagnol, A. Ovchinnikov, O. Chefonov, A. Ushakov, C. M. Garcia-Rosas, E. Isgandarov, M. Agranat, T. Ozaki, and A. Savel'ev, "Observation of crossover from intraband to interband nonlinear terahertz optics," *Optics Letters* Vol. 43, Issue 21, pp. 5463-5466 (2018).
- [6] P. Lugli, P. Bordone, L. Reggiani, M. Rieger, P. Kocevar, and S. M. Goodnick, "Monte Carlo studies of nonequilibrium phonon effects in polar semiconductors and quantum wells. I. Laser photoexcitation," *Phys. Rev. B* 39, 7852 (1989).
- [7] J. E. Bjarnason, T. L. J. Chan, A. W. M. Lee, M. A. Celis, and E. R. Brown, "Millimeter-wave, terahertz, and mid-infrared transmission through common clothing," *Appl. Phys. Lett.* 85, 519 (2004).
- [8] K. Ahi and M. Anwar, "A survey on GaN-based devices for terahertz photonics," *Proc. SPIE*, vol. 9957, pp. 99570A-1–99570A-13, 2016.
- [9] Kiarash Ahi, "Mathematical Modeling of THz Point Spread Function and Simulation of THz Imaging Systems," *IEEE Transactions on Terahertz Science and Technology*, vol. 7, no. 6, pp. 747-754, Nov. 2017.
- [10] Anastasiia Tukmakova, Ivan Tkhorzhevskiy, Artyom Sedinin, Aleksei Asach, Anna Novotelnova, Natallya Kablukova, Petr Demchenko, Anton Zaitsev, Dmitry Zykov and Mikhail Khodzitsky, "FEM Simulation of Frequency-Selective Surface Based on Thermoelectric Bi-Sb Thin Films for THz Detection," *Photonics* 2021, 8, 119.
- [11] D. You, R. R. Jones, P. H. Bucksbaum, and D. R. Dykaar, "Generation of high-power sub-single-cycle 500-fs electromagnetic pulses," *Optics Letters* Vol. 18, Issue 4, pp. 290-292 (1993).
- [12] F. Blanchard, L. Razzari, H.-C. Bandulet, G. Sharma, R. Morandotti, J.-C. Kieffer, T. Ozaki, M. Reid, H. F. Tiedje, H. K. Haugen, and F. A. Hegmann, "Generation of 1.5 μ J single-cycle terahertz pulses by optical rectification from a large aperture ZnTe crystal," *Optics Express* Vol. 15, Issue 20, pp. 13212-13220 (2007).

- [13] X. Ropagnol, F. Blanchard, T. Ozaki, and M. Reid, "Intense terahertz generation at low frequencies using an interdigitated ZnSe large aperture photoconductive antenna," *Appl. Phys. Lett.* 103, 161108 (2013).
- [14] X. Ropagnol, M. Khorasaninejad, M. Raeiszadeh, S. Safavi-Naeini, M. Bouvier, C. Y. Côté, A. Laramée, M. Reid, M. A. Gauthier, and T. Ozaki, "Intense THz Pulses with large ponderomotive potential generated from large aperture photoconductive antennas," *Opt. Express* 24, 11299 (2016).
- [15] X. Ropagnol, Marcel Bouvier, M. Reid, and T. Ozaki, "Improvement in thermal barriers to intense terahertz generation from photoconductive antennas," *Journal of Applied Physics* 116, 043107 (2014).
- [16] X Ropagnol, Zs Kovács, B Gilicze, M Zhuldybina, F Blanchard, C M Garcia-Rosas, S Szatmári, I B Földes and T Ozaki, "Intense sub-terahertz radiation from wide-bandgap semiconductor based large-aperture photoconductive antennas pumped by UV lasers," *New J. Phys.* 21 (2019) 113042.
- [17] Hang Zhao, Yong Tan, Tong Wu, Gunther Steinfeld, Yan Zhang, Cunlin Zhang, Liangliang Zhang, and Mostafa Shalaby, "Efficient broadband terahertz generation from organic crystal BNA using near infrared pump," *Appl. Phys. Lett.* 114, 241101 (2019).
- [18] Mostafa Shalaby and Christoph P. Hauri, "Demonstration of a low-frequency three-dimensional terahertz bullet with extreme brightness," *Nat Commun* 6, 5976 (2015).
- [19] Francois, G. Sharma, X. Ropagnol, L. Razzari, R. Morandotti, and T. Ozaki, "Improved terahertz two-color plasma sources pumped by high intensity laser beam," *Opt. Express* 17, 6044 (2009).
- [20] F. Blanchard, G. Sharma, L. Razzari, X. Ropagnol, H.-C. Bandulet, F. Vidal, R. Morandotti, J.-C. Kieffer, T. Ozaki, H. Tiedje, H. Haugen, M. Reid, and F. Hegmann, "Generation of Intense Terahertz Radiation via Optical Methods," *IEEE J. Select. Topics Quantum Electron.* 17, 5 (2011).
- [21] X. Ropagnol, R. Morandotti, T. Ozaki, and M. Reid, "THz pulse shaping and improved optical-to-THz conversion efficiency using a binary phase mask," *Opt. Lett.* 36, 2662 (2011).
- [22] F. Blanchard, X. Ropagnol, H. Hafez, H. Razavipour, M. Bolduc, R. Morandotti, T. Ozaki, and D. G. Cooke, "Effect of extreme pump pulse reshaping on intense terahertz emission in lithium niobate at multimilliJoule pump energies," *Opt. Lett.* 39, 4333 (2014).
- [23] S. Mondal, H. A. Hafez, X. Ropagnol, and T. Ozaki, "MV/cm terahertz pulses from relativistic laser-plasma interaction characterized by nonlinear terahertz absorption bleaching in n-doped InGaAs," *Opt. Express* 25, 17511 (2017).
- [24] Bernd M. Fischer, Matthias Hoffmann, Hanspeter Helm, Rafal Wilk, Frank Rutz, Thomas Kleine-Ostmann, Martin Koch, and Peter Uhd Jepsen, "Terahertz time-domain spectroscopy and imaging of artificial RNA," *Optics Express* Vol. 13, Issue 14, pp. 5205-5215 (2005).
- [25] Jianming Dai, Jiangquan Zhang, Weili Zhang, and D. Grischkowsky, "Terahertz time-domain spectroscopy characterization of the far-infrared absorption and index of refraction of high-resistivity, float-zone silicon," *J. Opt. Soc. Am. B/Vol.* 21, No. 7/July 2004.
- [26] M. Naftalya and R. E. Miles, "Terahertz time-domain spectroscopy of silicate glasses and the relationship to material properties," *J. Appl. Phys.* 102, 043517 (2007).

- [27] S. Karthick, D. Ganesh, K. Thirupugalmani, A.K. Chaudhary, S. Brahadeeswaran, "Terahertz generation and optical properties of N-benzyl-2-methyl-4-nitroaniline single crystals in 0.1–2.0 THz range for photonic applications," *Materials Letters* 246 (2019) 95–98.
- [28] Isaac C. Tangen, Gabriel A. Valdivia-Berroeta, Larry K. Heki, Zachary B. Zaccardi, Erika W. Jackson, Charles B. Bahr, David J. Michaelis, and Jeremy A. Johnson, "Comprehensive Characterization of Terahertz Generation with the Organic Crystal BNA," *Journal of the Optical Society of America B* Vol. 38, Issue 9, pp. 2780–2785 (2021).
- [36] Y.-S. Lee, *Principles of Terahertz Science and Technology*. New York: Springer, 2008.
- [37] X. Ropagnol, M. Matoba, J. E. Nkeck, F. Blanchard, E. Isgandarov, J. Yumoto, and T. Ozaki, "Efficient terahertz generation and detection in cadmium telluride using ultrafast ytterbium laser," *Appl. Phys. Lett.* 117, 181101 (2020).
- [38] A. Rice, Y. Jin, X. F. Ma, X. C. Zhang, D. Bliss, J. Larkin, *et al.*, "Terahertz optical rectification from zinc-blende crystals," *Applied Physics Letters*, Vol. 64, p. 1324, 1994.
- [39] B. B. Hu, X. C. Zhang, D. H. Auston, and P. R. Smith, "Free-space radiation from electro-optic crystals," *Applied Physics Letters*, Vol. 56, p. 506, 1990.
- [40] A. Nahata, D. H. Auston, T. F. Heinz, and C. Wu, "Coherent detection of freely propagating terahertz radiation by electro-optic sampling," *Applied Physics Letters*, Vol. 68, p. 150, 1996.
- [41] M. Nagai, K. Tanaka, H. Ohtake, T. Bessho, T. Sugiura, T. Hirosumi, *et al.*, "Generation and detection of terahertz radiation by electro-optical process in GaAs using 1.56 μm fiber laser pulses," *Applied Physics Letters*, Vol. 85, p. 3974, 2004.
- [42] A. Syouji, S. Saito, K. Sakai, M. Nagai, K. Tanaka, H. Ohtake, *et al.*, "Evaluation of a terahertz wave spectrum and construction of a terahertz wave-sensing system using a Yb-doped fiber laser," *Journal of the Optical Society of America B-Optical Physics*, Vol. 24, p. 2006, 2007.
- [43] Mojca Jazbinsek, Uros Puc, Andreja Abina, and Aleksander Zidansek, "Organic Crystals for THz Photonics," *Appl. Sci.* 2019, 9, 882.
- [44] Jia Xu, Björn Globisch, Christina Hofer, Nikolai Lilienfein, Thomas Butler, Nicholas Karpowicz, and Joachim Pupeza, "Three-octave terahertz pulses from optical rectification of 20 fs, 1μm, 78MHz pulses in GaP," *J. Phys. B: At. Mol. Opt. Phys.* 51 (2018) 154002.
- [45] Katsuyoshi Aoki, Janne Savolainen, and Martina Havenith, "Broadband terahertz pulse generation by optical rectification in GaP crystals," *Appl. Phys. Lett.* 110, 201103 (2017).
- [46] C. Vicario, A. V. Ovchinnikov, S. I. Ashitkov, M. B. Agranat, V. E. Fortov, and C. P. Hauri, "Generation of 0.9-mJ THz pulses in DSTMS pumped by a Cr:Mg₂SiO₄ laser," *Optics Letters* Vol. 39, Issue 23, pp. 6632–6635 (2014).
- [47] P. Y. Han, M. Tani, F. Pan, and X.-C. Zhang, "Use of the organic crystal DAST for terahertz beam applications," *Optics Letters* Vol. 25, Issue 9, pp. 675–677 (2000).

- [48] John J. Carey, Ray T. Bailey, D. Pugh, J. N. Sherwood, and F. R. Cruickshank, and Klaas Wynne, "Terahertz pulse generation in an organic crystal by optical rectification and resonant excitation of molecular charge transfer," *Appl. Phys. Lett.* 81, 4335 (2002).
- [49] Darrow J T, Zhang X-C, Auston D H and Morse J D, "Saturation properties of large-aperture photoconducting antennas," *IEEE J. Quantum Electron.* 28 1607–16 (1992)
- [50] H A Hafez, X Chai, A Ibrahim, S Mondal, D Féralchou, X Ropagnol and T Ozaki, "Intense terahertz radiation and their applications," *J. Opt.* 18 093004 (2016)
- [51] Li-Mo Wang, "Relationship between Intrinsic Breakdown Field and Bandgap of Materials," 2006 25th International Conference on Microelectronics, 2006.
- [52] D. H. Auston, A. M. Johnson, P. R. Smith, and J. C. Bean, "Picosecond optoelectronic detection, sampling, and correlation measurements in amorphous semiconductors," *Appl. Phys. Lett.* 37, 371 (1980).
- [53] P. Uhd Jepsen, R. H. Jacobsen, and S. R. Keiding, "Generation and detection of terahertz pulses from biased semiconductor antennas," *Journal of the Optical Society of America B* Vol. 13, Issue 11, pp. 2424-2436 (1996).
- [54] M. van Exter, C. Fattinger, and D. Grischkowsky, "Terahertz time-domain spectroscopy of water vapor," *Opt. Lett.* 14, 1128–1130 (1989).
- [55] W. Withayachumnankul, and M. Naftaly, "Fundamentals of Measurement in Terahertz Time-Domain Spectroscopy," *J. Infrared Millim. Terahertz Waves* 35, 610–637 (2014).
- [56] L. Duvillaret, F. Garet, and J. L. Coutaz, "A reliable method for extraction of material parameters in terahertz time-domain spectroscopy," *IEEE J. Sel. Top. Quantum Electron.* 2, 739–746 (1996).
- [57] L. Duvillaret, F. Garet, and J. L. Coutaz, "Highly precise determination of optical constants and sample thickness in terahertz time-domain spectroscopy," *Appl. Opt.* 38, 409–415 (1999).
- [58] I. Pupeza, R. Wilk, and M. Koch, "Highly accurate optical material parameter determination with THz timedomain spectroscopy," *Opt. Express* 15, 4335–4350 (2007).
- [59] M. Scheller, C. Jansen, and M. Koch, "Analyzing sub-100- μm samples with transmission terahertz time domain spectroscopy," *Opt. Comm.* 282, 1304–1306 (2009).
- [60] M. Kruger, S. Funkner, E. Brundermann, and M. Havenith, "Uncertainty and Ambiguity in Terahertz Parameter Extraction and Data Analysis," *J. Infrared Millim. Terahertz Waves* 32, 699–715 (2011).
- [61] M. Naftaly, and R. Dudley, "Methodologies for determining the dynamic ranges and signal-to-noise ratios of terahertz time-domain spectrometers," *Opt. Lett.* 34, 1213–1215 (2009).
- [62] P. U. Jepsen, and B. M. Fischer, "Dynamic range in terahertz time-domain transmission and reflection spectroscopy," *Opt. Lett.* 30, 29–31 (2005).

- [63] F. Blanchard, D. Golde, F. H. Su, L. Razzari, G. Sharma, R. Morandotti, T. Ozaki, M. Reid, M. Kira, S. W. Koch, and F. A. Hegmann, "Effective Mass Anisotropy of Hot Electrons in Nonparabolic Conduction Bands of n-Doped InGaAs Films Using Ultrafast Terahertz Pump-Probe Techniques," *Phys. Rev. Lett.* **107**, 107401 (2011).
- [64] Laboratory of Terahertz Spectroscopy, Prague. <https://lts.fzu.cz/en/intro.php>. (2012). [Online; Accessed: 08/01/2021].
- [65] M. Schall, H. Helm, and S. R. Keiding, "Far Infrared Properties of Electro-Optic Crystals Measured by THz Time-Domain Spectroscopy," *International Journal of Infrared and Millimeter Waves* volume **20**, 595–604 (1999).